Institut für Physik und Astronomie
Physik weicher Materie

# The Interplay of Nanostructure and Efficiency of Polymer Solar Cells

**Dissertation**
**zur Erlangung des akademischen Grades**
**"doctor rerum naturalium"**
**(Dr. rer. nat.)**
**in der Wissenschaftsdisziplin "Experimentalphysik"**

**Eingereicht von:** ***Chunhong Yin***

**Betreuung:** ***Prof. Dr. Dieter Neher***

Potsdam, den 04.12.2008

# Abstract

The aim of this thesis is to achieve a deep understanding of the working mechanism of polymer based solar cells and to improve the device performance. Two types of the polymer based solar cells are studied here: the polymer-polymer solar cells, and the polymer-small molecule solar cell which has polymer as electron donor incorporating with organic small molecule as electron acceptor.

For the polymer-polymer devices, I compared the photocurrent characteristics of bilayer and blend devices as well as the blend devices with different nano-morphology, which is fine tuned by applying solvents with different boiling points. The main conclusion based on the complementary measurements is that the performance-limiting step is the field-dependent generation of free charge carriers, while bimolecular recombination and charge extraction do not compromise device performance.

Regarding polymer-small molecular hybrid solar cells I combined the hole-transporting polymer M3EH-PPV with a novel small molecule electron acceptor vinazene. This molecule can be either deposited from solution or by thermal evaporation, allowing for a large variety of layer architectures to be realized. I then demonstrated that the layer architecture has a large influence on the photovoltaic properties. Solar cells with very high fill factors of up to 57 % and an open circuit voltage of 1V without thermal treatment of the devices were achieved. In the past, fill factors of solar cells exceeding 50 % have only been observed when using fullerene-derivatives as the electron-acceptor. The finding that proper processing of polymer-vinazene devices leads to similar high values is a major step towards the design of efficient polymer-based solar cells.

# Zusammenfassung

Ziel dieser Dissertation ist es, die grundlegende Arbeitsweise von polymerbasierten Solarzellen zu verstehen und ihre Leistungsfähigkeit zu erhöhen. Zwei Arten von organischen Solarzellen werden untersucht: Polymer-Polymer Solarzellen und Polymer-kleine Molekül Solarzellen, bei denen das Polymer als Elektronendonator und das organische kleine Molekül als Elektronenakzeptor fungiert.

Bei den Polymer-Polymer Solarzellen untersuchte ich sowohl die Photostromcharakteristik von Zweischicht- und Mischsolarzellen als auch Mischsolarzellen mit unterschiedlicher Nano-Morphologie, welche durch die Verwendung von Lösungsmitteln mit unterschiedlichen Siedetemperaturen modifiziert wird. Die Hauptschlussfolgerung aus den vergleichenden Messungen ist, dass der effizienzlimitierende Faktor die feldabhängige Generation freier Ladungsträger ist, wohingegen bimolekulare Rekombination oder die Extraktion der Ladungsträger die Leistungsfähigkeit von Polymer-Polymer- Solarzellen nicht beeinträchtigen.

Bezüglich der Polymer-kleine Molekül Hybridsolarzellen kombinierte ich das Loch-leitende konjugierte Polymer M3EH-PPV mit einem neuartigen kleinen Vinazene-Molekül als Elektronenakzeptor. Dieses Molekül bietet die Möglichkeit, entweder aus einer Lösung heraus verarbeitet, oder im Hochvakuum verdampft zu werden, wodurch eine Vielzahl an unterschiedlichen Probenstrukturen realisiert werden kann. Dadurch konnte ich zeigen, dass die Struktur der aktiven Schicht einen großen Einfluss auf die photovoltaischen Eigenschaften hat. Die Solarzellen erreichten einen Füllfaktor von bis zu 57 % und eine Kurzschlussspannung von 1 V. In der Vergangenheit konnten Füllfaktoren über 50 % bei organischen Solarzellen nur in Verbindung mit einem Fulleren-Akzeptor beobachtet werden. Das Resultat, dass bei geeigneter Präparation der Polymer-Vinazene Schicht vergleichbare Ergebnisse erzielt werden können, ist ein bedeutender Schritt hin zu effizienteren Polymersolarzellen.

# Contents

# Chapter 1 Motivation & Outline

## 1.1 Motivation

The world energy consumption is rising whereas natural resources as oil and gas are limited resulting already in increased energy costs in the past years. Only with the help of alternative energies like wind or solar the energy crisis can be prevented. Since the solar energy introduction on the earth is 1000 times larger than the current worldwide energy consumption, it is forecasted that solar energy will become the main energy source of the future.

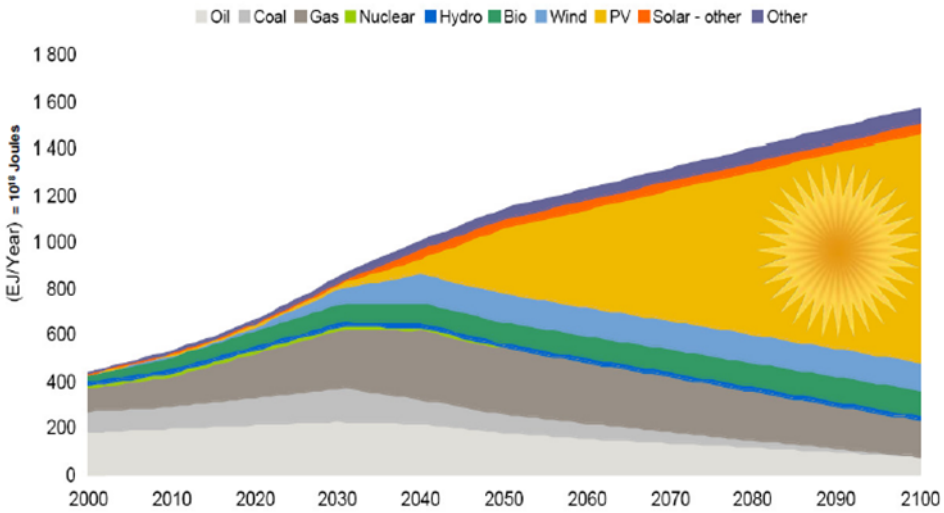


**Figure 1 Trend of global energy consumption on different sources until the year of 2100 (Source: Prognose des Wissenschaftlichen Beirates der Bundesregierung Globale Umweltveränderungen, 2006).**

Although the world solar cell production is nearly doubling year by year, reaching most likely more than 10 GW in 2010 after 3.5 GW in 2007, the use of solar cells relies still heavily on government funded programs since solar energy is currently not cost competitive with the more conventional energy sources. To reach grid parity with other energy sources, the cost of solar energy has to come down by a factor of 2-5 depending on region and technology used. The need for lower cost solar cells have triggered the search into new solar cells architectures as a cheaper alternative to the more than 50 year old crystalline silicon based solar cells. The key to lower cost solar cells lies in reduced material consumption and easier processing. Organic solar cells come with the promise to achieve these goals in

the near future. However their efficiencies and stability can currently not compete with their inorganic counterparts. Optimisation of the organic solar cells needs thorough understanding of the physical processes governing the conversion of light into electricity.

Organic solar cells represent the subclass of solar cells where the active material contains organic materials like polymers or small molecules. First organic photovoltaic cells were fabricated with a single layer of organic material sandwiched between two electrodes with different work functions. Since the photogenerated excitons are strongly bound in organic materials and dissociated electrons and holes need to travel through the same material, which opens the path for recombination, the efficiencies of these cells were generally very low, less than 0.1%.[1] In 1986, significant higher efficiencies could be reached by Tang.[2] Thesis devices consisted of a thermally evaporated small molecule phthalocyanine donor layer followed by a perylene di-imide electron acceptor layer. The solar cell power conversion efficiency reached 1%. Currently, the best reported efficiencies for organic solar cell with vacuum sublimed small molecules are around 5%.[3, 4] Small molecules are drawing great attention owing to the advantage of their high purity, ease of synthesis and generally high charge carrier mobilities. Vacuum sublimation allows for easy deposition of well defined multi-layered device structures.

On the other hand, the potential of roll-to-roll processing on low-cost flexible plastic substrates raised great interest in solution processed polymer solar cells. In 1995 Halls et al.[5] and Yu et al.[6] reported independently efficient solution processed polymer based solar cells. Bi-layer heterojunction structures are difficult to achieve from solution since depositing of a second layer may dissolve the first layer. Essentially, most polymers dissolve in common organic solvents, the numbers of polymer combinations which can be used to fabricate solution processed bilayer by using orthogonal solvents devices are very limited. Therefore so-called bulk heterojunction have been introduced, relying on the phase separation of the individual polymer components into nano to micron sized domains. Solar cells made from polymer-polymer blends exhibited moderate energy conversion efficiencies (ECE) of the order of 1.5 to 1.8%.[7-9] Even higher efficiencies of up to 6% could be reached by using fullerene based acceptors. [4, 10]

**Table 1 Four main types of organic solar cells and the processing methods.**

| Donor | Acceptor | processing method |
|---|---|---|
| dye-sensitized solar cells | | Solution processed |
| small molecule | small molecule | Vacuum processed |
| polymer | small molecule | |
| polymer | polymer | Solution processed |

Shown in Table 1 are the main types of organic solar cells. For the sake of completeness, it should be mentioned that sometimes also the so-called dye sensitised solar cell (a hybrid organic inorganic approach) are counted into the class of organic solar cells. Dye-sensitized solar cells (DSC), also referred to as Grätzel cells, were invented by Michael Grätzel and Brian O'Regan in 1991.[11] In these cells, the function of light absorption is separated from charge carrier transport, a concept fundamental different from the conventional semiconductor based solar cells. Electrolyte is required for the regeneration of the dye molecule by electron transfer from a redox species in solution. The record energy conversion efficiency is above 10%, which is already at the practical application line. However, for commercial applications, a serious chemical stability problem needs to be solved first, concerning solvent leakage and corrosion. Further effort needs to be given to replacing this electrolyte with solid state hole transporter alternatives.[12] There has been much work devoted on this point, but only a considerably lower energy conversion efficiency of about 5.1% has been yet achieved. [13] Recently reported solar cell performance from these four different types of solar cells are summarized in Table 2.

So far, the majority of research work on solution-processed organic solar cells has been concentrated on the system using poly(3-hexylthiophene), P3HT as electron donor and ([6,6]-phenyl $C_{61}$-butyric acid methyl ester), PCBM as electron acceptor. However, a major drawback of PCBM is its low absorption coefficient. Additionally, the very high electron affinity of PCBM severely limited the open circuit voltage. These drawbacks of this system limit the theoretical reachable efficiency to less than 7%, which is too low to compete with inorganic solar cells.

**Table 2 Comparison of the some performance of the recently reported organic solar cells. All cells were stated to have been measured under 1 sun 1.5AM solar radiation. $V_{oc}$ is the open circuit voltage, $J_{sc}$ is the short circuit current density, FF is the fill factor, and η is the efficiency, which is the percentage of power out ($P_{out}$) to power in ($P_{in}$) where $P_{out}$= Voc ·Jsc ·FF and thus η= Voc·Jsc· FF/$P_{in}$.**

| Type of organic solar cells | Active layer materials | $J_{sc}$ (mA/cm$^2$) | $V_{oc}$ (V) | FF (%) | η (%) | Ref. |
|---|---|---|---|---|---|---|
| Dye sensitized solar cell (With electrolyte) | TiO2/dye/$I^- - I_2$ | 19.4 | 0.795 | 71.0 | 10 | [14] |
| Dye-sensitized solar cells (Solid state) | TiO2/dye/CuI or CuSCN<br>TiO2/dye/spiro-MeOTAD | 9.3<br>11.0 | 0.516<br>0.86 | <br>68 | 3.0<br>5.1 | [13] * |
| Small molecule PV cells Vacuum processed | CuPc:C60 | 15.0 | 0.54 | 61 | 5.0 | [15] |
| Polymer-small molecule Solution processed | P3HT:PCBM blend | 11.65 | 0.66 | 70.11 | 5.4 | [4] |
| All-polymer Solution processed | M3EH-PPV:CN-Ether-PPV<br>MDMO-PPV:PF1CVTP<br>P3HT:F8TBT | 3.6<br>3.0<br>4.0 | 1.4<br>1.4<br>1.2 | 35<br>37 | 1.7<br>1.5<br>1.8 | [7]<br>[8]<br>[9] |

* Sample is measured at light intensity of 126 mW/cm$^2$

* The corresponding chemical structures of the active layer materials can be found in the references.

In this thesis we investigate new materials for organic solar cells using polymers as electron donor and either polymers or small molecules as electron acceptors. The electron acceptors are chosen to allow for high open circuit voltages and also absorb a significant portion of the sunlight. Although the theoretical limit following this approach is well above 10%, the current measured efficiencies are much lower. Basic understanding of physical process which influences the device efficiency is required for further optimisation of device structures and materials to reach for higher efficiencies.

The aims of this work are:

To obtain a deeper understanding of the working mechanism and hereby to improve the device performance for all-polymer solar cells by finer controlling the film morphology.

To replace fullerene derivatives with a novel small molecule and further improve its efficiency by applying different device structures and characterizing techniques.

## 1.2 Outline

In **Chapter 2**, a brief introduction to organic semiconductors and their essential properties as well as the basic working mechanism of polymer solar cells is given. In the second part of this chapter, a more comprehensive insight into the important key factors which might limit the final energy conversion efficiency is discussed. The basic sample preparation techniques, the experimental setups and the characterization methods are described in **Chapter 3**.

Chapters 4 to 7 describe the main work and achievements of this thesis. This is organized in four parts:

In **Chapter 4** emphasis is given to the understanding of charge carrier generation and electron blocking at a hole transporting polymer interlayer. Three different device architectures of polyfluorene-based solar cells are applied. In this study, a novel interlayer technique is successfully introduced for the first time in the solar cell preparation process, and well defined bilayer devices can be achieved even from two polymers which have no large solubility difference.

The preliminary studies related to intrachain excitons and interchain exciplexes are presented in **Chapter 5.** By performing steady state photoluminescence (PL) and time-resolved photoluminescence spectroscopy, relationship between the excited state and the photovoltaic performance is studied. An anticorrelation between exciplex emission and photovoltaic properties can be established. It is concluded that the efficiency in polymer solar cell is limited by the low dissociation efficiency of the geminate electron-hole pairs.

The influence of polymer film nanomorphology on the final charge carrier generation efficiency is studied in detail in **Chapter 6**. Variation of the polymer blend layer nanomorphology by using solvents with different boiling points clearly tune the interchain interaction between the donor and acceptor polymers. We demonstrated in this chapter that the blend nanomorphology has a profound effect on the initial separation of the Coulombically bound electron-hole pairs, on the probability that they recombine via the formation of interfacial exciplexes or, possibly, via intrachain triplet excitons, and, therefore, on the final solar cell properties. For an annealed layer coated from a 1:4 tri-chlorobenzene:chloroform mixture, a fill factor of 44% was achieved, which is among the highest values reported for polymer-polymer blends.

In **Chapter 7** solar cells comprising of PPV-donor polymer and a novel organic small molecule as the electron acceptor are presented. It is found that the photovoltaic properties of these cells, in particular the fill factor, correlate strongly with the heterojunction topology. A fill factor of 57% is obtained from a device with a spin-coated polymer layer and an evaporated film of the novel electron acceptor molecule. This very high FF is comparable to values reported for organic solar cells using fullerenes as the electron acceptor. In fact, the device we present here is the first polymer-based solar cell with both high fill factor and high open circuit voltage.

**Chapter 8** contains the summary and outlook. The description of various experimental methods is included in the **Appendix.** The thesis ended with the **Acknowledgment**.

# Chapter 2 Introduction

Progress in organic photovoltaic cells requires a clear understanding of the peculiar physics of organic semiconductors and devices.[16] After introducing the unique advantage of organic semiconductors, we will give an overview of organic materials for photovoltaic (PV) application. We then discuss the basic physical processes that lead to photocurrent generation in organic solar cells as well as the typical characteristics of polymer solar cells. Generally recognized efficiency-limiting factors, such as charge carrier generation, recombination and transport are reviewed.

## 2.1 Organic semiconductors

There are several advantages by using organic semiconductors for PV applications compared to inorganic materials: First, the chemical structure can be easily tuned in order to adjust the energy gap, energy levels, charge transport properties as well as solubilities of the materials. Second the high absorption coefficient of organic materials (typically for polymers usually >= $10^5$ $cm^{-1}$)[17] allow to have high absorption in even less than 100 nm thick layers, which is much thinner than the 1 μm for amorphous silicon or even 200 μm for crystalline Si PV cells. Therefore, organic solar cells have the advantage of much lower weight and material consumption. Additionally, organic materials can be processed not only by thermal evaporation (dry processing) but also by spin coating, doctor blading or inkjet printing techniques (wet processing). Especially, all wet processing can be performed at low temperature and ambient pressure, and allows devices to be fabricated on plastic substrates for flexible devices. These techniques are required for the roll-to-roll processing that will reduce the cost of polymer-based PV down to a point where it can compete with current grid electricity.

Organic semiconductors can be divided into different categories, for example pigments, liquid crystals, small molecules and polymers. Here we distinguish small molecules and polymers by the length of repeat units. Polymers generally contain more than 10 repeat units. For a long time, polymers were considered as insulators, with typical applications as protection for electric cables and the covers of machines. In 1977, a new world of electronic materials was opened by three

scientists, A. Heeger, A. MacDiarmid and H. Shirakawa, when they discovered that chemically doped polyacetylene had a conductivity of $10^5$ $Sm^{-1}$. (Nobel Prize in Chemistry, 2000). Teflon shows a conductivity of $10^{-16}$ $Sm^{-1}$ as a perfect insulator. The high conductivity found in the doped polyacetylene clearly opened up the field of plastic electronics.

A conductive polymer is, in most cases, a doped conjugated polymer. In conjugated polymers, the *s* orbital together with two of the *p* orbitals formed 3 $sp^2$ hybrid orbitals, leaving one *p* orbital unhybridized. The overlap of the $sp^2$ or *sp* orbitals forms the single bonds (σ-bond), where the electrons are strongly bound and localized. On the other hand, the unhybridized *p* orbital overlaps spatially with the other unhybridized *p* orbital of the neighbouring carbon atoms, resulting in molecular π-bonds. The π-bond and the σ-bond together formed a double bond. The electrons in the π-bonds are more loosely bound and delocalized. The essential property of conjugation is that the π-electrons are much more mobile than the σ-electrons, so they can move along the π-conjugation system. The formation of a π-bond in ethylene is shown in Figure 2 as an example.

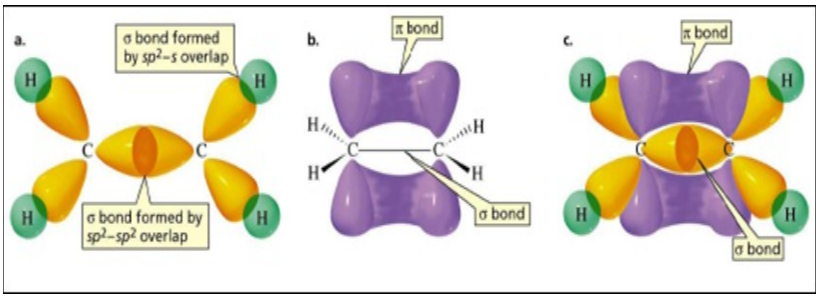


**Figure 2 Double bond formation in ethylene. The $sp^2$ orbitals are shown in yellow and the unhybridized $p_z$ orbitals in purple. The carbon–carbon sigma bond in ethylene is formed by $sp^2$-$sp^2$ overlap, and the carbon–carbon π-bond is formed by side-to-side overlap of a *p* orbital of one carbon with a *p* orbital of the other carbon. (reproduced from reference [18])**

Regarding the optical and electronic properties of π-conjugated electron systems, the highest occupied molecular orbital (HOMO) and the lowest unoccupied molecular orbital (LUMO) are most relevant. In molecular physics, metals, semiconductors and insulators are differentiated by the energy difference between their LUMO and HOMO, determining the band gap ΔE=E(LUMO)-E(HOMO). The commonly used conjugated polymers have an optical band gap between 1 and 4 eV.[19] Due to the delocalized character of π-conjugated systems, the band gap will decrease with increasing polymer conjugation length.

In Figure 3, the chemical structures of several important and commonly used solution-processable conjugated polymers are illustrated along with a fullerene molecule. In the upper line are three hole-conducting, donor-type polymers: poly[2-methoxy-5-(2-ethylhexyloxy)]-1,4-phenylenevinylene, MEH-PPV, poly[9,9-dioctylfluorene-co-bis-N,N-(4-butylphenyl)-bis-N,N-phenyl-1,4-phenylenediamine], PFB, and P3HT. Typical electron-conducting acceptors are listed below: poly[oxa-1,4-phenylene-1,2-(1-cyano)-ethylene-2,5-dioctyloxy-1,4-phenylene-1,2-(2-cyano)-ethylene-1,4-phenylene], CN-Ether-PPV, poly(9,9-dioctylfluorene-co-benzothiadiazole), F8BT, and a soluble derivative of $C_{60}$, [6,6]-phenyl $C_{61}$ butyric acid methyl ester, PCBM.

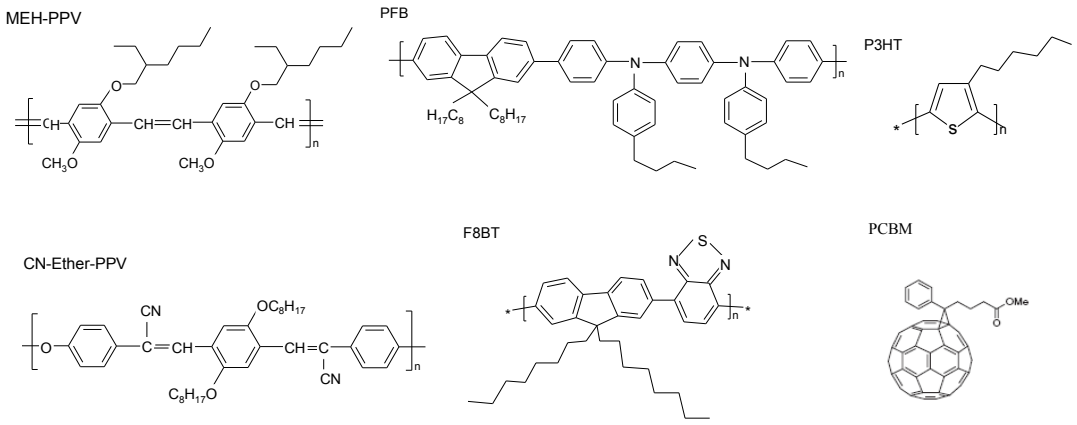


**Figure 3 The chemical structures of conjugated polymers and molecules commonly used in bulk heterojunction solar cells. Upper line: donor polymers MEH-PPV, PFB, P3HT. Lower line: electron acceptor polymers CN-Ether-PPV, F8BT and a soluble derivative of C60, PCBM.**

Unfortunately, unlike inorganic materials, photoexcitation of organic semiconductors does not automatically generate free charge carriers, but strongly Coulomb bound electron-hole pairs (termed as excitons) with a binding energy in excess of the thermal energy at room temperature. This is due to the relative low dielectric constant of the organic semiconductors. In order to generate free charge carriers, the excitons have to be split up with the help of an internal electric filed. Therefore, the power efficiency of solar cells made from only one organic compound is rather low, in general less than 0.1%. The photogenreated excitons can, however, be efficiently dissociated at an interface to a second organic layer or an electrode, where, owing to a suitable potential difference, charge transfer takes place. If the exciton decays via recombination or is trapped before reaching this

interface, it will not contribute the photocurrent generation. This decay is characterized by an exciton diffusion length and exciton lifetime. For polymers, these two parameters are typically 5 - 14 nanometers and a few nanoseconds, respectively. The binding energy of excitons can be expressed as $E_b=E_g-E_a$, where $E_b$ is binding energy, $E_g$ is band gap and $E_a$ is absorption edge (or exciton energy). The binding energy for PPV polymers or derivatives is around 0.4~0.5 eV.[20]

## 2.2 Polymer photovoltaic fundamentals

Polymer photovoltaic cells are polymer-based devices that convert sunlight to electrical energy. Figure 4 shows a simple solar cell structure where a polymer layer is sandwiched between two conductive electrodes. At least one of the electrodes is required to be transparent or semi-transparent to allow sunlight to reach the active layer. ITO (Indium-Tin-Oxide) is the most commonly used transparent electrode. The counter electrode is often formed from low work function metals such as Al, Ag, or a Ca/Al combination. An electric field is created inside the cell due to the work function difference between these two electrodes.

For some cases, an electron-blocking layer (ELB) and a hole-blocking layer (HLB) are inserted on both sides of the active layer. The substrate materials are either glass or, in some cases, a transparent flexible polymer foil, for example, polystyrene. [21-23]

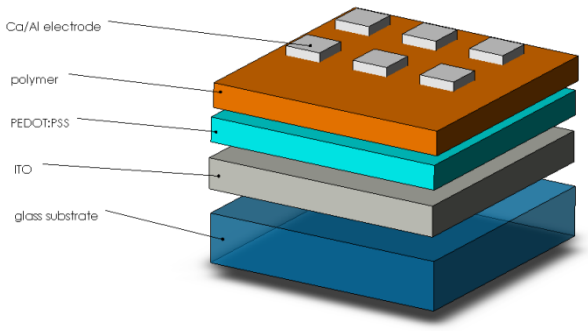


**Figure 4 Device structure of a typical polymer solar cell. The conjugated polymer film may be either a single component layer, a blend layer or a double layer.**

### 2.2.1 Process of solar energy convertion to current

The process of converting sunlight to electric current in polymer based photovoltaic cells is accomplished by four consecutive steps as described in Figure 5. As the first step, photons are absorbed with efficiency $\eta_A$. The generated excitons in the donor (or acceptor) material have an energy $E_{ex}$, which is smaller than the LUMO-HOMO gap by the exciton binding energy. These excitons diffuse to the donor-acceptor interface before they recombine with an efficiency $\eta_d$. A very important issue to be addressed later is the possibility of geminate recombination after the charge transfer has occurred. The efficiency for separating excitons reaching the interface into free carriers is represented by $\eta_{cg}$, which is the product of the charge transfer efficiency and the probability for charge separation. Finally, the free charge carriers are collected at the electrodes with efficiency $\eta_{cc}$, which is sensitively dependent on the nano-morphology of the active film structure.

An important property of solar cells is the external quantum efficiency (EQE) also called incident-photon-to-convert-electron efficiency (IPCE), which is the product of the efficiencies defined above:

$$\eta_{IPCE(\lambda,V)} = \eta_{A(\lambda)} \cdot \eta_{d(V)} \cdot \eta_{cg(V)} \cdot \eta_{cc(V)}$$

The IPCE spectrum gives information on the current that a solar cell will produce under the short circuit condition when illuminated by different wavelengths. If all the photons of a certain wavelength are absorbed and all the resulting charge carriers are collected, then the IPCE at that particular wavelength should be unity. As a consequence, the IPCE strongly depends on the absorption of light and the collection of charges. Contrary to EQE, the internal quantum efficiency (IQE) only considers processes involving absorbed photons, excluding losses due to the reflection and transmission of incident photons.

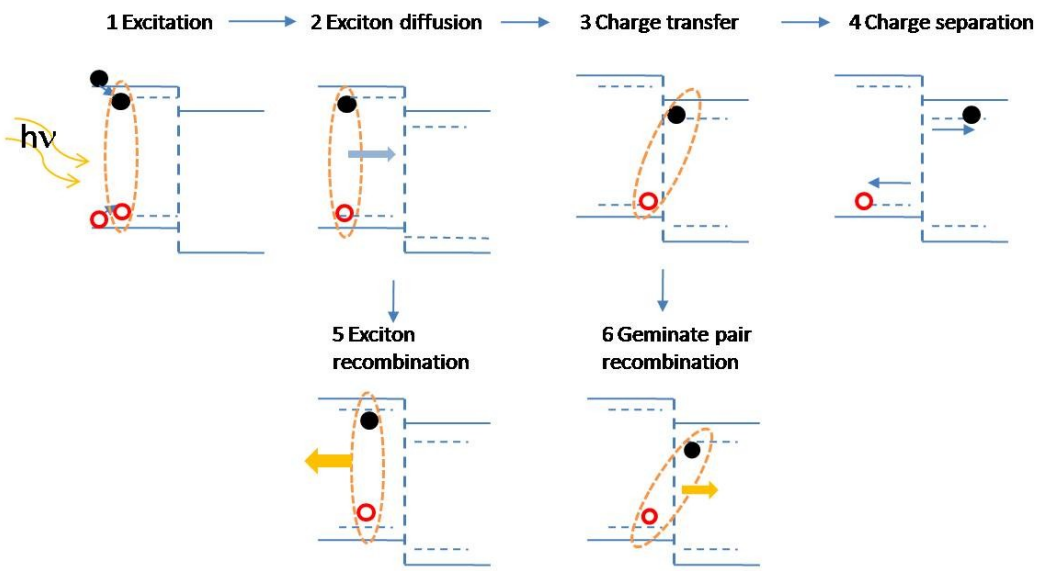


**Figure 5 A schematic illustration of the general process of charge carrier generation and recombination at a donor-acceptor heterojunction.**

a) Photon absorption and exciton generation

Upon absorption of photons, bound electron and hole pairs (exciton) rather than free charges are formed. Hereby, the electron and hole remain on the same polymer chain, so it is also termed as an intrachain exciton. If the spin of the electron stays unchanged, the excited state is a singlet state. On the contrary, if the spin is reversed, the state is a triplet state. The energy required to excite an electron from the ground state to the excited state can be roughly calculated from the optical band gap, $\Delta E_{opt}$=E(LUMO)-E(HOMO)-$E_b$, with $E_b$ the exciton binding energy. Polymers absorb only light which has a higher energy than the optical band gap. Unfortunately, the majority of conjugated polymers have a band gap higher than 2.0 eV (600nm), limiting the possible absorption of solar radiation to about 30%. Low band gap polymers are under investigation.[24, 25] However no significant success has been achieved so far.

b) Exciton diffusion to the heterojunction

The exciton diffusion efficiency $\eta_d$ describes the fraction of generated excitons reaching the donor-acceptor interface. The exciton diffusion efficiency is crucially sensitive to the active layer architecture in single or bi-layer devices. As the exciton diffusion length is typically 10 nm compared to an absorption length of ca. 100 nm for most soluble conjugated systems, bilayer devices with a single planner heterojunction between a donor and an acceptor layer are interestingly inefficient. The introduction of polymer blend (bulk heterojunction) has solved this problem.

Hereby the donor and acceptor polymers or molecules are coated from a common solvent. During drying of the layer, a separation into donor- and acceptor-rich domains occurs, resulting in distributed bulk heterojunction. Exciton diffusion efficiencies close to 100%, as evident from the complete quenching of fluorescence has been seen in blend, where the length scale of phase separation is comparable to the exciton diffusion length.

c) Charge transfer and free charge carrier generation

Once the exciton reaches the interface, they ideally separate into spatially-separated charge carriers via charge transfer. A result of charge transfer at the heterojunction is that the positively charged hole remains on the donor material whereas the electron stays on the acceptor material (Figure 6a). Photoluminescence quenching of highly luminescent polymers was used as a clear demonstration of efficient charge transfer. Apparently, there are two possible loss processes taking place directly after charge transfer. The first loss process is energy transfer, as illustrated in Figure 6b. If the HOMO and LUMO levels of the acceptor are located between the HOMO/LUMO of the donor, the excitons will directly migrate to the acceptor without splitting up, accompanied by energy loss.

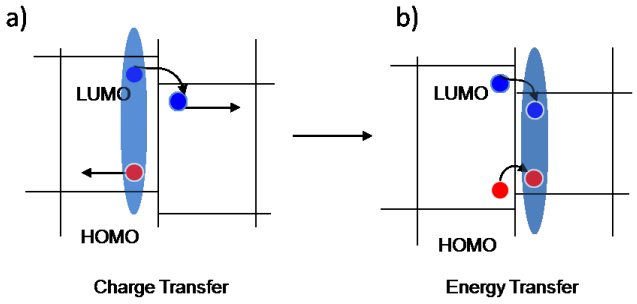


**Figure 6 a) Exciton dissociation via charge transfer, if the LUMO level offset between the donor and acceptor is larger than exciton binding energy. b) If both the HOMO and LUMO of the electron acceptor are located between the HOMO/LUMO of the donor, energy transfer takes place.**

Secondly, charge transfer will, in most cases, lead to a electron-hole pair with the electron on the acceptor and the hole remaining on donor, referred to as a geminate pair. In this case, the electron and hole remains Coulombically bound across the D-A interface as shown in Figure 7.

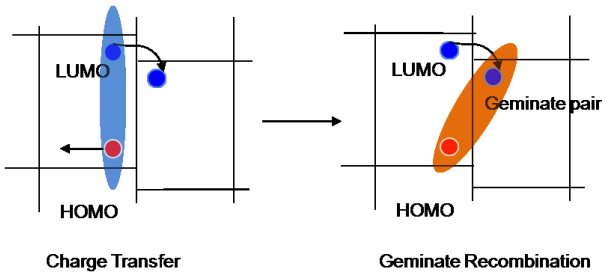


**Figure 7 After charge transfer, geminate recombination often occurs in the polymer-based solar cell.**

This geminate pair can either be dissociated by an electric field or by thermal energy, or recombine via a lower energy exciplex emission or via triplet recombination. As we will show later, this geminate recombination is one of the main loss channels for the efficiency in polymer-polymer solar cells.

d) Charge collection

After the excitons have been dissociated, the free charges need to be transported to the electrodes. In the D-A bilayer devices, when both layers are equally thick, the distance both carriers need to travel are equal, and since both carriers travel through the bulk, the donor material serves to transport holes whereas the electrons travel through the acceptor material. Then, the collection efficiencies are mainly affected by the charge carrier mobility, material defects and impurities. However, the issue is more complicated in the case of polymer blends, where separated percolation paths for both charge carriers are required and where the photogenerated electrons and holes can meet again and recombine. The morphology characterized by the phase separation and inter-penetration of donor and acceptor materials strongly influences the efficiency. We will discuss the this issue in detail in the next section.

### 2.2.2 Characteristics of polymer photovoltaic cells

The most important parameter describing the performance of solar cells is the energy conversion efficiency (ECE), which can be calculated from the current voltage (I-U) curves measured under simulated solar illumination.

Assuming exciton dissociation occurs throughout the entire device, the I-U curve of the device can be understood with the help of a Metal-Insulator-Metal (MIM) model. In the following, the four relevant working regimes of PV devices is shown schematically in Figure 8.

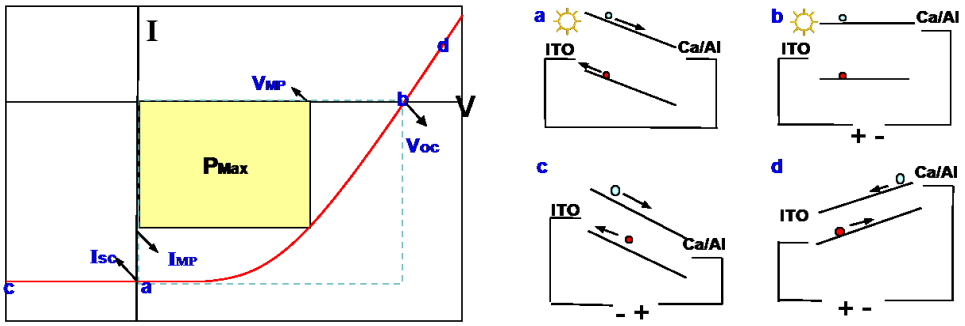


**Figure 8 Typical I-U curve of a polymer solar cell device. Four points are illustrated by the MIM model pictures: a) short circuit current $I_{sc}$ at closed circuit condition, b) open circuit voltage $V_{oc}$ at flat band or open circuit condition, c) under reversed bias V<0, d) under forward bias V>$V_{oc}$**

a) When no external voltage is applied, the photo-generated free charge carriers can drift to the respective electrodes due to the built-in field created by the difference of the work functions of the two electrodes. The resulting current is called the short circuit current, $I_{SC}$. It is a function of the illumination intensity.

b) The open circuit voltage $V_{oc}$ is simply the voltage for which the total current through the device under illumination is zero. Neglecting diffusion, $V_{oc}$ is equal to the flat band voltage $U_{FB}$, at which the internal electric field is zero.

c) Under reverse bias (V<0) the generated charges drift under an increased internal electric field. When all charges arrive at the electrodes, this current is tending to saturation. However, the internal field might also affect the efficiency of carrier generation and thus the shape of the I-U characteristics under reverse bias.

d) Efficient charge injection takes place when the forward bias voltage is larger than $V_{oc}$ and the direction of the current through the device is reversed. Under this condition, a light-emitting-diode is operating. When an electron or hole blocking layer with sufficiently high injection barrier is inserted in the device, the current beyond $V_{oc}$ should stay very low.

The spectral photocurrent efficiency commonly referred to as IPCE is calculated as the number of collected electrons per incident photon under short circuit dondition.

$$IPCE = \frac{\#electrons}{\#photons} = \frac{h \times c \times I_{sc}}{e \times \lambda \times P_{light}}$$

Here, $\lambda$ is the incident wavelength, $e$ the elementary charge, $h$ the Planck constant, $c$ the speed of light and $P_{light}$ is the incident light power.

On the I-U curve, $I_{mp}$ and $V_{mp}$ denote the point where the cell delivers the maximum electric power. $P_{max} = I_{mp} * V_{mp}$. The ratio between the $P_m$ and $V_{oc} * I_{sc}$, termed as the fill factor *FF*, represents a measure of the quality of the shape of I-U characteristic. From these quantities, the fill factor can be calculated as:

$$FF = \frac{P_{max}}{I_{sc} \times V_{oc}} = \frac{I_{MP} \times V_{MP}}{I_{sc} \times V_{oc}}$$

The ECE is defined as the ratio of the maximum electric power output of the cell to the incident optical power.

$$ECE = \frac{P_{max}}{P_{light}} = \frac{I_{MP} \times V_{MP}}{P_{light}} = FF \cdot \frac{I_{sc} \times U_{oc}}{P_{light}}$$

We note that the solar cell efficiency is often intensity dependent. Hence, solar radiation standards have been defined in the past in order to compare efficiencies of solar cells.

The most common definition of ECE is based on the air mass (AM) 1.5 spectrum, which is often provided by commercial solar simulators. The AM 1.5 spectrum is the standard spectrum at sea level. It is defined as the spectrum where the length of the actual light path from the sun to the position of the observer is 1.5 times the length of the shortest possible path when the sun is exactly at the zenith.

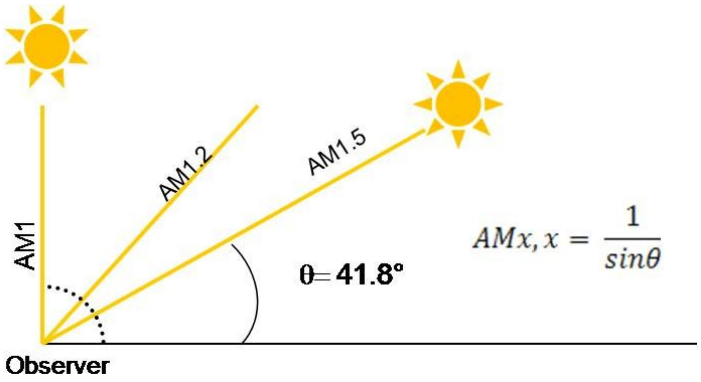


**Figure 9 Solar power on earth surface depends on the angle of incidence due to absorption in the atmosphere. AM1.5 is the solar spectrum when the light incident angle $\theta$ is 41.8 degree.**

## 2.3 Factors limiting the efficiency of polymer solar cells

The operation of polymer bulk-heterojunction solar cell devices is not yet fully understood. The efficiency of solar cells has been reported to be limited by several

factors. One of the issues is inefficient free carrier generation due to geminate recombination as has been demonstrated as the key loss mechanism in polymer-polymer cells.[26-29] Furthermore, due to the low mobility of the polymer molecules, bimolecular recombination and space charge limited current are expected to impede efficient charge collection and hence the final photocurrent generation.

### 2.3.1 Geminate recombination - an analysis based on Onsager's and Braun's theory

Geminate recombination is defined as the recombination of an electron with its parent countercharge, which is thought to govern the quantum efficiency of charge carrier generation in low-mobility solids. [30, 31] The usual approach applied to this issue is Onsager's theory,[32] which initially described the probability that a pair of opposite charged ions in a weak electrolyte would escape recombination. Although this theory is developed for classical particles, it has been successful applied in polymer heterojunctions to calculate the probability that a thermalized charge pair will escape geminate recombination and dissociate under the influence of an external electric field.[33]

In polymer solar cells, if the recombination of free charge carriers and space charge effect can be neglected, the photocurrent density $J_{ph}$ ,which is given by $J_{ph}=J_{light} - J_{dark}$, through the external circuit is calculated as[34]:

$$\boldsymbol{J_{ph} = q \cdot G(E) \cdot L} \qquad \textbf{(Eq 1)}$$

where $q$ is the electric charge, $G$ the generation rate of free electron and holes pairs per unit volume, and $L$ the active layer thickness.

According to Onsager theory, the generation rate is determined by the probability that a photogenerated polaron pair dissociated into free carriers, which is a field dependent process. If $G_{max}$ is the number of excitons (geminate polaron pairs) formed per unit time and volume, the generation rate $G$ of free charge carriers can be written as:

$$\boldsymbol{G(E) = G_{max} \cdot \eta_d(E)} \qquad \textbf{(Eq 2)}$$

and the photo-current is given by:

$$\boldsymbol{J_{ph} = q \cdot G_{max} \cdot \eta_d(E) \cdot L} \qquad \textbf{(Eq 3)}$$

Here, the $\eta_d(E)$ is the probability for a charge pair to escape recombination as described in Onsager theory.

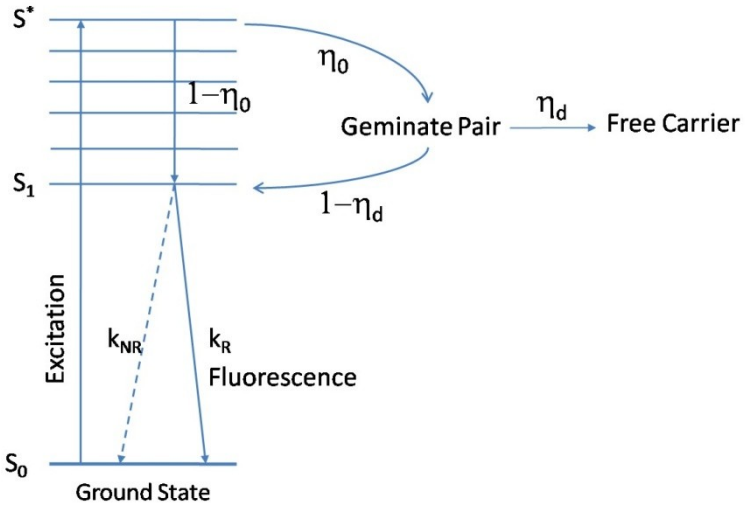


**Figure 10 Schematic drawing of charge carrier generation described by Onsager Model. $\eta_0$ donates the probability of geminate pair formation, and the $\eta_d$ represents the probability of the generated pair escaping recombination and becoming free charge carriers.**

As illustrated in Figure 10, the photogeneration in disordered systems such as molecularly doped polymers and aggregates is a two-step process consisting of bound electron-hole pair generation with a primary quantum yield $\eta_0$ (field independent), and the dissociation of this pair under the influence of the Coulomb attraction and the electric field. The charge dissociation probability is given by $f(r,\theta,E)$.

$$\boldsymbol{f(r,\theta,E) = e^{-A}e^{-B}\sum_{n=0}^{\infty}\sum_{m=0}^{\infty}\frac{A^m}{m!}\cdot\frac{B^{m+n}}{(m+n)!}} \qquad \textbf{(Eq 4)}$$

with $A = \frac{e^2}{4\pi\varepsilon_0\varepsilon_r r k_b T}$, $B = \beta r(1+\cos\theta)$, $\beta = \frac{eE}{2k_bT}$

Here, $r$ is the initial separation distance between the electron and hole in the e-h pair, $\theta$ is the angle of the dipole formed by the electron and hole with respect to the external field $E$, $\varepsilon_0$ is the vacuum permittivity, and $\varepsilon_r$ is the relative permittivity of the semiconductor, $k_b$ is the Boltzmann constant and $T$ is the temperature.

The final exciton dissociation efficiency is given as the product of these two steps, but it needs to be averaged over all possible dipole radii and orientations. If $g(r,\theta)$ is the probability per unit volume of finding the electron at an angle $\theta$ and distance $r$ relative to the counter charge, the total photo-generation efficiency $\eta(E)$ can be expressed as:

$$\boldsymbol{\eta(E) = \eta_0 \int f(r,\theta,E)g(r,\theta)d\tau} \qquad \textbf{(Eq 5)}$$

where $d\tau = r^2 dr sin\theta d\theta d\varphi$ represents the volume element.

The dipole distribution function *g(r,θ)* is often approximated by the isotropic delta function, where each electron travels the same distance $r_0$ from the parent hole after thermalization.

$$g(r) = \delta(r - r_0)/4\pi r_0^2 \quad \textbf{(Eq 6)}$$

After performing the integration over $\theta$ and φ, we can obtain Eq(5) as a function of $r$ only:

$$\eta(E) = 4\pi \cdot \eta_0 \cdot \int_0^\infty f(r,E) g(r) r^2 dr \quad \textbf{(Eq 7)}$$

Substituting Eq(5) and Eq(6) into Eq(7), and integrating the function over *r*, the resultant expression for the charge pair to escape geminate recombination as a function of electric field and initial separation distance is given as[35]:

$$\eta(E) = \eta_0 \cdot \frac{1}{2\beta r_0} \cdot e^{-A} \cdot \sum_{m=0}^{\infty} \frac{A^m}{m!} \cdot \sum_{n=0}^{\infty} \left[1 - e^{-2\beta r_0} \sum_{k=0}^{m+n} \frac{(2\beta r_0)^k}{k!}\right] \quad \textbf{(Eq 8)}$$

The thermalization separation distance $r_0$ can be obtained by fitting the electric field dependent photocurrent density curve to Eq(8).

Often the Onsager model is applied to fit the field dependent efficiency of photo-induced charge generation in organic semiconductor devices. From these fits a separation distance $r_0$ in the range of 1.9 to 2.5 nm has been usually obtained for layers of soluble and fully conjugated PPV derivatives such as poly(phenylimino-1,4-phenylenevinylene-2,5-dioctyloxi-1,4-phenylenevinylene-1,4-phenylene) (PA-PPV), poly(methylimino-1,4-phenylene-1-phenyl-1,2-ethenylene-2,5-dimethoxy-1,4-phenylene-2-phenyl-1,2-ethenylene-1,4-phenylene (PPV-amine) or MEH-PPV.[36, 37] Lloyd-Huges and coworkers have successfully applied Onsager's model to fit the field-dependent efficiency of photoinduced charge generation in an organic field effect transistor made from the conjugated polymer poly[(9,9-dioctylfluorene-2,7-diyl)-co-(bithiophene)] (F8T2).[38] Their analysis yielded a polaron pair radius of ca. 2.2 nm, similar to the values given above for fully conjugated PPV.

In Onsager's theory, the efficiency of dissociation depends on the initial distance between charges $r_0$, which is commonly related to the excess energy of excitation dissipated during the charge transfer process. An important addition to the Onsager theory has been made by Braun, who pointed out that the life time of this geminate pair is not defined by diffusive motion but by a given rate $k_f$.

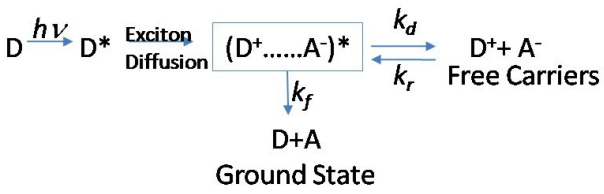


**Figure 11 Schematic diagram for description of Braun's theory for charge carrier separation.**

In Braun's model, the probability that a geminate pair dissociates into charge carriers as a function of electric field is given by:

$$\eta(E) = \frac{k_d(E)}{k_d(E)+k_f} \quad \textbf{( Eq 9)}$$

The rate $k_f$ is, in the simplest case, the luminescence life time of the decay of the geminate pair. It can be measured by fluorescence methods, but there is no direct method for determining $k_d(E)$.

Based on Onsager's initial theory for the dissociation of weak electrolytes[32, 39], Braun derived the dissociation rate $k_d$ to be[40]:

$$k_d(E) = k_d(0)\left[1 + b + \frac{b^2}{3} + \frac{b^3}{18} + \frac{b^4}{180} + \cdots\right] \quad \textbf{(Eq 10)}$$

where $k_d(0)$ is the dissociation constant at zero electric field

$$k_d(0) = K(0)k_r \quad \textbf{(Eq 11)}$$

Here, $K(0) = \frac{3}{4\pi a^3} e^{-\frac{E_b}{k_b T}}$ is the equilibrium dissociation constant at zero electric field, $a$ is, as for $r_0$ defined in Onsager's theory, the initial separation of the e-h pair, $b = e^3E/8\pi\varepsilon_0\varepsilon_r k_b^2 T^2$, and $E_b = e^2/4\pi\varepsilon_0\varepsilon_r$ is the e-h binding energy. Finally, $k_r$ is the constant of bimolecular charge recombination, which can be calculated by using the Langevin relation:

$k_r = \frac{e(\mu_e+\mu_h)}{\varepsilon_0\varepsilon_r}$, with $\mu_e(\mu_h)$ is the mobility of electrons (holes).

Morteani et al. demonstrated Braun's model is not sufficient to explain the excited state properties in polymer blends. In contrast to Braun's model, the geminate e-h pair did not recombine directly via emission of light, but collapsed into an exciplex state which gave rise to a red-shift emission.[41]

Figure 12 summarizes the main findings by Morteani et al. The potential energy curves represent the ground state, the free charge carriers and the initial excited state with the exciton residing on the donor phase. The distance of the exciton from the interface is denoted as $r_{DA}$ and the separation of the geminate pairs is represented as $r_0$.

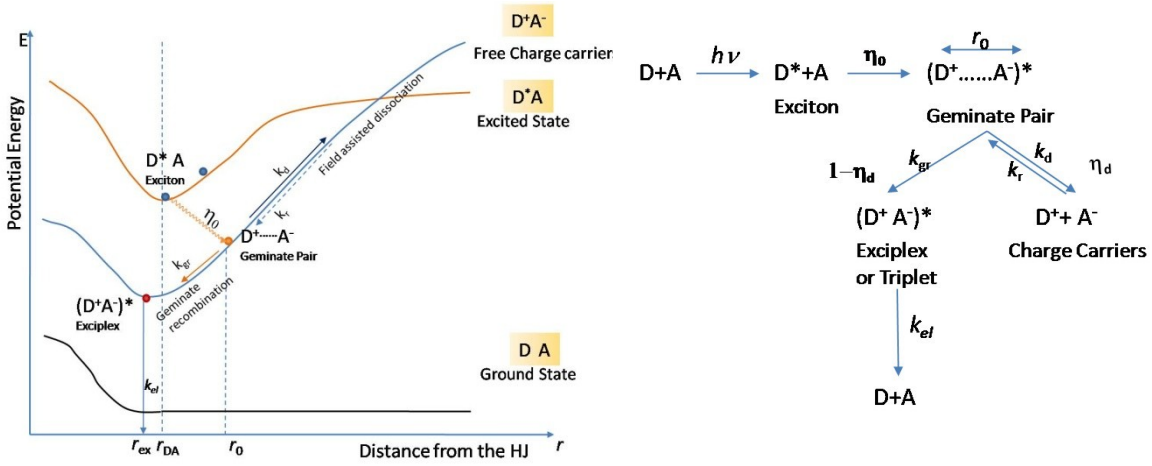


**Figure 12 A schematic representation of photogeneration process and the kinetics of geminate pair dissociation based on the model by Morteani et al. D and A represents the donor and acceptor phase respectively.**

Upon excitation, the exciton is generated in the donor or acceptor phase. It then diffuses to the D-A interface, where it undergoes charge transfer and dissociates to an interfacial geminate e-h pair with a dissociation efficiency $r_0$. This geminate pair can either dissociate with an efficiency $\eta_d$ and a rate constant $k_d$, or recombine with a rate constant $k_{gr}$ to form a luminescent exciplex state[41]. The generated charge carriers may go back to a geminate pair via bimolecular recombination as in Braun's model. The total charge carrier generation efficiency is the product of the geminate pair formation and the geminate pair dissociation. The findings of Morteani et al can be summarized to the following: a) formation of free carriers from a non-emissive (dark) polaron pairs stated not via dissociation of the exciplex. b) the exciplex can be thermally excited to form an interchian exciton which can then undergo again charge transfer at the heterojunction.

The authors could successfully describe electric field dependent photoluminescence quenching experiments by using Onsager's theory to describe the efficiency for polaron pair dissociation. They showed that the separation distance $r_0$ of the geminate pair formed at different polymer heterojunction varies considerably. The blends with large separation distances showed low geminate recombination rates and hence better solar cell performance.

### 2.3.2 Bimolecular recombination and space charge limited current

Recombination may occur between electron-hole pairs arising from a single exciton (geminate recombination) or from two different excitons (non-geminate bimolecular recombination). In the case of non-geminate bimolecular recombination, if the recombination of the charges is controlled by the diffusion of the charge carriers toward each other and in the absence of deep traps, the recombination is often Langevin-type[42] and the bimolecular recombination coefficient can be written as $\gamma_L = \frac{e(\mu_e + \mu_h)}{\varepsilon_0 \varepsilon_r}$

where $\mu_e$ and $\mu_h$ is the mobility of the electron and hole, respectively.

Information on the recombination process in polymer solar cells is often indirectly obtained by the correlation between the photo-generated short circuit current density $J_{sc}$ and the incident light intensity $I_{light.}$. Several authors have reported a power law dependence of $J_{sc}$ upon light intensity $I_{light}$, $J_{sc} \propto I_{light}^{\alpha}$, where α is the scaling exponent, which gives information about the dominant recombination mechanism and ranges typically from 0.5 to 1.[43, 44] At high light intensity, bimolecular recombination becomes more dominant and it may limit the maximum charge that can be extracted from the sample, eventually leading to a upper limit on the efficiency of the solar cell.[45] Since the generation rates of both holes and of electrons are proportional to the light intensity, the probability of bimolecular recombination should be proportional to the product of the hole and electron generation rate. As a consequence, if bi-molecular recombination is the major loss path in the solar cells, the short circuit current should scale with the square-root of the light intensity with $\alpha = 0.5$.[44] Alternatively, if the recombination of the initially formed electron-hole pairs (geminate recombination) is limiting the device efficiency, the short circuit current will scale linearly with the light intensity, $\alpha = 1$. However, α values between 0.85 and 1 were reported for polymer/fullerene based solar cells, where the deviation of α from one was attributed to the loss of carriers via bimolecular recombination.[46, 47] Optimizing the nanomorphology of the phase separation in the D-A bulkheterojunction is the key for both efficient photo-generated exciton diffusion to the donor-acceptor interface within the exciton lifetime, before they recombine to the ground state as well as for reduced bimolecular recombination.[48]

When the transport of both charge carriers is strongly unbalanced, or the mobility of at least one of the charge carriers is considerably low, the accumulation of charges in the semiconductor bulk will occur. These excess charges build up as space charge which modifies the field inside the device. This phenomenon is termed as space charge effect. As a consequence, carriers might reside in the device for large times and bimolecular recombination becomes more significant. In addition, this space charge can affect the field-dependent efficiency for free carrier formation. The maximum current density an intrinsic non-doped semiconductor can transport is equal to the so-called space-charge-limited current (SCLC), which, in the absence of traps, can be calculated from Child's law:

$$J_{SCL} = \frac{9}{8}\varepsilon_0\varepsilon_r\mu\frac{V^2}{L^3} \quad \textbf{(Eq 12)}$$

where $\mu$ is the mobility of the lowest charge transport carrier, $V$ is the voltage and $L$ is the thickness of the active layer. Space charge effects will become important in solar cells, if the number of carrier generated per unit time and area exceeds the space charge limit. Since $J_{SCL}$ is linear in $\mu$, systems with poor transport are more vulnerable to this effect.

### 2.3.3 Charge transport properties

Semiconducting properties of conjugated polymers are attributed to the overlap of the $p_z$-electrons of the carbon atoms along the back bone.[49] Because the length of polymers is much smaller than the thickness of the active layer, slow interchain hopping sets a fundamental limit to charge carrier transport in the polymer bulk. In polymer solar cells, due to the electrostatic interactions between the electrons and holes, two requirements must be fulfilled in order to achieve high charge extraction efficiency: firstly, the mobile charge carrier hopping distance must be larger than the Coulomb radius. However, the charge carrier hopping distance is determined by the property of the polymer for e.g. the length and the regularity of the side chain attachment.[50] New materials need to be developed in order to accomplish this requirement. Secondly the charge carrier transit time $t_{tr}$ must be much smaller than the carrier life time $\tau$.[51] The charge carrier transit time is calculated as $t_{tr} = L/\mu E$. The mobility life time product is therefore an important parameter determined whether or not the energy conversion efficiency is limited by the charge transport and recombination.

Mobility in bulk heterojunction solar cells can be obtained by time of flight[42] (TOF) measurements, determined from the analysis of organic field effect transistors (OFET) [43], or derived from the current-voltage-characteristics of single carrier devices (e.g. hole-only or electron-only device). However, TOF requires a large film thickness (normally at least 1μm), which is more than 10 times thicker than the typical layer thickness with optimum performance. Since the performance of bulk heterojunction solar cells is shown to be strongly morphology dependent, the mobility may also change when increasing the thickness. Mobilities calculated from OFETs resemble the motion of charge carriers in the lateral direction close to a dielectric, which hardly represents the operational condition in solar cells.

Recently, a novel technique called photo-CELIV (charge carrier extraction by linearly increasing voltage after photo excitation) has been introduced to investigate the charge carrier mobility as well as the rate of bimolecular recombination of charge carriers in the same polymer blends as used in the solar cell devices.[44-46]

In Figure 13, we showed a schematic time diagram of the applied voltage and current response to illustrate the measurement principle.

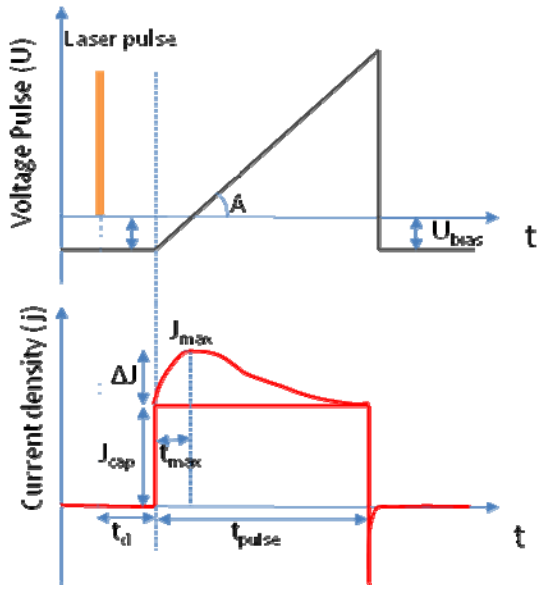


**Figure 13 Schematic drawing of the applied voltage pulse (top) and the corresponding current transient response (bottom) in a photo-CELIV measurement.**

Charge carriers are photogenerated by a short light pulse. They then can either be extracted under built-in potential or undergo recombination. During and after excitation an external forward bias is applied to compensate the built-in potential of the sample, resulting in a near-zero electrical field inside the polymer layer.

After a delay time $t_d$, a linearly increasing voltage pulse with the slope $A=U_{bias}/t_{pulse}$ is applied to the sample to extract the equilibrium charge carriers. The extracted current densities are monitored by a digital oscilloscope. If only one type of carrier is motive, the current transient will feature a single maximum with amplitude $J_{max}$ at a delay time $t_{max}$ after starting the extraction voltage ramp. From the measured current transients, the charge mobility can be calculated as $\mu = 2d\left[3t_{max}^2\left(1+0.18\,\Delta j/j_{cap}\right)dE/dt\right]^{-1}$, where $j_{cap} = \varepsilon\varepsilon_0 dE/dt$ is the capacitive charging current density and $\Delta j = j_{\max} - j_{cap}$.[57, 58] 57-59 The charge density left after the delay time $t_d$ can be approximately calculated from $n = \epsilon\epsilon_0/\left(e\mu j_{cap}\right)j'(t_d)$, where $e$ is the elementary charge and $j'(t_d)$ is the time derivative of the current at time $t_d$.[58]

# Chapter 3 Sample preparation and characterization

## 3.1 Solar cell sample preparation

### 3.1.1 Cleaning and pre-treatment of ITO substrates

In this thesis, glass coated with ca. 100nm indium tin oxide (ITO, Merck) is used as the transparent electrode. The glass substrate has a square shape of 2.5×2.5 $cm^2$. In order to achieve the desired geometry of the bottom electrode, the substrate was first covered with 1 cm wide TESA® tape and then submerged into a $FeCl_3$ (in 1M HCl) etching bath at 60°C for 5 min. The structured ITO substrates were washed with plenty of water right after etching. Then, a four step cleaning procedure with acetone, hemanex (3% water solution), milli-Q water and isopropanol in sequence was performed to remove the organic and inorganic impurities on the ITO surface. For each cleaning step, the substrates were placed in a glass sample holder filled with the washing solvent and the sample holder was placed in an ultrasonic bath for 15 minutes. Afterwards, the washing solution was first poured away and the substrates were then rinsed with milli-Q water to ensure that no organic solvent remained on the sample surface. After the last washing step, the substrates were stored in isopropanol solution. Before use, they were retreated in an ultrasonic bath and then dried under nitrogen stream. A 50 nm thick conductive polymer polystyrene sulfonic acid doped poly(3,4-ethylenedioxythiophene) (PEDOT:PSS) (Baytron AI 4083 purchased from HC Starck) was spin-coated on the entire substrate to reduce the surface roughness. PEDOT:PSS is a hole-transporting polymer and it has work function of 5.1 eV[60, 61] about 0.3 eV higher than that of ITO (4.8 eV).[62, 63] This leads to a reduction of the hole transport barrier and effectively block the electron back transfer. Before the spin-coating of PEDOT:PSS, oxygen plasma treatment (Tepla Plasma System 200G) was applied to the ITO substrates to ensure that no impurities were attached to the surface and to make the ITO surface more hydrophilic, allowing better wetting with the conductive polymer layer.

### 3.1.2 Deposition of the active organic layer

3.1.2.1 Solution deposition

Polymers were dissolved in a suitable solvent, which in this thesis is chlorobenzene if not specified otherwise. If needed, the polymer solution was placed on a hot plate (at 80ºC) with continuous stirring for ca.10 min and then ultrasonicated for 30 min to form a homogeneous solution. Polymer film spin-coating was done by taking 100 µl of the solution with a pipette and immediately dropping this onto the substrate. The spin coater was started directly after dropping the solution and the rotation time was set according to the experimental needs. The final polymer films were studied as-prepared or annealed. The as-prepared films were kept in the transfer chamber of a glove box under a nitrogen atmosphere at $10^{-1}$ mbar over night to ensure complete evaporation of the solvent. The annealed films were obtained by directly placing the samples onto a hot plate with constant temperature.

3.1.2.2 Thermal deposition

Most of the small molecules used in organic light emitting diodes (OLED) or organic solar cells cannot be solution processed due to their poor solubility. Vacuum thermal evaporation hence is often used for deposition of small molecules. One of the advantages of thermal deposition is that it permits high levels of purity of the result film. Thermal deposition allows sequential stacking of well-defined layers, which permits efficient extraction of charges. The evaporator used in this work was built by BESTEC GMBH and was specially designed according to our experiment requirements. A top view of the evaporator source system is simply sketched in Figure 14. Six conical crucibles were arranged symmetrically in the evaporator on the bottom part. Two metal evaporator source boats were placed in the inner circle. After thermal evaporating of the organic layer, the top electrodes could be directly deposited without the need to transfer the sample to another evaporator.

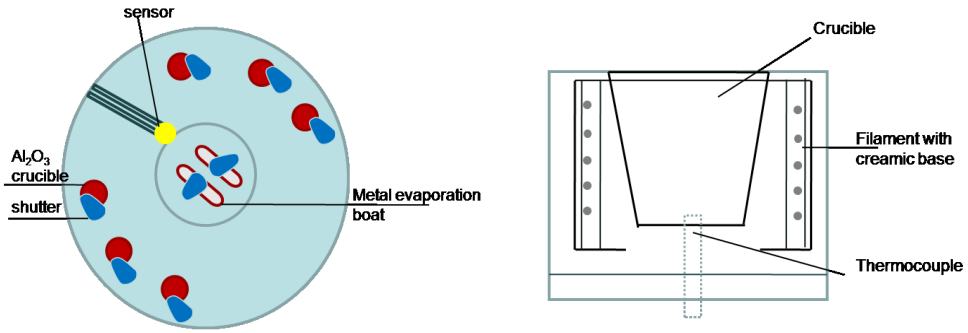


**Figure 14 left: illustrated top view of organic molecule evaporator source system. right: close view of the structure of a crucible.**

The evaporator crucibles are made from alumina ($Al_2O_3$), and placed inside a resistive heater. The resistive heater consists of a tungsten filament supported by a ceramic base. Temperature control is done via a thermocouple having close contact to the bottom of the crucible. Therefore the direct control of the deposition is ensured. Generally, thermal gradient sublimation is applied before the thermal evaporation in order to achieve high levels of purification.[64] Due to the limited amount of material, the molecule used in this thesis was evaporated directly without any purification. The evaporation occurred at high vacuum at about $1\times10^{-7}$ mbar. A typical growth rate used here is 0.3 Å/s where the evaporator crucibles temperature is in the range of 190-210°C. Too low growth rate had a danger of adsorbing contaminants onto the surface at a higher rate than the organic molecules, whereas growth is extremely difficult to control if the growth rate is too high.[65]

### 3.1.3 Top electrode evaporation

After the solution deposition of the active organic layer, the samples were transferred into the metal evaporator chamber, where the top electrode materials were thermally deposited directly onto the active layer through a metal mask. By placing the masks with the pixels properly arranged with respect to the etched ITO stripe, 6 individual pixels with the active area of each cell defined by the cross-section of the top electrode and the ITO stripe, here typically between 0.12 and 0.2 $cm^2$, were formed (see Figure 15).

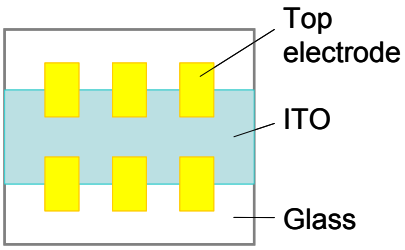


**Figure 15 Planar view of the cathode pattern with 6 pixels. The vertical stripe in the middle represents the etched ITO area.**

The top electrode materials used in this thesis are calcium (Ca) and aluminium (Al). Suitable amounts of the metals were placed in the source boat on the lower part of the evaporation chamber. The chamber was then closed after closing the source shutter and the sample shutter. Vacuum was applied and the evaporation started when the pressure reached $2\times10^{-6}$ mbar. Since the metal source position is fixed, the sample plate was to rotate slowly to obtain a homogeneous film. The current through the boot was regulated to keep the evaporation rate constant. The source shutter and sample shutter were opened when the metal started to evaporate and when the evaporation rate became constant. For the solar cell devices described in this thesis, a 30 nm Ca layer was first evaporated on the polymer film, followed with a 100 nm Al layer as a protective layer. After the evaporation step, the devices were stored in the glove box for further characterization. For the photoluminescence kinetic studies silver (Ag) was utilized as an $O_2$-protective layer.

## 3.2 Photovoltaic Characterization

### 3.2.1 Spectral photocurrent measurement

The spectral photocurrent was recorded with a homemade setup. The sample was placed in a measurement-box which has 7 copper contacts, one for the ITO and the other six for the pixel electrodes. The illumination light was generated by an Oriel 150W Xe-lamp. The incident light was first chopped with a chopper at 140 Hz frequency, and then monochromatized via an Oriel Cornerstone 260 monochromator before it was guided by a fused silica fiber of 1mm diameter to the device. The photocurrent was detected with a lock-in-amplifier which only amplified the signal modulated with a frequency of 140 Hz. Therefore, the noise was dramatically reduced, allowing a signal down to 100 nV to be detected. The

number of photons incident on the sample was calculated at each wavelength by using a calibrated Si-diode (SN1316).

### 3.2.2 White light efficiency measurement

Current-voltage (I-U) curves were recorded by exposing the sample to a constant intensity of white light generated by a Steuernagel HK solar simulator. The light power was measured with a Gentec pyroelectric power meter. A Keithley 2400 Source Meter was used for applying the bias voltage and recording the current. All devices were measured under the illuminating intensity of 100 $mW/cm^2$ at the air mass 1.5 (AM 1.5) specifications. For studying the dependence of the photocurrent on the incident light intensity, a set of neutral density filters with transmission coefficients from 0.01 to 0.5 were placed between the sample and the white light source. The resulting light intensity was inferred from the product of the original light intensity and the transmission coefficient of the used gray filters. All measurements in glove box were at $O_2 < 1$ ppm and $H_2O < 1$ ppm.

# Chapter 4 Charge carrier generation and electron blocking at interlayers in polymer solar cells

## 4.1 Introduction

So far the most efficient polymer based solar cells are usually fabricated from blends of electron and hole-accepting materials. Because the D-A interface is much larger in the blend than in the bilayer devices, the goal of a higher efficiency of exciton dissociation is accomplished without reducing the overall thickness of the active layer. However, in these blend devices, a percolated path for the carriers to travel to the electrodes is required for efficient charges extraction, and the photocurrent was shown to be very much sensitive to the nanoscale morphology. [66-68] Hence, it is quite meaningless to use this type of device structure as a model to study charge carrier generation. When trying to understand the performance of solar cells, it is important to start from a simpler system with well characterized polymers. Ramsdale et al. performed detailed studies on polyfluorene-based devices with a simple bilayer structures. With this bilayer structure, the contributions of bimoleculear recombination can be almost neglected.[69] This dramatically reduces the number of variable parameters in the analysis of the device performance. [66]

In this chapter we presented a novel interlayer technique for preparing double layer devices from soluble polymers. In order to demonstrate that a well defined heterojunction rather than a diffuse layer is formed in bilayer device, the film surface potential were measured by Kelvin probe. The results were compared with those obtained from normal blend structures and with pure single layer films. At the end, a detailed study is undertaken in comparing the photocurrent characteristics of bilayer structures and blend devices.

## 4.2 Materials: PFB and F8BT

The two conjugated polymers [poly(9,9-dioctylfluorene-2,7-diyl-*co*-bis-N,N´-(4-butylphenyl)-bis-N,N´-phenyl-1,4-phenylenediamine)] (PFB) and [poly(9,9-di-octylfluorene-2,7-diyl-*co*-benzothiadiazole)] (F8BT) (see Figure 16 for the chemical structures) have been used here since they were intensively studied for the understanding of fundamental processes in polymer solar cells. PFB is a copolymer with alternating fluorine and triphenylamine subunits.

Triphenylamines have excellent hole transport properties and have been used in photoconductors and LEDs. [70] Hole mobilities of PFB up to 2 * $10^{-3}$ $cm^2V^{-1}s^{-1}$ have been reported by Redecker et al. as measured by time-of-flight. [71] The large offset between the highest occupied molecular orbital (HOMO) and lowest unoccupied molecular orbital (LUMO) levels of the two polymers (0.8 eV and 1.24 eV respectively)[72] indicates that efficient charge transfer should occur between PFB and F8BT. The strong photoluminescence quenching in this blend further confirmed that this combination is suitable for solar cell investigation. It is for this reason, combined with their stability and the good hole transporting properties of PFB, that we employed this polymer system for this study. Both polymers used here were obtained from American Dye Source (ADS).

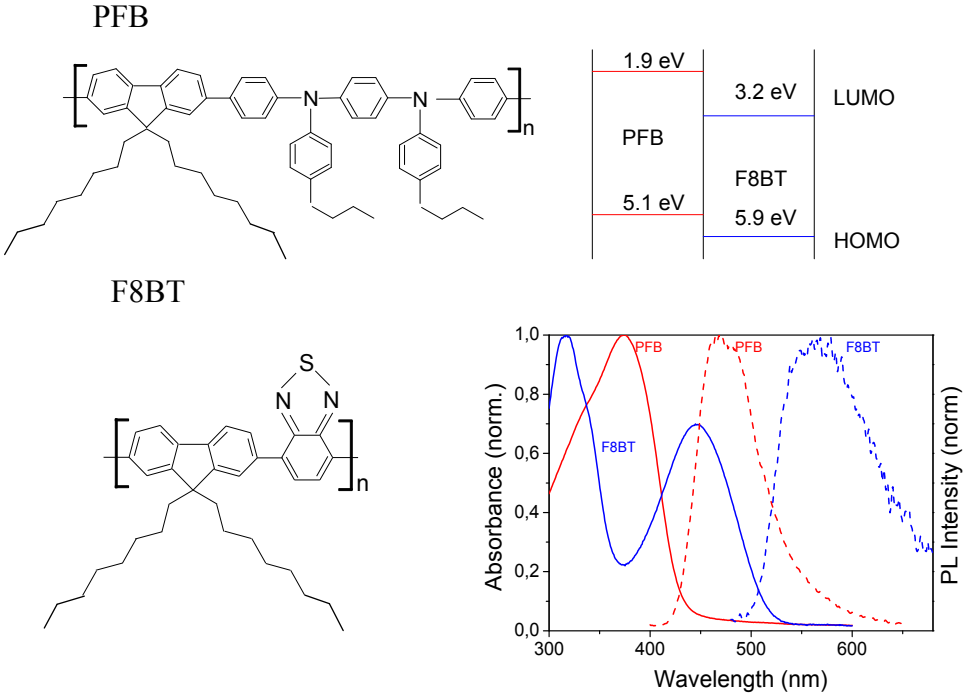


**Figure 16 Chemical structures, energy levels and the absorption photoluminescence spectra of the two fluorene polymers (PFB and F8BT) studied in this chapter.**

## 4.3 Application of the interlayer concept to PV cells

In this section, we will present a novel technique to prepare double layer solar cell devices. An easy and classic approach towards bilayer structures from solution is using selective solvent for the two different layers. Unfortunately, most conjugated polymers exhibit similar solubilities in most organic solvents. Direct coating of a second layer on top of the first layer will partially dissolve or at least swell the first layer, leading to an undefined interface.

High efficiencies for all-polymer solar cells were reported for bilayer devices produced by laminating a polythiophene derivative (POPT) with a cyano-substituted poly(phenylenevinylene) (MEH-CN-PPV) as the electron acceptor (ECE = 1.9%).[73] However, this procedure is rather complicated and experience is required to achieve a good film. Further the laminating technique still has to prove its applicability for large area devices.

More recent Kim et al. published an elegant approach to form thin insoluble polymer layers (so-called interlayers) on conducting polymer anodes, hence allowing the construction of polymeric multilayer from solution.[74] They produced the interlayer by first spin-coating a poly(2,7-(9,9-di-n-ocylfluorene)-alt-(1,4-phenylene-((4-sec-buylphenyl)imino)-1,4-phenylene)) (TFB) solution directly on top of PEDOT:PSS layer, followed by annealing the entire structure at 180°C (> $T_g$ of TFB) for 1 h. After the film was cooled down, the remaining soluble part of TFB was removed by spin-rising the film with a solvent. The authors named the resulting thin (~10 nm) insoluble layer an 'interlayer'. The performance of electrophosphorescent OLEDs comprising interlayer polymers with different positions of the electronic levels was studied by Yang et al.[75] They observed a significant increase in efficiency upon increasing the energies of the highest occupied molecular orbital (HOMO) and of the lowest occupied molecular orbital (LUMO) of the interlayer polymer. This effect was interpreted in terms of efficient electron-blocking at the interface between the emission layer and the interlayer. The performances of these devices were quite comparable to those comprising cross-linked hole-transporting/electron-blocking layers, indicating that the interface between the interlayer and the active layer coated ontop is well defined.[76]

With the aim of investigating the properties of charge carrier generation, three configurations of samples were prepared as shown in Figure 17. Type I and type II structures have a PFB interlayer between the PEDOT:PSS anode and the active layer, while type III contains a single PFB:F8BT blend layer.

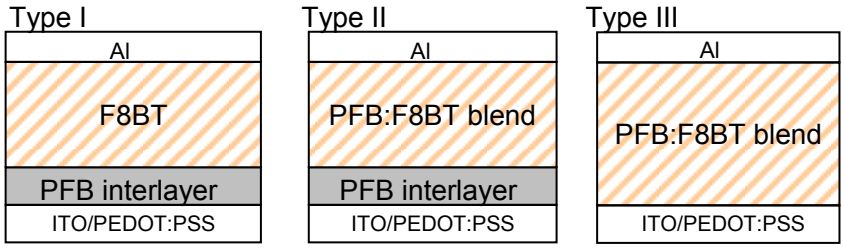


**Figure 17 Configuration of the three types of multicomponent polymer solar cell structures. All cells have the active layer sandwiched between the PEDOT:PSS anode and a 80nm aluminium cathode. Type I: Bulk F8BT layer on top of PFB interlayer, Type II: PFB:F8BT blend layer on top of PFB interlayer, Type III: only PFB:F8BT blend layer. The PFB interlayer thickness is around 6 nm.**

This interlayer was prepared by spin-coating the hole transporting polymer (PFB) onto the PEDOT:PSS coated ITO anode, followed by annealing of the entire structure at 150°C (the temperature above the glass transition temperature of PFB) for about 30 minutes. Then, the entire sample was washed with the same solvent used for spin coating, in this case chlorobenzene, to remove the soluble PFB fraction. As a result, a ca. 6 nm thick (as determined by UV-Vis absorption spectroscopy) interlayer of insolubilized PFB remained on the PEDOT:PSS anode. The formation of the insoluble interlayer is not yet fully understood, but it is proposed due to the binding of polymer individual chains at the surface of PEDOT:PSS.[75]

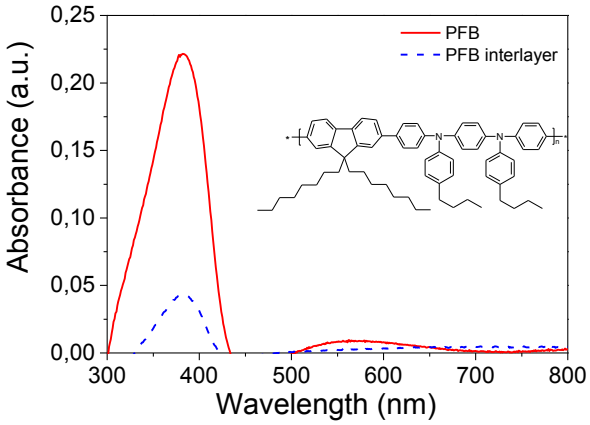


**Figure 18 The absorbance of a spin-coated PFB layer (solid line) and the insoluble PFB interlayer (dashed line).**

## 4.4 Film surface potential studies by Kelvin probe

The electron blocking function of the interlayer was first investigated by measuring the change in surface potential upon illumination with Kelvin Probe

directly on the multilayer sample (without Al electrode) shown in Figure 17. Kelvin probe (KP) has recently become an important tool for the investigation of the surface potential of organic semiconductors. In the study of Polymer/Fullerene based solar cells with Kelvin force microscopy (KFM), Hoppe et al. observed that the work function changed when more PCBM accumulated on the surface, which they attributed to a higher electron density under illumination.[77] Together with high resolution scanning electron microscopy (SEM), they were able to draw conclusions concerning the electron transport toward the cathode in the solar cell configuration.

In this subchapter, we aim to study the electron blocking effect of the interlayer by comparing the light-induced surface potential changes in three different device structures. Note that all measurements were performed in air. For a quantitative study of the work function, samples would need to be kept under ultrahigh vacuum (UHV) conditions, since adsorbates strongly alter the work function of the surface. Nevertheless, since we consider only the light-induced shift of the potential, absorbate related effects shall be of minor importance.

For the type I structure, with a 50 nm thick pure F8BT layer on top of a pure PFB interlayer, the light-induced surface potential change is about -260 mV (see Table 3).

**Table 3 Change in surface potential upon illumination with a super bright blue LED (emission maximum at 475 nm), as measured with the Kelvin probe method. The measurement is conducted in air. The changes in surface potential of the pure polymers are also listed.**

| | **Type I** | **Type II** | **Type III** | **Reference I** | **Reference II** |
|---|---|---|---|---|---|
| Active layer | PFB interlayer F8BT | PFB interlayer PFB & F8BT | PFB& F8BT | PFB | F8BT |
| $\Delta\phi$ | -260mV | -60mV | -50mV | -10 mV | -80 mV |

* **The Kelvin probe measurements have been performed by Björn Pieper.[78]**

We attributed this to the efficient photo-generation of charges across the PFB/F8BT interface. This finding implies that the PFB(interlayer)/F8BT interface efficiently suppresses the interdiffusion of photo-generated electrons and holes across this interface. In contrast, the type III devices which comprises a PFB:F8BT blend on PEDOT:PSS, exhibits a photoinduced change in the surface potential of only –50 mV. This is between the values measured for a pure PFB

layer (reference I, $\Delta\phi$=-10 mV) and a pure F8BT layer (reference II, $\Delta\phi$=-80 mV) on PEDOT:PSS. Presumably, the photoinduced change in surface potential for the type III structure as well as for the reference devices lies in a weak accumulation of electrons in the semiconducting polymer layer at the PEDOT:PSS/polymer interface, due to the electron-blocking function of PEDOT:PSS.[79]

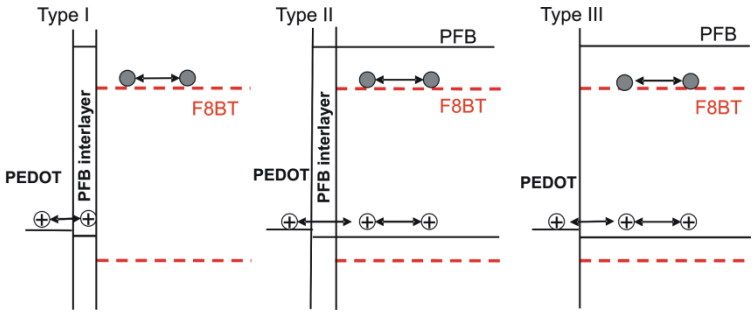


**Figure 19 Proposed model for illustrating charge transfer in the three types of devices upon illumination. The energy levels of PFB and F8BT are shown with solid and dashed lines, respectively.**

In order to support our interpretation that the bilayer type I structure consists of a sharp heterojunction and does not comprise a diffuse PFB:F8BT layer (which might form when spin-coating F8BT on top of the immobilized PFB film), we studied type II devices contains also a PFB interlayer but with a blend layer ontop. Interestingly, this type shows a rather small change in the surface potential upon illumination, though the PFB interlayer might also act as a barrier for electrons. The photo-generated change in the Kelvin voltage was only –60 mV, which is in the same range as the type III device without interlayer. We ascribe this to the backflow of photo-generated holes from the interlayer into the hole-transporting PFB component of the blend, which effectively suppresses the buildup of considerable charge across the interface (see Figure 19). We conclude that devices of type I exhibit a defined heterojunction, which allows for directional photoinduced charge transfer, and that this sharp heterojunction effectively suppresses the interdiffusion of holes and electrons.

## 4.5 Photovoltaic properties

Solar cell of these three type configuration (with Al top electrode) were characterized. Figure 20 shows the normalized external quantum efficiencies of the complete photovoltaic device of type I, compared to the normalized photoaction spectra of the other types of devices. Aluminum has been chosen

because of the large barrier for the injection of both electrons and holes into the active polymer layer, thereby reducing the contribution by bimolecular recombination of injected charges to the overall current. Because the type I device contains only a ca. 6 nm thick PFB interlayer but a 50 nm thick F8BT layer, the IPCE spectrum of this structure has the highest F8BT contribution. Nevertheless, the PFB contribution is still dominant, suggesting efficient dissociation of excitons formed within the PFB interlayer at the interface to F8BT.

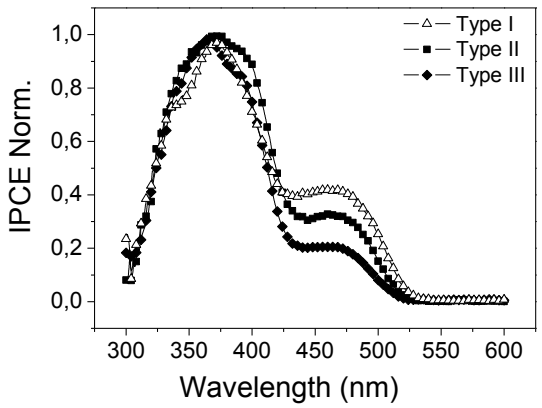


**Figure 20 Normalized quantum efficiency spectra of the three types of solar cell structures. The thicknesses of the active layers were around 40-50 nm.**

The photocurrent-voltage characteristics of the bilayer structures are shown in Figure 21, in comparison with that of the respective blend device. Because the introduction of the interlayer largely affects the dark current characteristics, we will focus our discussion on the photocurrent density $J_{ph}$, which is the difference between the current density under illumination, $J_L$, and in the dark, $J_D$. As shown in Figure 21, the photocurrent characteristics of the type I device is highly asymmetric: while the magnitude of photocurrent increases continuously with increasing negative bias, it becomes nearly zero for a bias larger than ca. 1 V. Apparently, the photogeneration of current is largely inhibited at a large positive bias, which is equivalent to the internal electric field pointing upwards from the PEDOT:PSS anode to the Al cathode. Since the PFB(interlayer)/F8BT interface is efficiently blocking electrons located in the F8BT layer to move into PFB (and holes located in the PFB interlayer to move into F8BT), field-induced dissociation of the geminate pair into free electrons and holes is inhibited if the internal electric field points upwards.

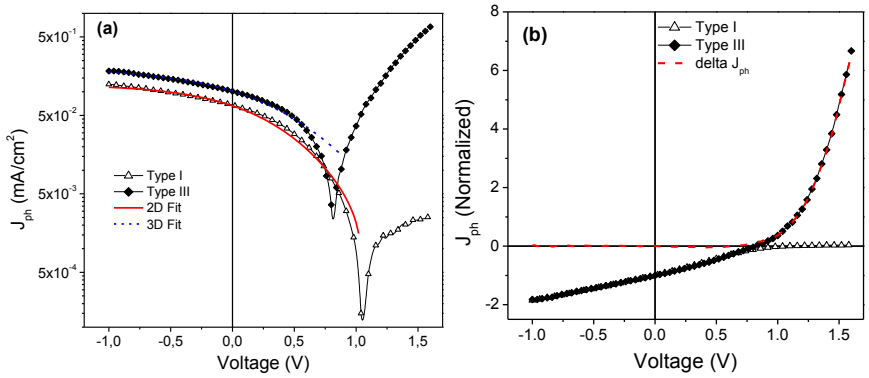


**Figure 21 (a) Photocurrent density as function of external bias for a type I (triangles) and a type III (diamonds) devices under AM 1.5 illumination. The PFB interlayer thickness is around 6 nm; the active layer has a thickness of 65-70 nm for both devices. The solid line shows the fit of the photocurrent characteristics to Eqs. (13) and (14), the dashed line is the best fit to Eqs. (13) and (14). Both fits take into account only the efficiency of carrier photogeneration. (b) the same data normalized to the same value at zero bias. The dashed line is the difference between the normalized characteristics of the type III and type I devices.**

On the other hand, for sufficiently small positive or even negative bias, the dissociation of the geminate pair will be assisted by the internal electric field and the photocurrent will be determined by the efficiency of charge generation at the heterojunction and the collection of charges at the corresponding electrodes. According to J. Barker et al., the dissociation rate $k_d$ of geminate pairs at a planar interface as a function of the internal electric field $E$ follows the relation[80]:

$$k_d(E) = k_d(0) M^{-1} \left[ \exp[M] \left(1 - M^{-1}\right) + M^{-1} \right] \qquad \textbf{(Eq 13)}$$

$$M = \frac{e}{k_b T} \sqrt{\frac{-eE}{\pi \varepsilon_0 \varepsilon_r}}$$

Here, $k_d(0)$ is the zero-field dissociation rate. The electric field which we assume to be constant across the active layer is related to the external bias by $E = (V\text{-}V_{bi})/L$, with $V_{bi}$ the build-in potential (at which the photogenerated current becomes zero) and $L$ the thickness of the layer. If the recombination of geminate polaron pairs at the interface is the only loss process, the field-dependence of the photocurrent density is simply given by:

$$J_{ph}(E) = C \frac{1}{1 + k_r / k_d(E)} I_{light} \qquad \textbf{(Eq 14)}$$

with $k_r$ defined in Eq 11. $I_{light}$ is the incident light intensity and $C$ is a constant, which depends, among others, on the geometry of the device, the intensity profile within the device and the absorption coefficients of the used materials.

Substituting Eq 13 to Eq 14 yields:

$$J_{ph}(E) = C \frac{1}{1 + k_r / k_d(0) \cdot M^{-1} \cdot \left[\exp\left[M\right]\left(1 - M^{-1}\right) + M^{-1}\right]} \cdot I_{light} \qquad \textbf{(Eq 15)}$$

The open circuit voltage has been taken as the build-in potential of the bilayer device ($V_{bi}$ = 1.04 V). If we take $L$ = 70 nm, $T$ = 295 K and $\varepsilon_r$ = 3.5, the only adjustable fit parameter here is the ratio between $k_r$ and $k_d(0)$. As shown by the solid line in Figure 21a, an excellent fit to the photocurrent characteristics of the type I device can be obtained by applying equation (15) with $k_{rec}$/ $k_{diss}(0)$ = 60. The small discrepancy at voltages close to the build-in potential is most likely caused by an additional current contribution due to carrier diffusion and by the bimolecular recombination of charges at the PFB:F8BT interface.[66, 80, 81]

Finally, we like to discuss the shape of the photocurrent characteristics for the blend device. As expected, the $J_{ph}(U)$ curve of the blend is less asymmetric than that of the bilayer structure. Also, the type III device exhibits a smaller apparent build-in voltage $V_{bi}$ (0.82 V compared to 1.04 V for the bilayer device). This effect has been reported earlier by H.J. Snaith et al when comparing PFB:F8BT blend and laminated bilayer devices.[82] For voltages larger than the build-in potential, the blend device exhibits a positive photocurrent, which increases rapidly with bias. In the blend device, holes can travel through the whole active layer by moving within the PFB phase, giving rise to a hole-only current at positive bias. This current might be largely affected by photogenerated charges, e.g. via photocurrent multiplication processes.[83, 84] It is most likely due to this additional photocurrent contribution, that the apparent build-in potential of the blend device is smaller than that of the strict bilayer.

Despite these obvious differences, the shape of the photocurrent characteristics of the blend device (type III) is very similar to that of the defined bilayer for voltages smaller than the apparent build-in potential Figure 21), implying that similar processes determine the photocurrent in both cases. For blend devices, Schilinsky

and coworkers have recently suggested that the photocurrent in the forth quadrant of the I-V-characteristics is largely affected by the mean drift distance of carriers, which may be smaller than the thickness of the active layer for low electric fields.[85] Our data suggest that this effect is of minor importance in our blend devices.

According to the Braun theory for charge carrier dissociation in a three-dimensional isotropic media, as we already introduced in the introduction part of this thesis, equation 13 can be rewritten as a three dimension form:

$$J_{ph}(E) = C \frac{1}{1 + \dfrac{k_r}{k_d(0) \cdot [1 + b + \dfrac{b^2}{3} + \dfrac{b^3}{18} + \ldots]}} \cdot I_{light} \qquad \textbf{(Eq 16)}$$

A reasonable fit to the photocurrent characteristics below ca. 0.6 V was obtained with the above equation. The curve in Figure 21b has been calculated with the same parameters as for the fit of the bilayer device, namely with the same build-in voltage but with a somehow lower value for $k_{rec}/ k_{diss}(0)$ of 25. This difference is quite understandable having in mind the different micro morphologies of bilayer and blend samples. The good fit to Brown's model is in support of our conclusion that the photocurrent characteristics of the blend device is governed by field-dependent charge carrier dissociation.

## 4.6 Conclusion

By showing the change of the surface potential measured by Kelvin probe under illumination we provide evidence that the combination of an interlayer of an electron-donating polymer with a spin-coated layer of an electron-accepting material forms a well defined heterojunction rather than a diffuse layer. As a consequence, solar cells made from these solution processed bilayer devices exhibited a highly asymmetric photocurrent characteristics, with an almost complete suppression of photocurrent generation at positive bias. We also find that the photocurrent characteristics of such a bilayer structure can be well fitted by taking into account only the dissociation and recombination of geminate polaron pairs at the interface between the electron-donating interlayer and the electron-accepting top layer. The photocurrent in this bilayer device is almost exclusively determined by the field-dependent carrier generation at the internal interface. Comparable studies on blend devices suggest that the efficiency to form

free carriers is the determining process in these polymer-polymer solar cells, regardless of whether photoinduced charge transfer occurs inside a blend or across a distinct interface. In fact, the photocurrent characteristics of bilayer and blend devices were found to be quite similar. As bimolecular recombination is of minor importance in the bilayer geometry, this similarity suggests that the interplay between dissociation and recombination of photogenerated geminate pairs determines the properties of these polymer-polymer solar cells.

# Chapter 5 Excited state and photovoltaic properties of PPV based polymer solar cells

In chapter 4, bilayer devices prepared with a novel interlayer approach were presented where the polyfluorenes PFB and F8BT are used as model compounds. The experimental results gave strong evidence that the efficiency to form free carriers is the determining process in polymer-polymer solar cells, regardless of whether photo-induced charge transfer occurs inside a blend or across a distinct interface. However PFB and F8BT are not a good choice for efficient solar cells since they barely absorb beyond 500 nm. Compared to these polyfluorenes, polyphenylenevinylenes (PPV), show a broader and red-shifted absorption and spin-coated solar cells from PPVs are known to exhibit good photovoltaic properties.

By using the blends of M3EH-PPV and CN-Ether-PPV, a ECE of 1.7% was achieved recently.[7] Even though, efficiencies of polymer-polymer-based devices are still far lower than those reported for blend systems based on the electron accepting component PCBM, which recently exceeded 5%. [86, 87, 88] Though 95% of photoluminescence from M3EH-PPV was quenched by CN-Ether-PPV, as determined by the PL quenching experiments, an IPCE of 31% shows that the collected charge carriers account to less than one third of the quenched excitons. The initial results from Yu showed a subliner relationship ($J_{sc} \sim I^{0.86}$) between the short circuit current intensity $J_{sc}$ and the incident light intensity I, indicating charge carriers loss via bimolecular recombination. Additionally, Offermans et al. proposed field enhanced triplet yield to constitute an important loss mechanism for the blend of MDMO-PPV and a derivative of CN-PPV. [89]

In this chapter, our goal is identifying the loss mechanism in solar cells based on blends of M3EH-PPV and CN-Ether-PPV. In our optical studies, we first present results of detailed steady state investigations on pure polymers and as well on 1:1 polymer blend. The excited state dynamic is studied by performing time-resolved photoluminescence measurements. To demonstrate the applicability of the proposed mechanism, we compare the performance of polymer blend solar cells with different degree of intermixing of the D-A components as well as solar cells with different device architectures. Further, the influence of bimolecular recombination and space charge limited current on this system was studied by

investigating the dependence of the photocurrent on incident light intensity and electric field.

## 5.1 Introduction to PPV polymer based solar cells

In 1995, the first all-polymer solar cells with moderate efficiency was reported by Yu and Halls, where MEH-PPV was used as electron donor and CN-PPV as electron acceptor.[5, 6] These two polymers absorbed in complementary spectral regions between 300 nm and 550 nm. Solar cells comprising the blend of these two polymers achieved promising photovoltaic properties with IPCE ca. 5% and energy conversion efficiency close to 0.1%, which were about 20 times larger than of devices made with pure MEH-PPV and even ~100 times larger than from pure CN-PPV. Later on, a much more improved efficiency was obtained by replacing the CN-PPV with CN-ether-PPV, where an ether group was introduced to increase the solubility.[90] In 2000, significant progress was made by using the copolymer M3EH-PPV as donor and CN-Ether-PPV as acceptor. Breeze et al. demonstrated solar cells with IPCE of 24% corresponding to 0.6% power conversion efficiency.[91] After further device optimization, an even higher efficiency (ECE=1%) was published by the same authors.[92] However the low fill factor of 25% left room for further improvements. In 2005, solar cells composed of the same polymer blends but with an improved processing procedure was fabricated by Kietzke et al.[7] In their work, a large open circuit voltage of 1.34 V, an external quantum efficiency IPCE of 31% and a white light power conversion efficiency of 1.7 % have been achieved. Recently, an even higher peak IPCE of 42% was achieved by Koetse et al.,using a mixture of poly(2-methoxy-5-(3,7-dimethyloctyloxy)-1,4-phenylenevinylene) (MDMO-PPV) as the donor, and the alternating copolymer poly(9,9-dioctylfluorene-2,7-diyl-alt-1,4-bis(2-(5-thienyl)-1-cyanovinyl)-2-methoxy-5-(3,7-dimethyl-octyloxy) benzene (PF1CVTP) as the acceptor, though their devices exhibited a slightly lower energy conversion efficiency ($\eta$=1.5 %).[8] In Table 4 we summarize the characteristic parameters of solar cells based on PPV polymer blends. The data show that both the fill factor and the quantum efficiency need to be doubled in order to reach 6-7% energy conversion efficiency. [93] Recent experiments on PPV-based blends showed that annealing the layer leads to an improvement of the efficiency by a factor of two compared to the as-prepared layers.[94] The corresponding photophysical studies

revealed that this improvement was accompanied by a strong reduction of emission from an interfacial exciplex. This anticorrelation suggests the photovoltaic properties of the PPV-based blends to be determined by the efficiency for polaron pair separation, similar to what has been concluded in chapter 4 for polyfluorene-based blends.

**Table 4 Characteristic parameters of solar cells based on PPV polymer blends**

| Donor | Acceptor | IPCE | $V_{oc}$ | FF | ECE | Reference |
|---|---|---|---|---|---|---|
| MEH-PPV | CN-PPV | 6% | 0.6V | | | [5]* |
| M3EH-PPV | CN-Ether-PPV | 24% | 1.0V | 25% | 1.0% | [92] |
| MDMO-PPV | PF1CVTP | 42% | 1.4V | 37% | 1.5% | [8] |
| M3EH-PPV | CN-Ether-PPV | 31% | 1.4V | 35% | 1.7% | [7] |

*illuminated at 0.15mW/cm$^2$

## 5.2 Materials: M3EH-PPV and CN-Ether-PPV

Two PPV-based polymers were studied in this chapter: Poly[2,5-dimethoxy-1,4-phenylene-1,2-ethenylene-2-methoxy-5-(2-ethylhexyloxy)-(1,4-phenylene-vinylene-1,2-ethenylene)] M3EH-PPV and CN-Ether-PPV. The chemical structures and corresponding energy levels of these two polymers were shown in Figure 22. M3EH-PPV got its name from the three methoxy and one ethylhexyloxy side chain attached to the polymer backbone. It can be regarded as a strictly alternating copolymer of the soluble MEH-PPV and the insoluble 2,5-dimethoxy-PPV. M3EH-PPV was first synthesized by the Horner reaction [95] in the group of Prof. Hörhold, Jena, and has optical properties very similar to the well characterised MEH-PPV. However, it is much less soluble than MEH-PPV due to the short length of the side-chains. Compared to MEH-PPV, M3EH-PPV has much higher glass transition temperature ($T_g$=113°C). This high glass transition temperature indicates a more ordered structure. As a hole-transport material, M3EH-PPV has a hole mobility on the order of $10^{-3}$ cm$^2$/Vs [96] at 300 K as measured from organic field effect transistor, which has been found to be almost twice of the zero field mobility of MEH-PPV. The average weight molecular weight of M3EH-PPV we used in this thesis is about 44,000kg/mol.

The CN-Ether-PPV, (poly[oxa-1,4-phenylene-1,2-(1-cyano)-ethylene-2,5-dioctyloxy-1,4-phenylene-1,2-(2-cyano)-ethylene-1,4-phenylene], used here has two dioctyl side chains attached to the central phenylene vinylene of the repeat

unit. The addition of an ether linkage along the backbone in CN-ether-PPV is used to improve the solubility, but it is also likely to disrupt the conjugation and affect the chain packing morphology due to increased flexibility in the chain at the sites of conjugation breaks.[97] Broken conjugation has been found to disrupt energy and charge migration in conjugated polymers.[98] The molecular weight of this polymer was $M_n$=12,000 g/mol and it exhibited a $T_g$ of 62°C.

Both M3EH-PPV and CN-ether-PPV were provided by Professor. Hörhold and Dr. Tillmann at the University of Jena in Germany.

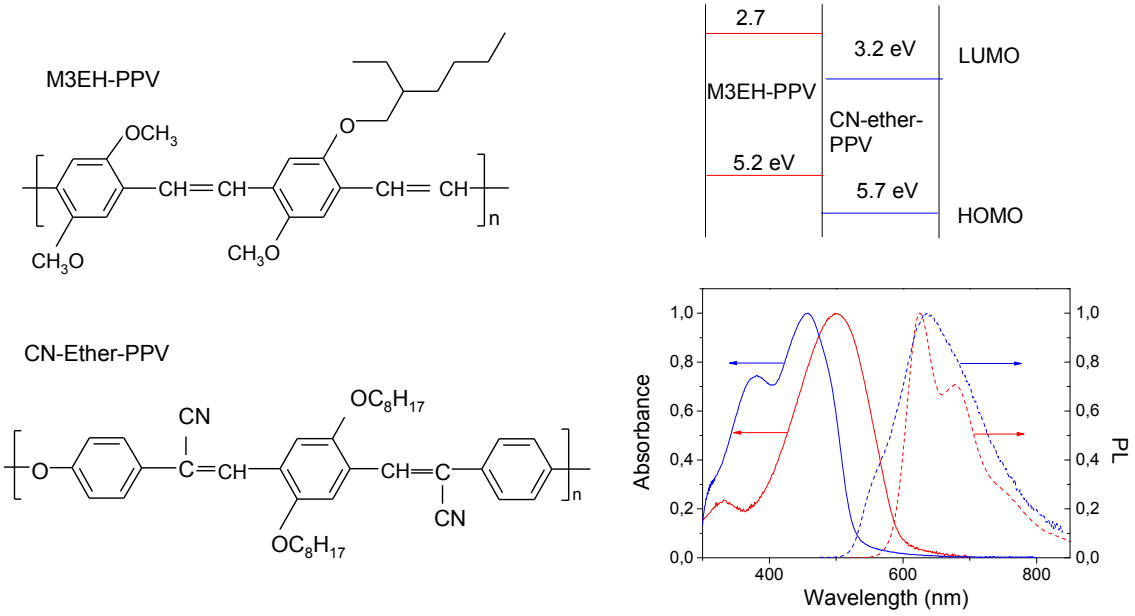


**Figure 22 Chemical structures, energy levels and the absorption photoluminescence spectra of the electron donor polymer M3EH-PPV and electron acceptor polymer CN-Ether-PPV studied in this chapter.**

In polymer blends, sufficient offset (ca. 0.1-0.4 eV) between the LUMO levels of the electron donor and the electron acceptor is required for efficient charge separation. On the other hand, a high energy difference between the LUMO level of the acceptor and the HOMO of the donor material is needed for achieving high open circuit voltage. Compared to the well known electron acceptor PCBM, CN-Ether-PPV has the LUMO level of -3.2 eV, which is 700 meV higher than that of PCBM. Thus, the blend of M3EH-PPV and CN-Ether-PPV should lead to a high $V_{oc}$.

## 5.3 Spectroscopy studies

### 5.3.1 Theoretical background

As discussed in introduction part, an electron is excited to the upper energy level upon absorption of light and leaving behind a hole in the HOMO. As one of the main difference from inorganic materials, the photo-excitation in organic semiconductors does not generate free charges but bounded electron-hole pair (exciton). Before the exciton essentially separates into free charge carriers, several different intermediated states can be formed. Hence, the degree of charge separation may vary from a tightly bound pair to completely separated charges. In Figure 23, three of the general recognized forms are sketched.

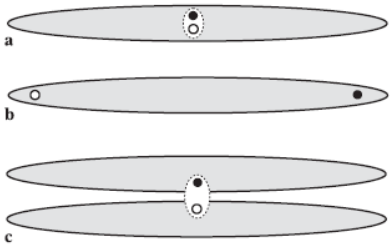


**Figure 23 Schematic representation of e-h pair formations in organic semiconductor. a) intra-chain exciton b) geminate polaron pair, with the exciton extending over a few adjacent molecular units c) inter-chain exciton, excimer (or exciplex). The long ellipse denotes one conjugated segment of a polymer chain and electron and hole are represented as filled and open circles, respectively.**

It is generally accepted that singlet excitons (Figure 23 a) are first generated in organic semiconductor after excitation.[99, 100] This electron-hole pair remains on the same chain bound together by their electrostatic attraction (columbic attraction). It may essentially recombine by releasing their energy as heat or light emission. In order to dissociate the pair efficiently the exciton binding energy must be overcome. The use of a D/A dissociation interfaces with a energy offset between the HOMO and LUMO levels higher than the exciton binding energy is necessary to achieve high current.

For solid polymer layers, the close proximity of π-conjugated chains can also result in the formation of interchain excitations, with the electron and the hole residing on adjacent chains such as excimers or exciplexes. These excitations are stabilized by interchain interactions. There has been a continuous debate on the importance of interchain interactions when regarding optical excitations in dense layers of conjugated polymers. Despite Greenham et al. provide strong evidence

that singlet excitons are the dominant product of photo-excitation in PPV,[101] Yan et al. demonstrated that in films of MEH-PPV only 10~20% of absorbed photons generate excitons, the majority lead to long-lifed excitations.[6,102] The authors measured the photoluminescence of pure MEH-PPV and the blend of MEH-PPV and nonemissive polystyrene. In the latter case, inter-chain interactions are unlikely. They came to the conclusion that the long-life excitation results from inter-chain interactions. As an evidence, the inter-chain interaction were dramatically reduced if the distance between the polymer chains was strongly increased.

An excimer is a pair of identical molecule (or polymer chain) whose electron wave function is delocalized over both molecules in the excited state but not in the ground state. When the two molecules (or polymer chains) consists different materials, an exciplex is formed. The formation of excitons, excimers and exciplexes is sketched in Figure 24.

$$D + h\upsilon \longrightarrow D^* \text{ (exciton)}$$
$$D^* + A \longrightarrow D^*A \text{ (exciplex)}$$
$$D^* + D \longrightarrow D^*D \text{ (excimer)}$$
$$A^* + A \longrightarrow A^*A \text{ (excimer)}$$

**Figure 24 illustration of exciton, exciplex and excimer formation. D and A represented the ground states of donor and acceptor molecules respectively. D* or A* denoted the excited states.**

The photoluminescence from an excimer (or exciplex) is characterized by a broad and structureless red-shifted emission spectrum,[103] and long radiative lifetimes. This delayed relaxation may lead to an increased probability of trapping and recombination of bounded electron hole pairs which will not contribute to the output current in solar cell devices and consequently represent an additional loss channel.

Beside excimers and exciplexes, interchain interactions can also lead to the formation of aggregates, where the electronic wave function is delocalized over two or more chains in the ground state as well as in the excited state [104]. For the case of aggregates, an additional shift of both absorption and emission should be present. An important feature to distinguish aggregate and excimer is that aggregate emission can be directly excited, while excimer emission is always excited via an intra-chain exciton.

The influence of intra- and inter-chain interactions on the photoluminescence (PL) spectra of conjugated polymers, especially PPV polymers, is currently a topic of great interest.[89, 94, 105-109] As the nature of the charge separated state is crucially important for the performance of solar cells. Steady state photoluminescence and time-resolved PL is a well established tool to investigate the excited state dynamics of conjugated polymers.

### 5.3.2 Steady state and time-resolved photoluminescence studies

In this section, we like to review our previous photospectroscopy studies on M3EH-PPV and CN-Ether-PPV as well as their 1:1 blend films. Part of the data were adapted from my master work and repeated here to provide a deeper and more detailed understanding. Note that these earlier PL studies were not correctly calibrated for the instrumental response at longer wavelength. All spectra shown here have been recalculated using the proper calibration curve. So that the PL spectra showed here might looked different as shown in our previous publications.[27, 94, 110]

#### 5.3.2.1 Steady state PL measurements

We performed steady state PL measurements on both pure M3EH-PPV, CN-Ether-PPV solution dissolved in chlorobenzene and on their solid films, respectively. Compared to the dilute solution, the PL spectrum of the M3HE-PPV solid film is ca. 32 nm red shifted but it still keeps a similar shape as the PL spectrum measured in solution. This red shift can be understood by considering that excitons formed in the bulk can migrate to the chains with the longest conjugation lengths. In contrast the PL spectra of CN-ether-PPV show a large difference between the solution and the solid film. The PL spectrum of the solid film is broad, structureless and 100 nm red shifted compared with that in solution. These results indicate the presence of an additional emitting species in the CN-Ether-PPV solid film, most likely an inter-molecular excitation such as a physical dimer or an excimer.

A quantitative comparison of the photoluminescence showed that the overall PL of the blend film was considerably quenched relative to the neat films. As is shown in Figure 25, the PL of M3EH-PPV:CN-Ether-PPV is quenched to about 5% of the pure M3EH-PPV layer emission, indicating that 95% of the excitons are

dissociated. These values shall be compared to the 99% of the emission quenching obtained from 1:1 blend of M3EH-PPV and PCBM. Apparently, CN-Ether-PPV functions well as an electron acceptor when combined with M3EH-PPV, nearly as good as the well studied PCBM.

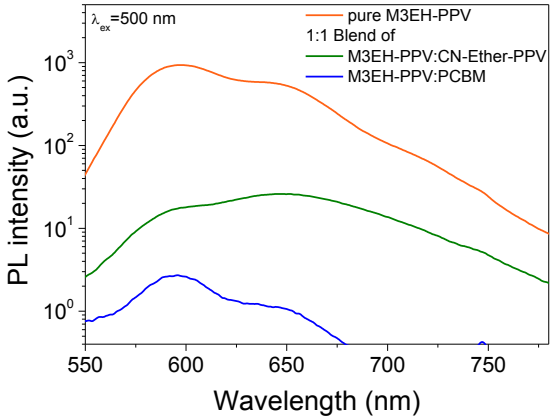


**Figure 25 PL measured from pure M3EH-PPV film, 1:1 blend of M3EH-PPV:CN-Ether-PPV. The PL of 1:1 blend of M3EH-PPV:PCBM film is shown as a comparison of the quenching.**

Surprisingly, a new feature appeared at ca. 670 nm in the PL spectrum of the M3EH-PPV:CN-Ether-PPV blend film, which is present neither in the emission of the pure polymer layers nor in the spectrum of a 1:1 blend of M3EH-PPV and PCBM. After changing the excitation wavelength from 450 nm (excitation mostly of CN-Ether-PPV) to 550 nm (excitation solely of M3EH-PPV), the 670 nm emission still remained and the PL intensity decreased by a factor of two (Figure 26). This decrease can be partially attributed to the weaker absorption at 550 nm. All the observations indicate that a new emitting species is formed in the blend film and that it can be excited either via the donor or the acceptor phase. Broad and red-shifted emission spectra have recently been reported for a variety of blends of electron-donating and electron-accepting polymers and attributed to an interchain exciplex.[41, 89, 111-114]

In contrast to the PL of CN-Ether-PPV which increased slightly after annealing, probably due to a better packing of the chains, the absolute PL intensity of the annealed blend at 670 nm was almost half of the as prepared film. However, the PL intensity of the blend at 600 nm did not significantly change upon annealing.

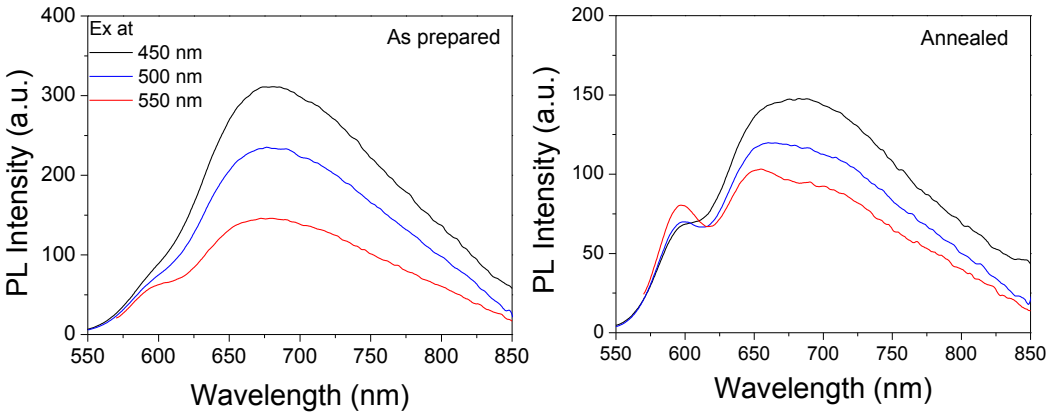


**Figure 26 The PL spectra of a 1:1 (weight ratio) M3EH-PPV:CN-Ether-PPV blend film excited at different wavelengths. The absolute PL intensity of the film is shown before and after annealing.**

There is no noticeable emission below 550 nm (even when exciting the sample at the absorption maximum of CN-ether-PPV), implying that the exciton on the electron acceptor is fully quenched in the blend. The shape of the overall spectra remains the same for all excitation wavelengths. Therefore, emission from the CN-Ether-PPV excimer must be very weak. As pointed out by Chasteen et al., the very long lifetime of both the exciton and the excimer in CN-ether-PPV will make these species particularly vulnerable to be quenched.[111] In order to resolve the nature of the 670 nm emission, time-resolved spectroscopy studies were performed.

### 5.3.2.2 Time-resolved PL measurements

In our previous work a detailed time-resolved spectroscopy study was performed on the pure polymers and on their 1:1 blend film coated from chlorobenzene. The photoluminescence of M3EH-PPV film is characterized by a fast luminescence decay with the time constant considerably below 0.8 ns. This short time scale is typical for intra-chain recombination in conjugated polymers.[115, 116] The decay time is relatively insensitive to the emission wavelength. Thus, there is no indication that more than one emitting species is present.

In Table 5 we summarized the emission decay time constants obtained from the transients of CN-Ether-PPV dilute solutions and its solid films. Since chlorobenzene is a good solvent for this polymer and low concentrations were used, we believe that the polymer chains are well separated in solution and that the emission from CN-Ether-PPV in solution is solely from intra-chain singlet

excitons on isolated chains. This is supported by the very weak effect of the emission wavelength on the PL decay.

**Table 5 Emission decay times of CN-Ether-PPV in dilute solution and in the solid film coated from chlorobenzene.**

| Emission | 500 nm | 600 nm | 650 nm | 700 nm |
|---|---|---|---|---|
| Solution | 1.7 ns (98%)<br>0.3 ns (2%) | 1.8 (91%)<br>0.8 (9%) | | |
| Solid film | 0.6 ns (43 %)<br>7.1 ns (34%)<br>2.5 ns (23%) | 7.9 (61%)<br>3.0 (36%)<br>0.5 (3%) | 8.4 ns (65%)<br>3.4 ns (35%) | 8.8 ns (66%)<br>3.8 ns (34%) |

It was reported that CN-PPV has a similar chemical structure like CN-Ether-PPV. However the PL life time of CN-PPV in solution[107] is appear half as long as the one we measured in CN-Ether-PPV solution. The same result was observed by Chasteen, et al. who performed detailed studies on the effect of the broken conjugation on the spectroscopy behavior of CN-PPV. They proposed that the longer life time in CN-Ether-PPV solution originates from the reduction of the ability of single-chain excitons to visit quenching sites, due to the broken conjugation.[111]

Unlike M3EH-PPV, the decay of the emission from a CN-Ether-PPV solid film is found to be dependent on emission wavelength. Beside a short life time component dominating at 500 nm, which can be attributed to intra-chain exciton recombination, in addition two longer components of around 8 ns and 3 ns could be identified. We assigned the longer components to interchain excimer emission. From the magnified emission of Figure 27a, an obviously emission build-up can be observed for emission at 650 nm and 700 nm. In the first few nanoseconds after the pulse, the number of emitted photons rises steeply as indicated by the arrows in Figure 27b. This indicates that the species responsible for the 650 nm emission is not formed immediately upon photo excitation of the polymer. This is a typical characteristic of excimer formation. Also, this build-up is accompanied by a fast decay of the intra-chain exciton emission at ca. 500 nm.

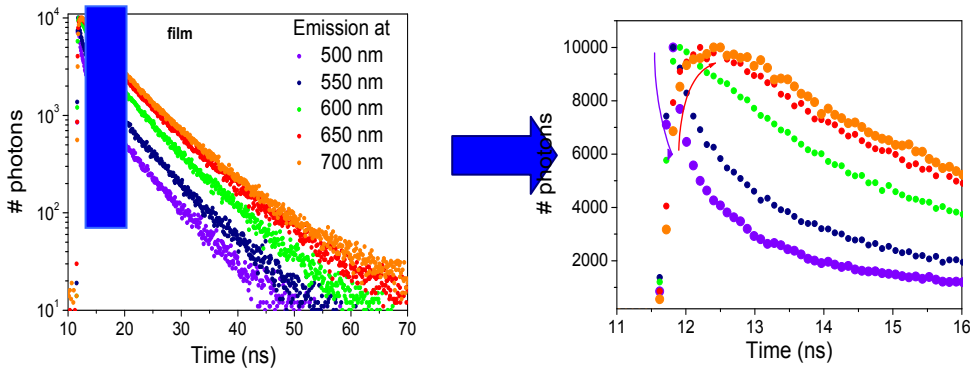


**Figure 27 a) Time resolved transients of a CN-Ether-PPV solid film for an excitation wavelength of 400 nm. b) The transients in the first few nanoseconds after the excitation pulse are shown on a shorter timescale. An emission build-up is marked with a red arrow for the emission at 650 nm and 700 nm. (Graphs are adapted from my master thesis [110])**

Also, the absence of a vibronic structure in the steady state emission spectrum of CN-Ether-PPV film is indicative of excimer emission. Note that Chasteen et al. reported that the decay time constant of CN-Ether-PPV film at 700 nm is dominated by a long component of 14.0 ns, which is almost twice as long as our measurement results. Detailed studies on the impact of film thickness on the emission decay dynamic were performed by the same group on M3EH-PPV and CN-ether-PPV film.[97] They demonstrated that decay times were shorter for thinner versus thicker films which they attributed to greater interchain interactions in the thinker films, probably due to more pronounced aggregation. This argument is reasonable since the films we measured are all around 50 nm instead of 150 nm studied in Chasteen's work.

Results from our previous studies on the emission decay time of the as-prepared and annealed M3HE-PPV:CN-ether-PPV blend layers was summarized in Table 6.

**Table 6 Fluorescence decay times for the M3EH-PPV:CN-Ether-PPV blend layer spin-coated from chlorobenzene solution**. **(Table is adapted from my master thesis [110])**

| Emission | 600 nm | | 650 nm | |
|---|---|---|---|---|
| | As prepared | 110°C annealed | As prepared | 110°C annealed |
| Dominant τ | 0.35 ns (**52%**) | 0.07 ns (**71%**) | 2.2 ns (57%) | 0.4 ns (**63%**) |
| | 1.9 ns (26%) | 0.9 ns (**14%**) | 5.8 ns (34%) | 1.7 ns (27%) |
| | 5.5 ns (12%) | 2.9 ns (15%) | 0.23 ns (**9%**) | 4.9 ns (10%) |

Clearly, the emission decay at 600 nm is dominated by the shortest time constant whereas the 650 nm emission is dominated by the long decay component. This leads to the conclusion that the steady state PL emission at 600 nm is caused by

recombination of excitons on M3EH-PPV while the emission at 670 nm involves inter-chain processes. After annealing, the component of fast emission decay at 600 nm increased to 85%. Also the 650 nm emission was now dominated by this short component. Together with the findings from the solid state PL measurements it seems reasonable to attribute the 670 nm emission in the blend to the formation and recombination of an exciplex formed between M3EH-PPV and CN-Ether-PPV chains. This exciplex forms in less than 1 ns, which is below the time needed to form an excimer in CN-Ether-PPV as demonstrated before. Following the ideas first proposed for a blend of polyfluorene derivatives (PFB:F8BT) we suggest that after dissociation of the excitons no free charge carriers, but so called geminate pairs are formed.[117, 118] As is stated in the introduction part, this geminate pairs will then either recombine via exciplex emission or nonradiatively recombination or may dissociate further into completely free charge carriers.

## 5.4 Anticorrelation between exciplex emission and photovoltaic properties

### 5.4.1 Motivation

In the last section we showed strong evidence for exciplex formation in these PPV-based blends. It was shown in our earlier work that the exciplex formation is suppressed after the blend has been annealed above the glass transition temperature of the two polymers.[94] We attributed this change to the increase of intermolecular distance or interaction at the heterojunction. Upon annealing, phase separation between the donor and acceptor components is presumably induced, which effectively weakens the inter-chain interactions leading to exciplex emission.

In this section, comparable studies are performed with a copolymer of MEH-PPV and M3EH-PPV in combination with CN-Ether-PPV. The correlation between relative exciplex emission and the photovoltaic performance of the blend devices was investigated. In addition, a comparative study was performed on defined bilayer and blend devices. As pointed out in the previous chapter, exciplex formation is minor important in bilayer devices, secondly, bimolecular recombination should be largely reduced. If a low IPCE is due to bimolecular

recombination, resulting in poor charge collection, the overall shape of current voltage characteristics should strongly differ for the blend and bilayer devices.

### 5.4.2 Polymer blend

MEH-M3EH-PPV, poly[2-methoxy-5(2´-ethylhexyloxy)-1,4-phenylenevinylene]-b-poly[2,5-dimethoxy-1,4-phenylenevinylene-2-methoxy-5-(2-ethylhexyloxy)-1,4-phenylenevinylene], is the copolymer of MEH-PPV and M3EH-PPV, which has similar HOMO/LUMO levels like M3EH-PPV. However, the solubility of MEH-M3EH-PPV in common solvents like chlorobenzene is much higher than that of M3EH-PPV due to the higher amount of solubilizing MEH-sidechains.

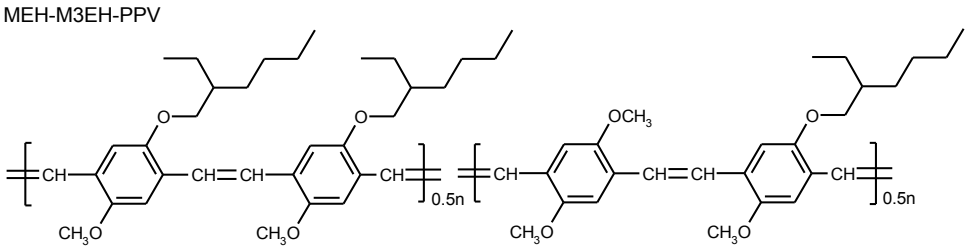


**Figure 28 The chemical structures of the MEH-M3EH-PPV.**

By mixing either M3EH-PPV or MEH-M3EH-PPV with CN-Ether-PPV, polymer blends with different nano-morphologies were obtained. For both blends, the photoluminescence was strongly quenched, indicating that nearly all photogenerated excitons are separated at the donor/acceptor heterojunction. This implies an almost complete intermixing of the D-A components.

As shown in Figure 29, the emission spectra of the prepared blend films of both mixtures exhibit a broad peak centered at ca. 670 nm. As discussed in the previous section, the origin of the 670 nm emission is identified as an exciplex between M3EH-PPV (or MEH-M3EH-PPV) and CN-Ether-PPV.[94] Since MEH-M3EH-PPV has a much higher solubility than M3EH-PPV, this undoubtly results in a better intermixing with CN-Ether-PPV. Therefore, more exciplex emission contribution in the PL spectra is expected. It is presumed that these exciplexes form either directly upon dissociation of an intrachain exciton or via a “dark” polaron pair. Most important, the PL spectra of the M3EH-PPV:CN-Ether-PPV blend layer (Figure 29 (a)) exhibit an additional residual of M3EH-PPV exciton emission at ca. 600 nm, while the emission of MEH-M3EH-PPV:CN-Ether-PPV

blend consist almost entirely of exciplex emission. This indicates a higher degree of intermixing than for the M3EH-PPV:CN-Ether-PPV combination. No emission of the CN-Ether-PPV (λ= 575-590 nm) could be detected in both cases.

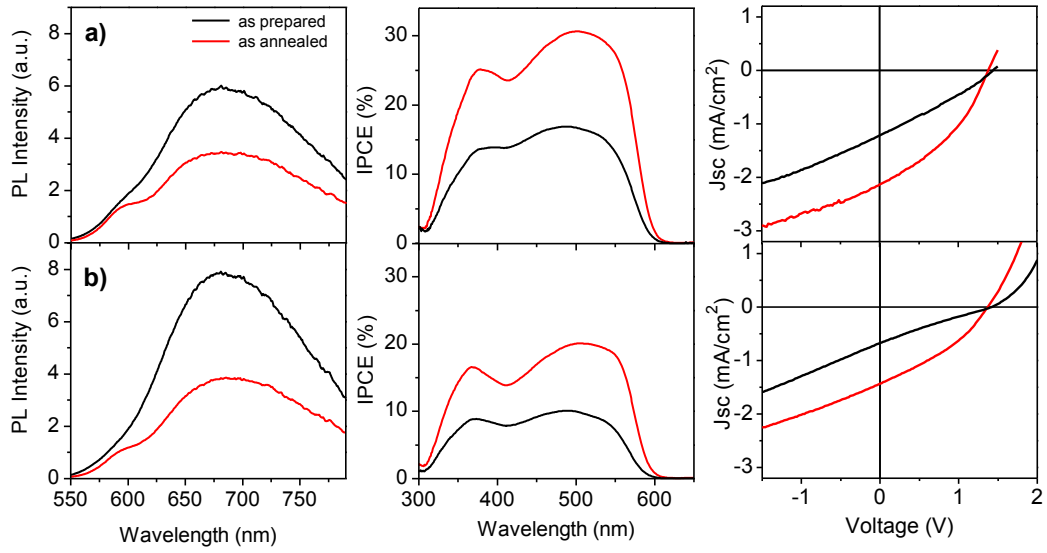


**Figure 29 The PL spectra, external quantum efficiency sprectra (IPCE) and I-U characteristics of blend layer of (a) M3EH-PPV:CN-Ether-PPV (1:1 by weight) and (b)MEH-M3EH-PPV:CN-Ether-PPV (1:1 by weight). The as-prepared samples is shown as black lines, and red lines represent samples after annealing at 130° C for 30 min. For the PL measurement, the polymer solution is directly spin-coated on glass and the sample is excited from glass side. Solar cell devices have the structure as follows: glass/ITO/PEDOT:PSS (50 nm)/PPV blend (55 nm)/Ca/Al.**

Despite the strong intermixing and the complete quenching of exciton emission, the as-prepared MEH-M3EH-PPV:CN-Ether-PPV blend device exhibited a rather low IPCE of less than 8%, compared to the 16% with M3EH-PPV as the donor (Figure 29c,d). After annealing the layers at 130°C, the exciplex emission was greatly reduced in both cases. This effect can be attributed to a certain degree of demixing, leading to a decrease in interfacial area between donor and acceptor polymer and thus reducing the probability of exciplex formation. The decrease in exciplex emission goes along with a significant increase in the IPCE (by a factor of nearly two).

This observation suggests a direct correlation between exciplex emission and the generation of free carriers, in agreement with data published for blends of polyfluorene-based copolymers[117] and on PPV derivatives.[112, 119] By performing time- and field dependent studies on polyfluorene blends, Morteani et al.[41] concluded that exciplexes and free charge carriers have a common precursor, most probably a non-emissive geminate pair. Alternatively, Offermans et al.[119]

proposed that free charge carrier generation involves direct field-induced dissociation of the exciplex. Irrespective of the exact microscopic mechanism, there should exist a direct anticorrelation between the intensity of exciplex emission and photovoltaic efficiency. This is nicely observed in our two blend devices. Apparently, the efficiency of free carrier generation is strongly related to the exact nano-morphology of the sample, which itself depends on the miscibility of the two components or on the thermal history of the sample. The results also show that a certain degree of demixing in polymer blends is a necessary condition for achieving high efficiencies with these polymer-polymer solar cells.

### 5.4.3 Bilayer

In section 5.4.2 we demonstrated that annealing reduced the exciplex emission, while the solar cell efficiency was increased. We attributed this to a higher degree of phase separation. However solar cell performance improvements resulting from annealing has also been attributed to the improvement of charge transport, due to better ordering of polymer chains within one phase.[87] Here we will study the effect of annealing on the efficiency of the bilayer devices. The bilayer devices were fabricated following the interlayer approach presented in Chapter 4. A ca. 10 nm thick insoluble M3EH-PPV interlayer was first prepared. Followed, this layer is covered by spin-coating a 60 nm layer of CN-Ether-PPV, resulting in a defined bi-layer device.

As shown by the emission spectra in Figure 30, we observed only a weak exciplex contribution when exciting the bi-layer at 550 nm, while no exciplex emission was observed when exciting predominately CN-Ether-PPV at 450 nm.

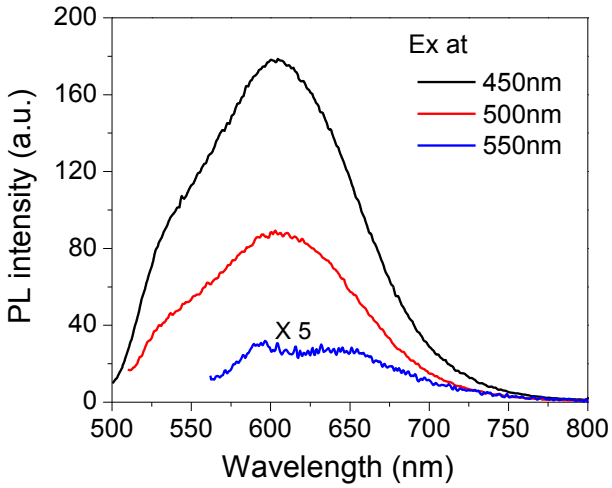


**Figure 30 a) PL spectra of M3EH-PPV (10 nm interlayer)/CN-Ether-PPV (60 nm) bi-layer film. The photoluminescence intensity is measured under different excitation wavelengths 450, 500 and 550 nm, the excitation was incident from the CN-Ether-PPV side.**

Apparently, the degree of intermixing is very low in these bi-layer structures. We like to note that Carter et al. have studied M3EH-PPV/CN-Ether-PPV bilayer devices made by subsequent spin coating. Recent studies by Kietzke et al. suggested that this procedure leads to noticeable intermixing rather than to a strict bilayer.[120]

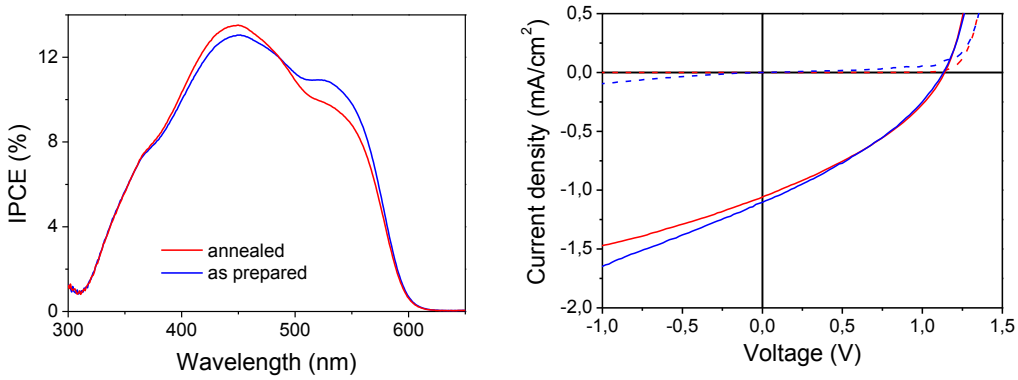


**Figure 31 IPCE spectra and I-U characteristics of the as prepared and the annealed bi-layer devices. The annealed sample was baked at 130°C for 30 minutes while the as-prepared sample was dried under nitrogen atmosphere over night.**

Most noticeably, annealing of the complete bi-layer had almost no effect on the IPCE (Figure 31). This provides strong evidence that the increase in the performance of the blend devices upon annealing, as described above, is mainly caused by changes in the nano-morphology and not by improved transport due to better ordering of the polymer chains within one phase.

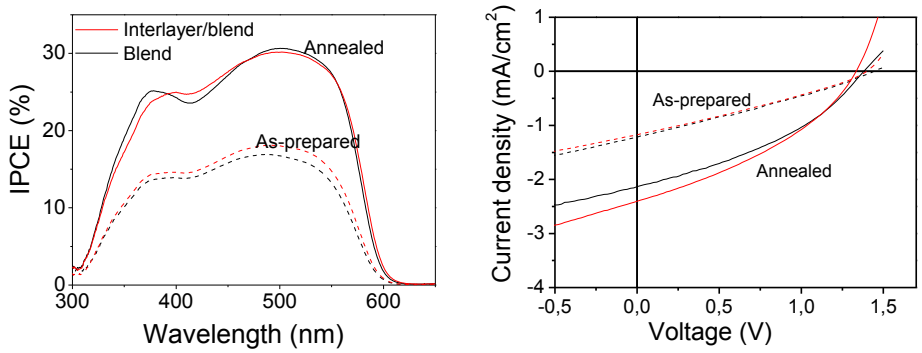


**Figure 32 IPCE spectra and I-U characteristics of devices with polymer blend (black) or polymer blend on top of a M3EH-PPV interlayer (red) as active layer. Solid and dashed lines represented the results from annealed and as prepared samples respectively.**

Alternatively, Veenstra suggested that annealing improves charge transport across the polymer-anode interface.[121] To test this hypothesis, we studied as-prepared blend devices either on pure PEDOT:PSS or after deposition of a thin M3EH-PPV interlayer. A pronounced interrelation between thermal history and device efficiency could be observed again, if the interlayer was covered with a spin-coated blend (see Figure 32 the black solid and dashed lines). Also, the IPCE was quite the same for devices with and without an interlayer. Since the fabrication of the interlayer involves already annealing of the PEDOT:PSS/polymer sample, the correlation between thermal history of the active layer and the photovoltaic performance must be caused by changes of the nanomorphology. Interestingly, as list in Table 7, the fill factors of the defined bi-layer were identical to those of the annealed blends. This implies that the effect of bimolecular charge carrier recombination on the I($V$) characteristics for the blend devices is of minor importance regarding the value of FF.

**Table 7 Performance of M3EH-PPV:CN-Ether-PPV based blend or bi-layer solar cells.**

| | Annealing | IPCE | Voc | FF | ECE |
|---|---|---|---|---|---|
| blend | N | 17% | 1.36 V | 29% | 0.48% |
| | Y | 31% | 1.33 V | 37% | 1.1% |
| bi-layer | N | 13% | 1.13 V | 34% | 0.35% |
| | Y | 14% | 1.14 V | 35% | 0.42% |

### 5.4.4 Effect of electric field and incident light intensity on the photocurrent in blend devices

In this section we present studies of the relation between photocurrent and incident light intensity as well as electric field, with the aim of determinating the possible effect of bimolecular recombination of free charge carriers and the build-up of space charge on the I($V$) characteristics of our solar cell.

As discussed in the introduction part in Chapter 2, photogenerated charges can either recombine geminately or non-geminately. In the absence of trap sites, non-geminate recombination is a bimolecular reaction. As a result the photocurrent follows a square root relation with excitation density, in contrast to a linear dependence in case of geminate pair recombination. Therefore, light intensity dependent measurements are often used to identify the process governing the recombination dynamics.

The photocurrents of annealed M3EH-PPV:CN-Ether-PPV blend devices scales linearly with light intensity for all bias voltages tested, even when varying the thicknesses of the active layer from 55 nm to 150 nm. This is further supporting the conclusion we have drawn in the previous section, that the bimolecular recombination plays a minor role in this blend system. The low efficiency and low fill factor showed in the blend devices must originate from other losses.

The photocurrent - light intensity dependence measured under different bias voltages (-1V, 0V, 1V) of a device with 150 nm layer thickness is shown as an example in the inset of Figure 33. Again, a linear dependence is seen even for the case, that the external bias approaches $V_{oc}$.

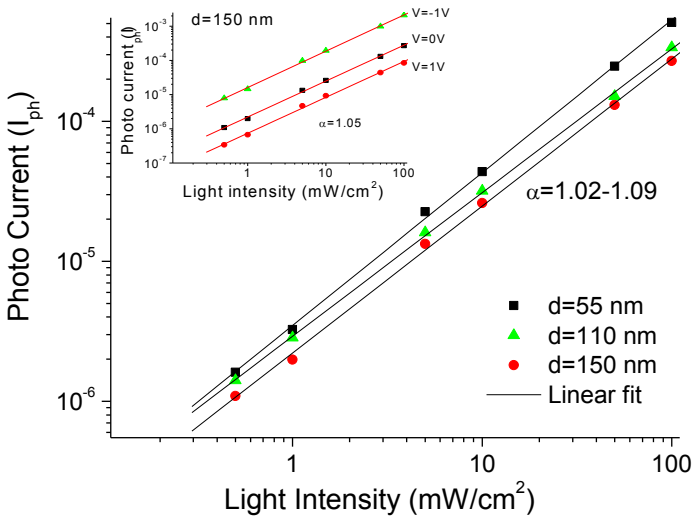


**Figure 33 The dependence of photocurrent on the incident light intensity for annealed M3EH-PPV:CN-Ether-PPV polymer blend devices with different thicknesses of the active layer: 55 nm (square), 110 nm (triangle) and 150 nm (filled circle). The photocurrents were measured with the applied bias voltage at 0V. The inset is the dependence of photocurrent on the incident light intensity for the device with thickness of 150 nm measured under the applied bias voltage at -1V, 0V, and 1V respectively.**

In 1971 Goodman and Rose predicted the existance of a upper limit for the photocurrent in semiconductors at high light intensities.[34] The occurrence of this upper limit originates from space charge accumulation at high charge carrier densities due to unbalanced charge transport. This upper limit is defined as the space charge limit (SCL). Since in the polymer blend device, the charge carrier mobilities are often strongly differed between the electron donor and acceptor, space charge effects are quite likely to occur. Mihailetchi et al. [122] demonstrated recently the existance of space charge effects in a blend of polymer with PCBM. Based on their experimental results, they pointed out that a space charge limited photocurrent follows a one-half power dependence on voltage.

We have plotted the dark-corrected photocurrent as a function of the internal field (given by $[V_0\text{-}V]/d$) for both the blend and the bi-layer devices in Figure 34. $V_0$ is defined as the compensation voltage, which is the external bias at which the photocurrent $I_{ph}$ is equal to zero.

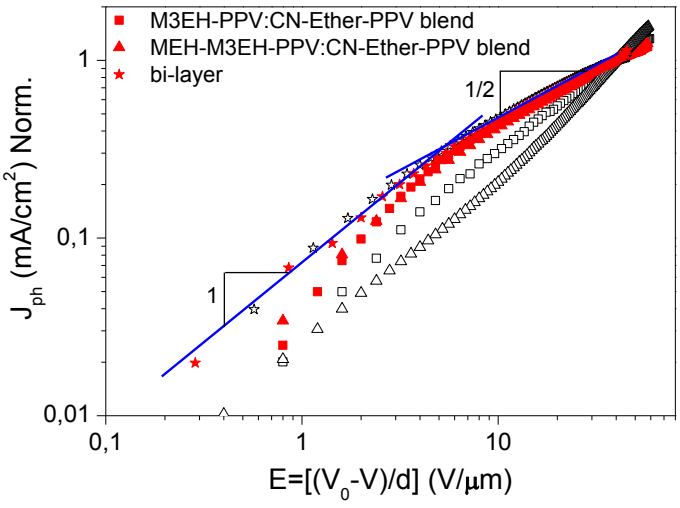


**Figure 34 Field dependence of dark corrected photocurrent on a log-log plot for the devices: M3EH-PPV:CN-Ether-PPV blend (squares), MEH-M3EH-PPV:CN-Ether-PPV blend (triangles), and a well defined bi-layer device with 10 nm M3EH-PPV interlayer and 50 nm CN-Ether-PPV (stars). The photocurrents are plotted both for the as prepared layers (open symbols) and for the samples annealed at 110°C (filled symbols).**

Discarding the properties of the as-prepared blend, which might be transport-limited, all curves followed the same field-dependence.

Interestingly, the photocurrents of all annealed devices scaled linearly with an internal field up to ca. 6 V/µm, followed by almost a one-half power dependence at higher fields as also reported by Mihailetchi et al. However it was also predicted by Goodman and Rose that the photocurrent should have a three-quarter power dependence on light intensity when space charge effects are significant. As shown in Figure 33, the photocurrents measured from all of our the M3EH-PPV:CN-Ether-PPV blends with different layer thicknesses was proportional to the light intensity. Thus, for practical device thicknesses (comparable to the penetration depth of light), space-charge effects are insignificant.

## 5.5 Conclusion

In this chapter, we first reviewed the previous work on the PL dynamics of the M3EH-PPV and CN-Ether-PPV homopolymers as well as of the 1:1 blend of both polymers. It is demonstrated by the combination of steady state and time-resolved PL measurements intra-chain exciton emission dominates in M3EH-PPV film while excimers play a major role in the emission of CN-Ether-PPV films. In the polymer blend, excitons are efficient separated as shown by the nearly complete PL quenching. However, time resolved spectroscopy measurements proofed the

occurrence of a new emitting species in the blend which is attributing to an exciplex. When the blend is annealed, inducing a higher degree of phase separation, a clear reduction of exciplex emission can be observed.

In section 5.4, the correlation between exciplex formation and solar cell performance was investigated by comparing two PPV-blend systems where the electron donor polymer shows different solubilities. The observed strict anticorrelation between exciplex emission and photocurrent generation indicated that the efficiency for generating free carriers is governed by local processes. Further studies on bilayer devices with a strict D-A interface gave strong evidence that the generation of free charge carriers rather than charge transport and bimolecular recombination is the main factor limiting the solar cell efficiency of these devices. We propose that the lower efficiency of these polymer-polymer blends compared to those of PCBM based blends is mainly caused by the lower dissociation efficiency of the geminate electron-hole pairs.

Many possible factors influencing the dissociation efficiency of the exciton can be identified: First of all, the columbic interaction between hole and electron is strongly affected by the dielectric constant. Second, the escape probability of the geminate pair from radiative recombination via an exciplex should be largely influenced by the mobility of the charge carriers. Typical exciplex fluorescence decay times were found for the M3EH-PPV:CN-Ether-PPV system to be in the 5 ns range.[9] Assuming that a distance between hole and electron of 2 nm is needed to escape the exciplex recombination, the drift velocity ($v_d$) should be larger than 0.2 m/s. The drift velocity is related with the mobility ($\mu$) by: $v_d = \mu \times E$. Thus, with a typical field strength of $E=10^7$ V/m mobilities larger than $\mu = 2 \times 10^{-8} \frac{m^2}{Vs} = 2 \times 10^{-4} \frac{cm^2}{Vs}$ are needed. Whereas hole mobilities in PPV derivatives are known to reach these mobility values, the electron mobility in CN-ether-PPV shall be few orders of magnitude lower, due to the amorphous structure of the bulk polymer and the high density of polar CN groups. In this case, the electrons will tend to localize at the hetero-interface, in contrast to rather crystalline materials like fullerenes or perylenes, where the periodic packaging lead high mobilities and even coherent transport. The major challenge for all-polymer solar cells is thus the development of crystalline electron-transporting semiconducting polymers with high mobilities.

# Chapter 6 Tuning of inter-chain interaction and solar cell performance

In the previous chapter we proposed that annealing leads to a higher degree of phase separation which in turn increases the probability for the dissociation of electron-hole pairs bound at the heterojunction into free carriers. Similar conclusions have been drawn recently by McNeill et al. and Mandoc et al. from studies on other polymer-polymer blend systems.[26, 68]

In bulk heterojunction solar cells, both photocurrent generation and charge transport are closely related to the film morphology. Hence, the nano-morphology is critical important to obtain high efficiencies. There are several approaches of controlling the blend morphology. A common approach for polymer blends is to control the morphology through processing conditions, e.g. solvent selection, solvent evaporation time, surface interaction and subsequent annealing. However, it is difficult to obtain a well controlled morphology. Additionally, block copolymers containing the electron donating and electron accepting segments in one chain have been used as a synthetic approach to obtain a nano-morphological interface. Unfortunately, the efficiency of devices made from blockcopolymers is still rather low.

In an effort to extend the understanding of the interrelation between structural, optical and optoelectronic properties in polymer-polymer photovoltaic devices, we have performed studies on M3EH-PPV:CN-ether-PPV blends coated from different solvents as well as from a solvent mixture. We compared M3EH-PPV:CN-Ether-PPV (1:1 by weight) blends prepared from 1,2,4-tri-chlorobenzene (TCB), chloroform (CF) and mixtures of TCB and CF with respect to the photoluminescence, morphology and solar cell performance.

## 6.1 Introduction

It is well established that the type of solvent used for spin coating, the spin rotation speed and the solution concentration have a significant influence on the polymer blend morphology. Solvents with different boiling points will result in different drying times during the film formation, thus affecting the morphology and the photovoltaic properties of the polymer blend device[123, 124] Furthermore, different solubilities of the two components in a common solvent affect the phase

separation during drying of the layer. For example, additives which selectively dissolve only one component were shown to improve the efficiency of solar cells made from a polymer-PCBM blend. [125, 126]

According to the previous studies, the efficiency of free carrier generation is strongly related to the exact nano-morphology of the sample and a certain degree of demixing is a necessary condition for achieving high efficiencies in polymer-based solar cells. To tune the degree of phase separation we have used chloroform and tri-chlorobenzene, instead of chlorobenzene, as solvents for the M3EH-PPV:CN-Ether-PPV blend. CF is a good solvent for both polymers, while TCB is a selective solvent for CN-ether-PPV, implying that M3EH-PPV will first solidify upon drying of the layer. A second reason why we selected TCB is its high boiling point (~230°C) owing to its low vapor pressure (0.29 mmHg at 25°C).[127] Film formation from TCB will, therefore, be rather slow which allows the polymer chains to reorganize themselves during evaporation of the solvent. Studies on polymer-based field transistors have shown superior performance for layers coated from this high boiling point solvent, which was attributed to a highly-ordered chain morphology.[128] For these two reasons a phase separated morphology is expected even in the as-prepared blend layers coated from TCB.

## 6.2 PL of polymer blend prepared from different solvents

In Figure 35 we show the steady state PL spectra for the as-prepared and annealed blend layers coated from pure CF and TCB. Also shown are the respective spectra for a layer cast from CB, which have been discussed in detail in the previous chapter.

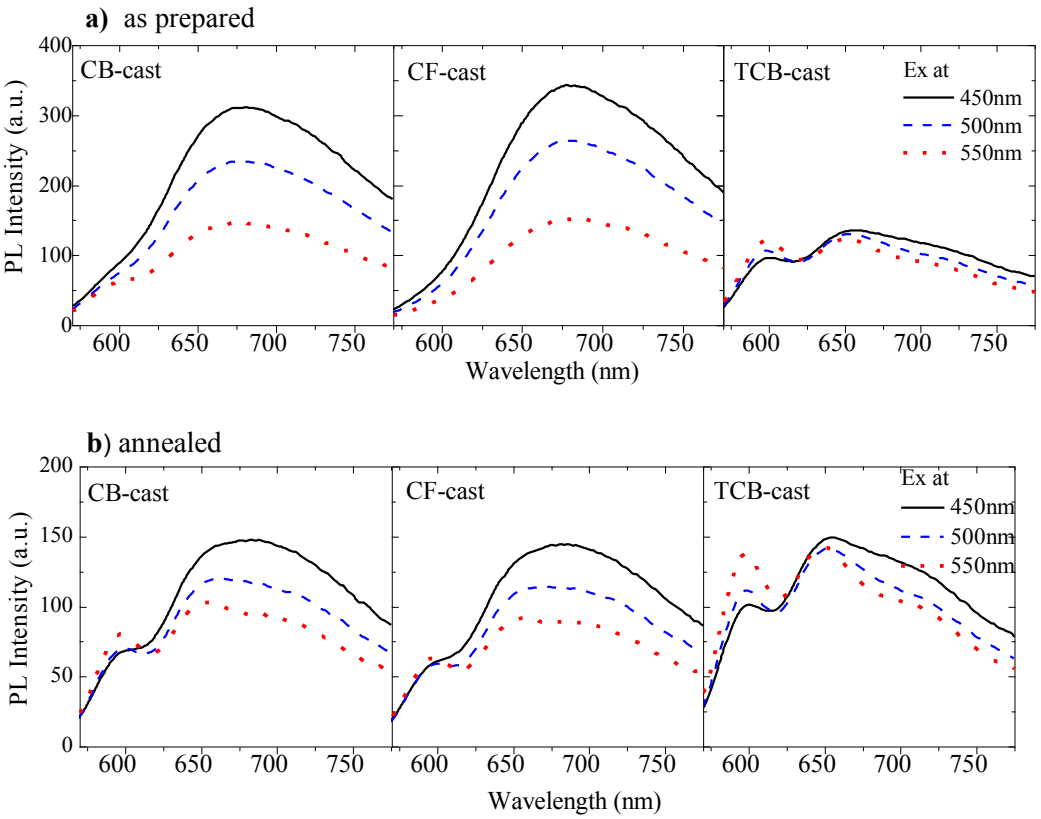


**Figure 35 The photoluminescence spectra for films of 1:1 M3EH-PPV:CN-Ether-PPV blends spin-coated from CB, CF and TCB respectively. All the samples were prepared on plain glass substrates and excited at 450, 500 and 550 nm. The spectra have been calibrated for the same excitation intensity. The thicknesses of all blend layers were ca. 80 nm.**

In contrast to blends coated from CB, the as-prepared CF-cast film features only the 670 nm exciplex peak, with no evidence for excitonic emission from either M3EH-PPV or CN-ether-PPV. When moving the excitation to shorter wavelength, the overall emission intensity increases due to additional absorption by the electron-acceptor, but the shape of the PL spectrum stays the same. Apparently, excitons formed on either CN-ether-PPV or M3EH-PPV rapidly decay to form exciplexes, indicating a high degree of intermixing in the as-prepared samples coated from CF. No evidence for excimer emission can be seen in the steady state PL spectra. Since both polymers are very soluble in CF, blends made therefrom are expected to become homogeneously intermixed on a molecular level.

For as-prepared samples coated from TCB, the singlet exciton and exciplex emission bands are of similar intensity (for excitation at 550 nm). The emission spectrum barely changes upon annealing. This gives strong evidence that the blend morphology is phase-separated and close to an equilibrium state right after

spin-coating. The exciplex component in the total emission spectra can be obtained by subtracting the pristine M3EH-PPV emission as shown in Figure 36.

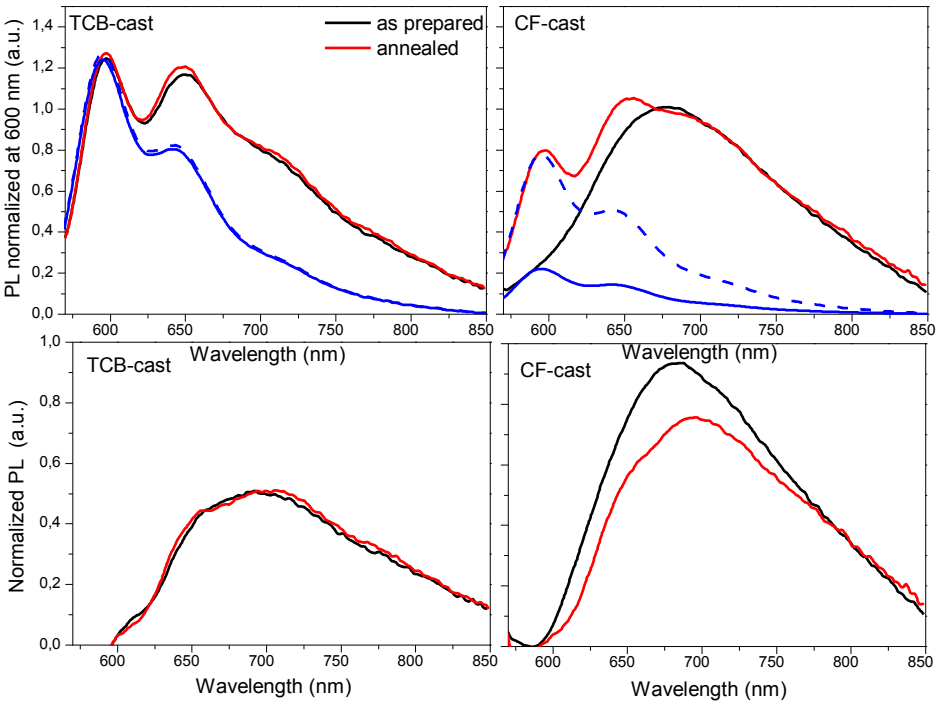


**Figure 36 Top: The normalized steady state PL of the polymer blends spin cast from TCB and CF. Bottom: The exciplex components obtained by subtracting the M3EH-PPV emission contribution (blue lines). The excitation was at 550 nm in all cases. For the polymer blend, black and red solid line represented the as prepared and annealed samples respectively. Before subtracting the M3EH-PPV emission, the PL was normalized at the emission wavelength of 670 nm for easier comparison.**

Since the samples were excited at 550 nm, where CN-Ether-PPV hardly absorbs, emission from it can be neglected. Clearly, the relative exciplex contribution in the as-prepared samples is doubled when the solvent change from TCB to CF. To summarize the results of photoluminescence, one can confirm that the donor-acceptor inter-chain interaction is largely tunable by using the different solvents.

The PL spectra of films spin coated from different ratios of TCB and CF are compared in Figure 37. With increasing CF fraction, the exciplex emission raises continuously, indicating that the morphology becomes more and more intermixed.

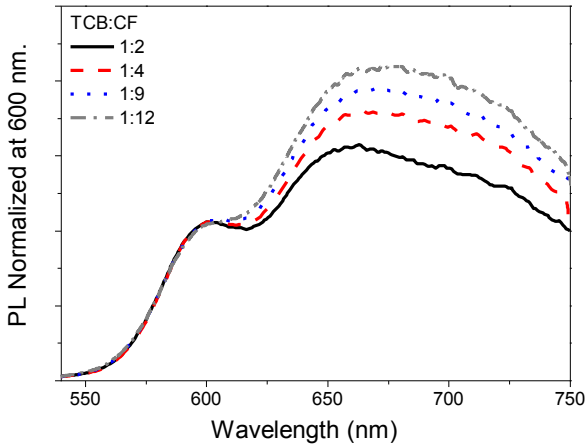


**Figure 37 Photoluminescence spectra (normalized at 600 nm) of as-prepared M3EH-PPV:CN-Ether-PPV (1:1 by weight) blend films spin-coated from TCB:CF solvent mixtures for different ratios. The samples were excited at 500 nm.**

Unfortunately, layers cast from pure TCB were rather inhomogeneous and not useful for device fabrication. Quite homogenous films could be obtained when the CF ratio in a TCB:CF mixed solvent was 80 % and above. For this composition, the relative emission intensity at 670 nm is still significantly lower than for the CB-coated layers.

We like to point out that the optical data presented here do not allow to differentiate whether exciton dissociation and exciplex formation occurs at the interface between a pure donor and a pure acceptor phase or within individual phases. Flory-Huggins theory predicts that phases formed by the demixing of two polymers are not pure but contain minority components. There is no doubt that such nanoscale intermixing occurs in blends of the two most studied polyfluorenes, PFB and F8BT.[129, 130] Kietzke et al. recently studied the optical properties of PFB:F8BT blends in nanoparticles. The results further revealed that exciton emission is mainly from the F8BT rich phase (with an PFB concentration of less than 5 wt.%) while exciplex formation occurs mainly in the PFB-rich phase (with a 10-15 % F8BT minority content).[131] On the other hand, recent work by McNeill and coworkers suggested that the domains in annealed PFB:F8BT blend layers have a high purity.[68] For the studied M3EH-PPV:CN-ether-PPV blend, we are not in possession of information on the purity of the phases.

## 6.3 Nanomorphology of polymer blend

### 6.3.1 Studies of excited state properties by means of time-resolved photoluminescence

All PL spectra except those measured on the as-prepared blend coated from CB exhibit a clear contribution from the M3EH-PPV exciton. This emission might arise either from the radiative decay of initially photoexcited excitons or from excitons "recycled" from exciplexes through thermal excitation. The latter process was first proposed by Morteani et al.[41] for polyfluorene blends and recent work supported the view that this process is also active in PPV-based blends.[112, 132] To improve the understanding of the excited state properties in relation to the blend morphology, photoluminescence decay measurements were performed on the as-prepared and the annealed samples.

Transient decays measured at different emission wavelengths on an as prepared TCB:CF-cast layer are shown in Figure 38. The curves have been normalized to the same PL intensity transient time of 4 ns. The overall emission decay curve showed strong similarity for the transients measured at 550 nm and 600 nm. Large differences can be seen when the emission wavelength is 700 nm. Hence discuss only transients of layers cast from CF and the TCB:CF solvent mixture for the emission decays at 600 nm and 700 nm (as shown in Figure 39).

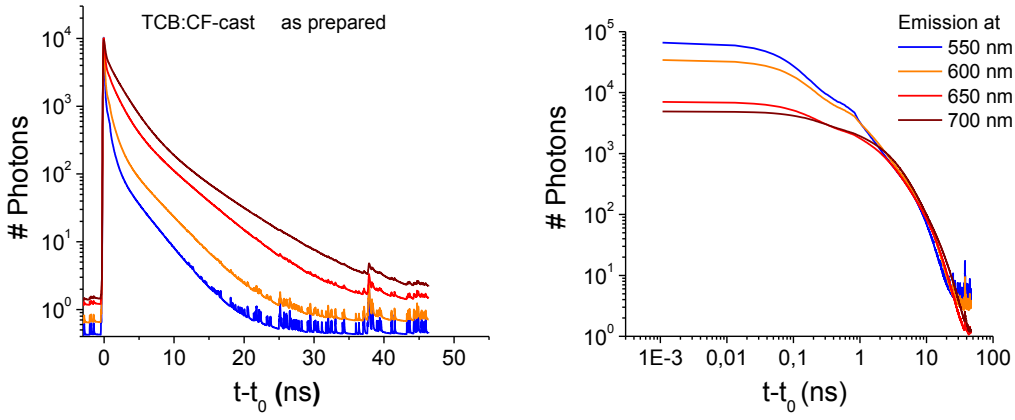


**Figure 38 Time-resolved photoluminescence transients with semi-log (left) and double-log (right) representation for polymer blend film prepared from TCB:CF. The emission were collected at 550, 600 , 650 and 700 nm, respectively. All the samples were excited at 405 nm.**

The corresponding semi-log decay curves are included as inset in every diagram.

For a detection wavelength of 700 nm, contributions from intrachain excitons on either component must be very weak and the emission shall be dominated by the exciplex (with a possible weak emission contribution from the excimer on CN-ether-PPV).

The decay curves are almost bi-exponential, but the fit is further improved by including a small decay component with very short decay time. Noticeably, the decay of the as-prepared blend coated from CF is nearly mono-exponential, with a decay time of 3.3 ns.

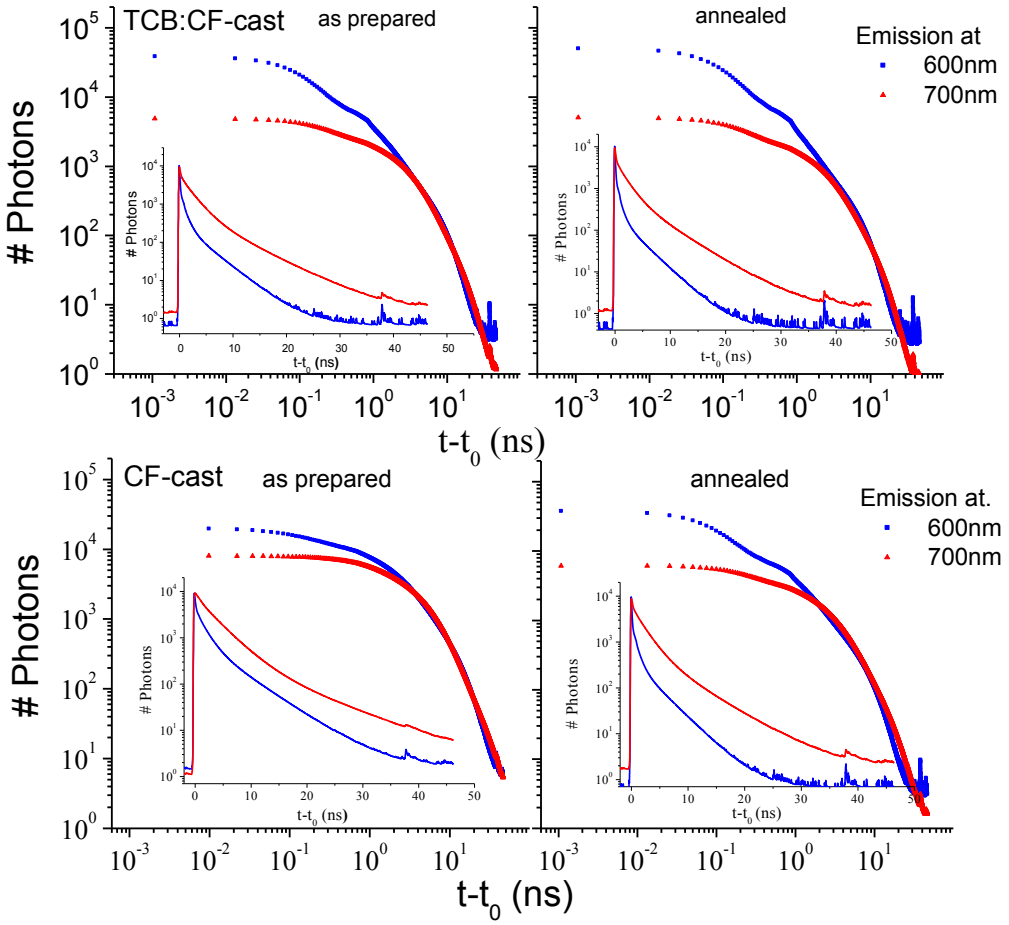


**Figure 39 Time-resolved photoluminescence transients (double-log representation) for polymer blend films prepared from a 1:4 TCB:CF mixture or from pure CF. Samples were excited at 405 nm and the emission were detected at 600 nm or 700 nm. The insets show the decays on a semi-log scale.**

**Table 8 PL decay times of polymer blends deposited from different solvents. The values are obtained by the best fit to the PL transients taking into account the instrumental response function. The average life times, calculated as the arithmetic means of the decay times weighted with the respective yields, are listed in the last column.**

| Sample | Emission at | Annealing | $\tau_1$ (ns) | $\tau_2$ (ns) | $\tau_3$ (ns) | Ave. $\tau$(ns) |
|---|---|---|---|---|---|---|
| TCB/CF-cast | 600nm | N | 0.07 (48%) | 0.88 (28%) | 3.9 (24%) | **1.2** |
| | | Y | 0.06 (60%) | 0.75 (21%) | 3.4 (20%) | **0.9** |
| | 700nm | N | 0.16 (12%) | 2.0 (59%) | 6.1 (29%) | **3** |
| | | Y | 0.13 (16%) | 1.7 (51%) | 5.2 (33%) | **2.6** |
| CF-cast | 600nm | N | 0.13 (17%) | 1.55 (44%) | 5.3 (39%) | **2.8** |
| | | Y | 0.06 (42%) | 0.81 (29%) | 3.6 (29%) | **1.3** |
| | 700nm | N | 0.6 (8%) | 3.3 (76%) | 9.5 (16%) | **4.1** |
| | | Y | 0.17 (11%) | 2.0 (61%) | 5.8 (28%) | **2.9** |

All the data shown here suggest that the as-prepared blend from CF is a rather homogenous mix of the two components. Therefore, the 3.3 ns component is attributed to the decay of an exciplex localized on adjacent polymer chains in a rather homogenous environment. Note that Chasteen et al. have originally assigned the 3.5 ns decay to the intrachain exciton on CN-ether-PPV.[112] Because of the very low PL intensity below 550 nm (at which the CN-ether-PPV exciton emits) we can safely exclude this assignment. For all other samples, the PL decays at 700 nm consist of a shorter component of 1.7-2 ns (51-61%) and a longer decay with 5.2-6.1 ns (28-33%). The presence of two decay components in all blends with significant phase separation can be attributed to the larger inhomogeneity of the layers and might even indicate that exciplex emission stems from two distinct phases (either rich in M3EH-PPV or in CN-ether-PPV).

At 600 nm, the emission from the exciplex is negligible weak. The decays are clearly tri-exponential. Except for the as prepared CF-cast film they show essentially the same dynamic features: a very fast decay (60-70 ps, 42-60%), an intermediate component (0.75-0.88 ns, 21-29 %) and a slow decay (3.4-3.9 ns, 20-29 %). Following the interpretation by Chasteen et al. the fast component is assigned to the intrachain exciton formed in the M3EH-PPV rich phase, which is rapidly quenched by dissociation in the blend. The rather high yield of the initial fast component indicates that the excitonic contribution seen in the steady-state PL spectra stems mainly from initially-generated excitons. It further implies that the length scale of phase separation in these samples is sufficiently large to allow

a considerable fraction of excitons formed on the donor to decay radiatively (before reaching the D-A heterojunction). The short decay component is almost absent in the as-prepared blend coated from CF, meaning that excitons formed initially on M3EH-PPV are almost immediately quenched, implying that the exciton diffusion length is very short in these blends. A conclusive assignment of the longer emission decays at 600 nm is rather difficult, but it is not unlikely that these components are due to excitons regenerated from thermally excited exciplexes.

### 6.3.2 Electric field induced photoluminescence quenching in polymer blend

As shown in Figure 36, the exciplex contribution to the overall blend emission can be deconvoluted. We found that after annealing, the exciplex contribution decreased by a factor slightly larger than two. In electric field-induced PL quenching experiments, the emissive decay of selected inter-chain excitations can be tuned by applying an external counter-field during photo-excitation of the samples. The attractive columbic interaction defining the binding energy of a hole-electron pair can be intentionally weakened in this way. In an exciplex, the hole and the electron are localized on neighboring macromolecules of different chemical nature. The binding energy in such a charge transfer state should, therefore be lower than for a monomolecular excited state, such as an exciton, where the hole-electron distance is smaller.[133] For this reason, exciplex-emission will be more strongly affected by an external field, and the recombination of such a loosely bound hole-electron pair will be more easily hindered by a reverse voltage applied to the device.[41]

Figure 40a shows the photoluminescence spectra measured under different external bias for a blend deposited from a TCB:CF solution. At zero voltage, the PL spectrum exhibited a pronounced excitonic emission shoulder at 600 nm. The intensity ratio of the main peak at 670 nm to the 600 nm shoulder is about 2:1 at zero electric field, which is reduced to about 1.4:1 when the voltage is increased up to 35 V. Similarly, in the sample fabricated from a pure CB solution the PL emission could be quenched selectively by means of the voltage applied (see Figure 40b). In this case, the 670 nm to 600 nm peak ratio is even inverted from 4 at zero bias down to 1.8 at 35 V. As a reference, we give the corresponding PL quenching plot of a pure M3EH-PPV film (150 nm) spin-coated from CB (Figure

40c). Here the 670 nm to 600 nm peak ratio is independent on the quenching voltage applied, indicating pure excitonic emission.

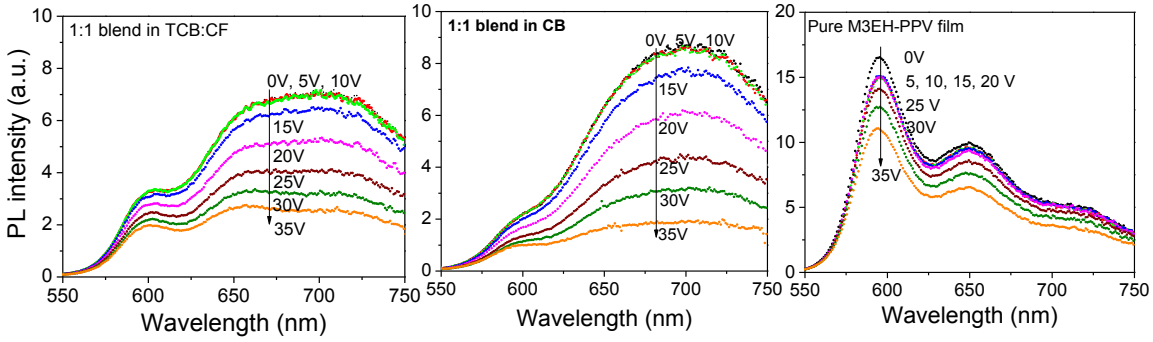


**Figure 40 Electric field induced photoluminescence quenching of a) TCB:CF (thickness of active layer 95 nm) b) M3EH-PPV:CN-Ether-PPV blend solid film prepared from chlorobenzene (thickness of active layer 110 nm) and of c) pure M3EH-PPV solid film (150 nm). The external voltage is applied by using a Keithley 2400 source-meter instrument. The applied potential was negative on the ITO-electrode. All the active layers are as-prepared and Ag was used as the top electrode.**

This is also summarized in Table 9, where the peak ratios are given and compared among the three samples for zero and 35 volts bias.

**Table 9 List of 670 nm to 600 nm photoluminescence peak ratio for polymer blend film prepared from TCB/CF mixed solvent and from chlorobenzene respectively. For comparison, the ratio is also listed for the pure M3EH-PPV film.**

| | 0V | 5V | 20V | 30V | 35V |
|---|---|---|---|---|---|
| **Blend from TCB/CF** | 2.0 | 2.0 | 1.6 | 1.5 | 1.4 |
| **Blend from CB** | 4.0 | 4.0 | 4.0 | 2.5 | 1.8 |
| **Pure M3EH-PPV from CB** | 0.6 | 0.6 | 0.6 | 0.6 | 0.6 |

### 6.3.3 Atomic force microscopy

Figure 41 depicts the Atomic Force Microscopy (AFM) topography images of 1:1 M3EH-PPV:CN-Ether-PPV films spin-coated from a 1:4 mixture of TCB and CF or from chloroform. For films cast from TCB:CF, the surface is relatively rough on a sub-micrometer scale, with the root mean square (rms) roughness of ca. 2.7 nm. In contrast, as prepared films cast from CF have a very smooth surface, with a rms roughness of below 1 nm.

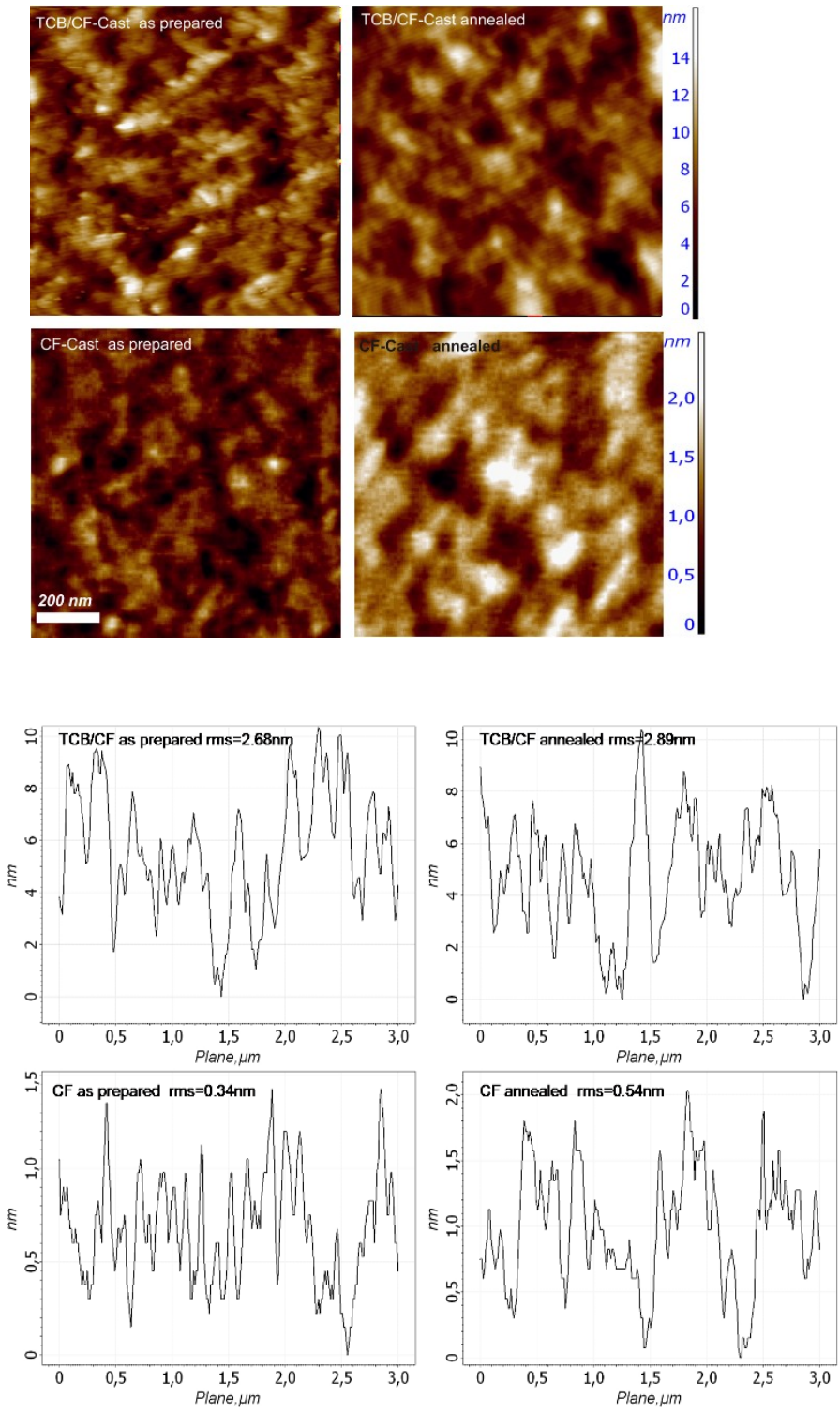


**Figure 41 Tapping mode AFM topography images of 1:1 M3EH-PPV:CN-Ether-PPV blends spin-coated from TCB:CF (1:4) or from pure CF. Typical height profiles obtained from these images are shown on the right side.**

These observations are consistent with the picture extracted from the optical studies. Apparently, as-prepared layers casted from chloroform exhibit a homogeneous blend morphology, while layers coated from the solvent mixtures possess nano-sized domains. A similar behavior was also observed by Li et al. in

their studies on the self-organization of polythiophene/fullerene blend system where they pointed out that the rough surface of slow-grow film is a signature of polymer self-organization to ordered structures in the film.[87]

## 6.4 Photovoltaic properties

### 6.4.1 PV performances of polymer blend solar cells prepared from different solvents

The photovoltaic characteristics of solar cells prepared from CF or the TCB/CF mixture are shown in Figure 42 and the relevant parameters are listed in Table 10. The performance of the as-prepared device made from CF is rather poor, with a maximum ICPE of only 4.5 %, a fill factor of 24 % and an ECE of only 0.15 %. In contrast, devices coated from the solvent mixture perform quite well even in the non-annealed state. Upon annealing, the ICPE of the CF-cast device improves by a factor of four while it changes only little for samples deposited from the mixed solvent. As shown before for blends coated from CB, there is a strict anti-correlation between the exciplex emission contribution in the steady-state PL and the photovoltaic performance.[27]

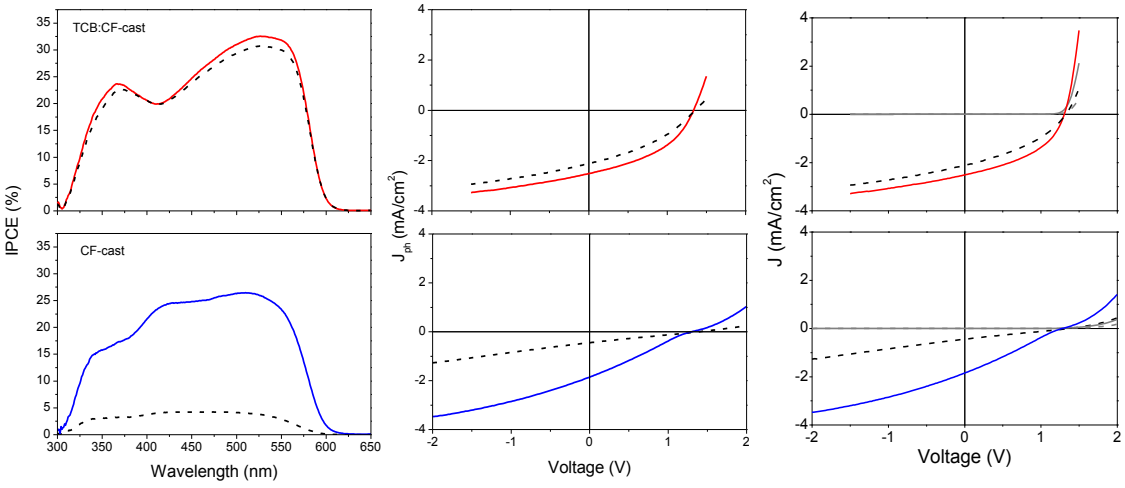


**Figure 42 Photovoltaic properties of M3EH-PPV:CN-Ether-PPV (1:1) blend devices. The active layers were spin-coated either from TCB:CF(1:4) or from CF. From left to right is the external quantum efficiency vs wavelength, the photo-current-density vs voltage, and the current density vs voltage under illumination or in dark. The solid lines represent the annealed devices and the black dashed lines show the as-prepared devices. Dark current densities are plotted as black dash-dotted lines.**

This suggests that the photovoltaic properties are essentially determined by processes on the local scale, namely the dissociation and recombination of polaron pairs formed at the donor-acceptor heterojunction.

**Table 10 Photovoltaic parameters of the samples shown in Figure 42.**

| Sample | Annealing | IPCE | $V_{oc}$ (V) | $J_{sc}$ (mA/cm2) | FF | ECE |
|---|---|---|---|---|---|---|
| **TCB/CF-Cast** | N | 31% | 1.33 | 2.1 | 37% | 1.0% |
| | Y | 33% | 1.31 | 2.5 | 44% | 1.42% |
| **CF-Cast** | N | 4.5% | 1.38 | 0.45 | 24% | 0.15% |
| | Y | 24% | 1.29 | 1.85 | 26% | 0.62% |

There is a remarkable effect of the preparation conditions on the fill factor. The annealed blend prepared from TCB/CF exhibits a FF of 44% which is among the highest values reported for polymer-polymer blends. In contrast, the fill factor of the as-prepared layer coated from CF is only 24 %, implying a large dependence of the photocurrent on the internal electric field. As pointed out above, low fill factors have been attributed to the dependence of free charge carriers generation on the internal electric field, bimolecular recombination of charges before they are extracted at the electrodes or to the formation of space charge due to unbalanced transport.[132] A direct way to distinguish between these processes is to investigate the dependence of photocurrent on the incident light intensity. A well accepted conclusion is that for non space-charge-limit devices and negligible bimolecular recombination, the photocurrent should closely follows a linear dependence on light intensity.[134]

### 6.4.2 Intensity and Field-dependence of Photocurrent

Shown in the left graph of Figure 43 are current voltage characteristics of a CF-cast as-prepared device recorded under different illumination conditions. Apparently, the shape of photocurrent curve does not vary with light intensity, implying that it is not affected by the amount of charges present in the device. Moreover, the photocurrent increases strictly linearly with the incident light intensity, irrespective of the applied voltage (right graph in Figure 43). Combining these two observations, the low fill factor measured in the CF-coated as-prepared blends must be attributed to inefficient field-assisted dissociation of the interfacial polaron pair.

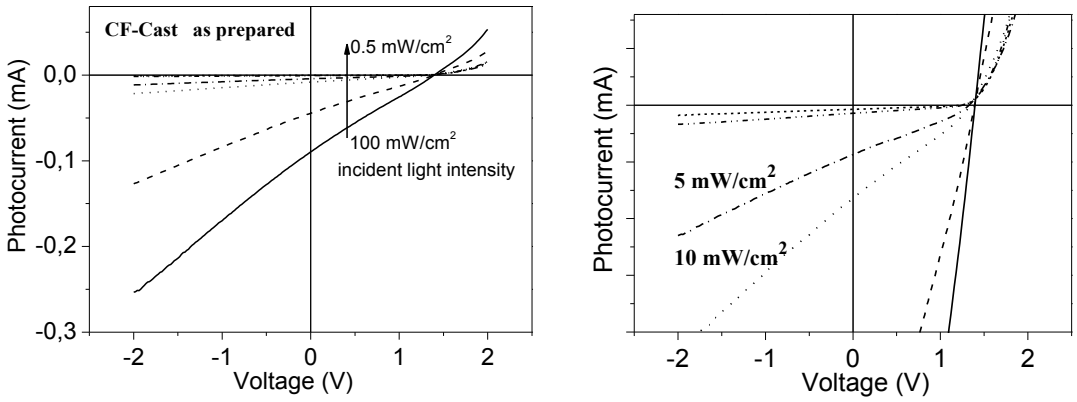


**Figure 43 Left: Current-Voltage characteristic of an as-prepared CF-cast sample (85nm) measured under white light of different intensity. Right: a closer view for low light intensity.**

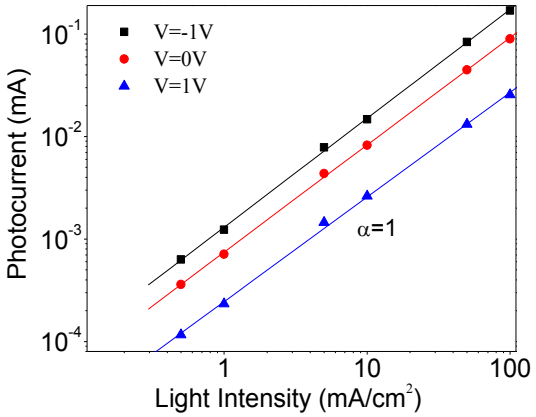


**Figure 44 Dependence of the photocurrent on the incident light intensity for the same sample showed in Figure 43 with the external bias set at -1V, 0V and 1V. The solid lines are linear fits with a slope of 1.0.**

As shown in Figure 44, also all other devices showed the same strict linear dependence of the photocurrents on light intensity, irrespective of the active layer thickness. No difference in the intensity dependence of photocurrent between annealed and as-prepared samples was observed. These findings rules out space charge formation and bimolecular recombination and implies that the photovoltaic performance is determined by the field-dependence of charge carrier generation. These conclusions are in full agreement with the results of studies on the same polymer blend system deposited from chlorobenzene showed in the previous chapter.

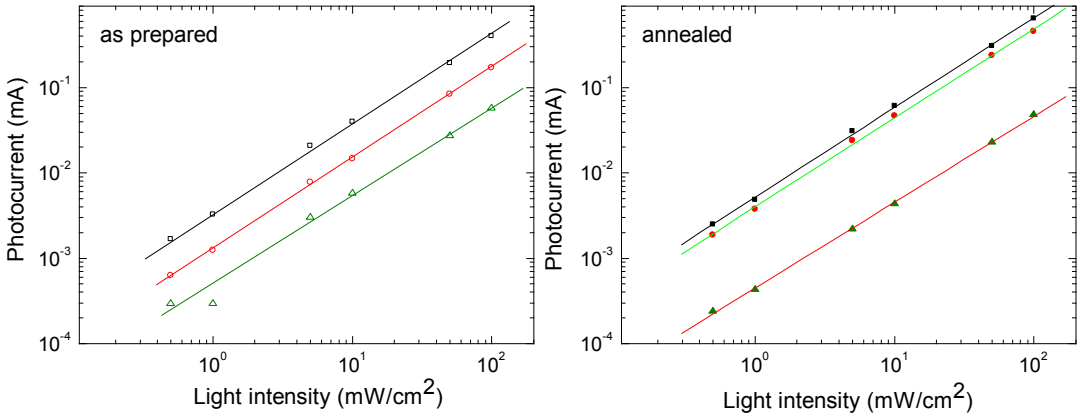


**Figure 45 Dependence of the photocurrent on incident light intensity (measured at a bias of -1V) for M3EH-PPV:CN-Ether-PPV blends prepared from TCB:CF (1:4) with an active layer thickness of 90 nm (square) or 145 nm (triangle). Also shown are data for a 85 nm thick blend coated from CF (circles).**

In Figure 46, the dark-corrected photocurrents are plotted as a function of the internal electric field.

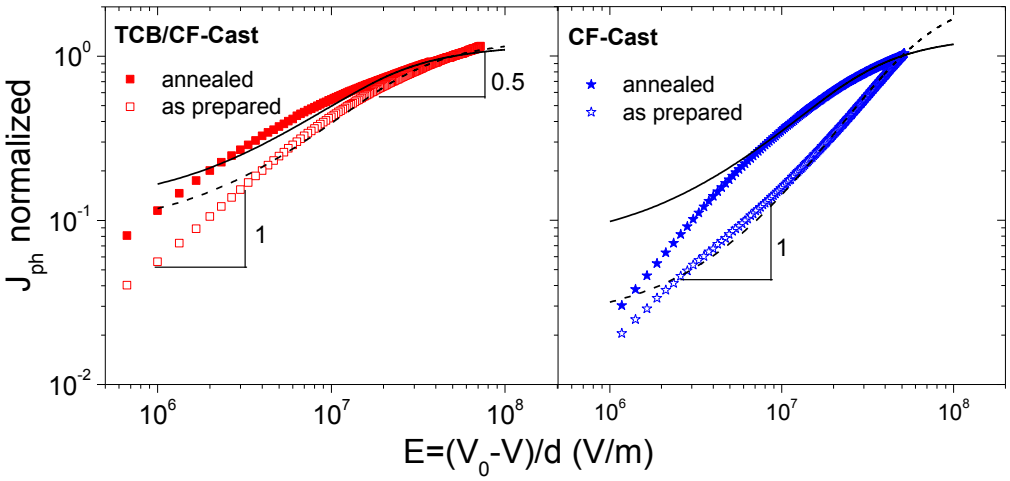


**Figure 46 Field dependence of the dark-corrected photocurrent (plotted on a log-log scale) for M3EH-PPV:CN-Ether-PPV blends prepared from a 1:4 mixture of TCB:CF (squares) and from pure CF (stars). The photocurrents are normalized to the value at a field of $5\times10^7$V/m. Open and full symbols show data for as-prepared and annealed samples, respectively. Dashed and solid lines display the corresponding fits with Onsager's theory as described in detail in the text.[1]**

The photocurrent of all devices follow a nearly linear dependence up to an electric field of ca. $5\times10^6$ V/m (corresponding to an external bias of ca. 1 V for an active layer thickness of 60 nm), which can be explained by the competition between

[1] The fitting was done by Marcel Schubert.

[2] This part of work was performed in close collaboration with Sebastian Bange.

drift and diffusion.[81] At higher fields, the as-prepared CF-cast film exhibits the steepest rise (with no clear tendency to saturate), implying that the formed electron-hole pairs are strongly bound.

### 6.4.3 Charge carrier generation fitted with Onsager model

As discussed in the introduction part, charge carrier generation in low mobility solids has been mostly described by either Onsager's model[32] or by the more recent model developed by Braun[40]. Both models rely on the field-induced separation of Coulombically bound electron-hole pair with initial distance $r_o$. Though Braun's model appears to be more applicable for disordered organic semiconductors, we were not able to fit the photocurrent data by assuming a delta-distribution of the initial pair distances $r_o$. Instead, reasonable fits were obtained over the whole field range when using Onsager's model with a fixed pair distance. These fits were shown in Figure 46 as solid and dashed lines. A good agreement to the data at high fields was obtained with an initial separation distances $r_0$ of 6 nm for the TCB:CF-cast as-prepared sample and $r_0$ = 7.1 nm for the annealed layer. For the CF-coated blend, $r_0$ = 3.5 nm for the as-prepared blend and $r_0$ = 5.6 nm for the annealed sample.

We are well aware of the fact that the value of $r_0$ retrieved from Onsager's model is not equal the true initial electron-hole pair radius but it is, nevertheless, a reasonable measure for the spatial extent of the coulombically bound polaron pair. It is, therefore, interesting to compare values of $r_0$ determined for our blends with those reported for conjugated polymers in the literature.

For fully conjugated PPV polymers, $r_0$ in the range of 1.9 to 2.5 nm have been reported.[36, 37] Inserting an ether linkage into the conjugated PPV backbone significantly reduced $r_0$ down to 1.1-1.6 nm.[36] It indicates that the polaron pair radius of fully conjugated polymers accounts in part for the delocalization of the hole along the polymer backbone. When adding a small amount of $C_{60}$ fullerene to PA-PPV, $r_0$ increased only slightly (though the photo-generation efficiency increased substantially). This is well understandable having in mind that the electrons remain localized on the isolated electron acceptors. Lloyd-Huges and coworkers have successfully applied Onsager's model to fit the field-dependent efficiency of photoinduced charge generation in an organic field effect transistor made from the conjugated polymer poly[(9,9-dioctylfluorene-2,7-diyl)-co-

(bithiophene)] (F8T2).[38] Their analysis yielded a polaron pair radius of ca. 2.2 nm, similar to values given above for fully conjugated PPV. The analysis of photoluminescence quenching in an as-prepared chloroform-coated blend of PFB with F8BT yielded $r_0$ = 3.1 at room temperature,[41] which is quite comparable to an electron-hole radius of 3.5 nm determined for our highly intermixed M3EH-PPV:CN-ether-PPV blend prepared under comparable conditions. These values seem to be indicative for a weak delocalization of electrons and holes in an interpenetrating network of donor and acceptor chains. The much higher initial pair radii for our annealed blends, therefore, suggests that carrier generation occurs at the boundary between two rather pure phases of well-organized chains, allowing for the rapid dissociation of the photo-generated polaron pairs. Further evidence for improved chain packing in the annealed blends comes from the absorption spectra of the blend layers as shown in Figure 47. These spectra show a well-resolved shoulder at the long wavelength side of the blend absorption, which becomes more pronounced and red-shifted upon annealing.

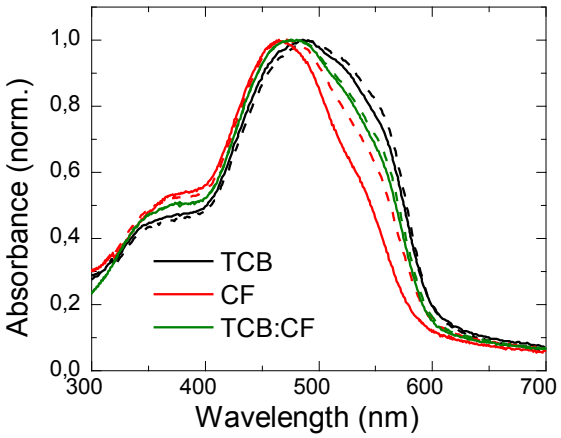


**Figure 47 Normalized absorption spectra of 1:1 polymer blends coated from TCB, CF or a 1:4 TCB:CF solvent mix. Solid and dashed lines are for as-prepared and annealed samples, respectively.**

## 6.5 Mobility and Bimolecular Recombination studied by the photo-CELIV technique[2]

Investigations on charge transport and recombination were performed for several reasons. Firstly, recent Monte Carlo simulations based on Onsager's theory suggested a correlation between the carrier mobility and the efficiency for the dissociation of the interfacial polaron pairs.[135] Secondly, Mandoc and coworkers

[2] This part of work was performed in close collaboration with Sebastian Bange.

pointed out that the field-dependent rate of carrier dissociation should be linear in the bimolecular recombination coefficient $\gamma$, which itself is a linear function of the average mobility of the electrons and holes.[132] Finally, the good fit of Onsager's model to our field-dependent photocurrent data suggests that dissociation involves the diffusion of both carrier under the influence of their mutual Coulombic potential and the internal electric field. Under these conditions, the bimolecular recombination of carriers should be Langevin-type, with the recombination coefficient given by:

$$\gamma_L = \frac{e(\mu_e + \mu_h)}{\varepsilon_0 \varepsilon_r}$$

There, $\mu_e$ and $\mu_h$ are the mobility of the electron and hole, respectively. We used the method of "carrier extraction by linearly increasing voltage technique" (photo-CELIV) [54-56] to investigate the transport as well as the rate of bimolecular recombination of charge carriers in the very same polymer blends as used in the solar cell devices. Details about this method will be described in appendix.

Figure 48 shows typical photo-CELIV current transients for varying values of $t_d$. For all sample types, a reduction of $j_{max}$ and an increase of $t_{max}$ upon increasing $t_d$ was found, corresponding to a drop in mobility.

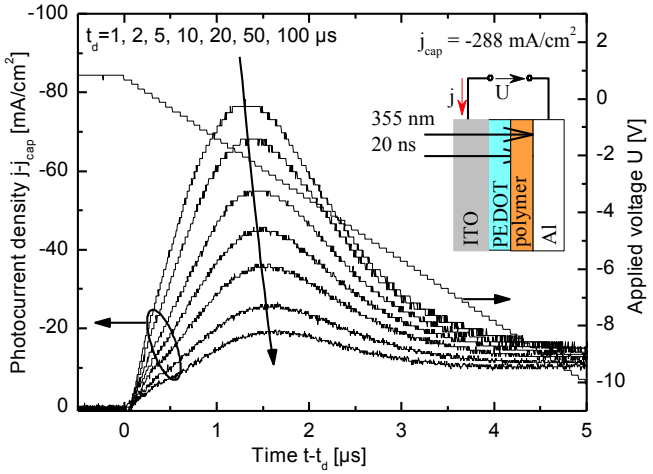


**Figure 48 Typical photocurrent transients obtained for films spin coated from CB solution with a thickness of *d*=53 nm and an active area of 1 mm$^2$ at *dE/dt*=4.06x10$^{13}$ Vm$^{-1}$s$^{-1}$. The delay time $t_d$ between photo excitation and carrier extraction is varied from 1 µs to 100 µs. The inset schematically shows the sample layer structure, the electrical circuit and the illumination direction. The top-down arrow attributes the corresponding $t_d$-parameter to each curve oriented forwards increased delay times.**

In addition, the extracted charge density decreases largely with increasing waiting time $t_d$. During this time period, the internal field is nearly zero and the photo-

generated charge density decays exclusively via bimolecular recombination. The zero-field bimolecular recombination coefficient $\gamma$ can be obtained from the slope of inversed charge density vs extraction time.

The obtained mobilities and extracted charge densities for TCB:CF and CF cast samples are shown in Figure 49. All samples show a strong decrease of the mobility during the first 10 µs after photoexcitation. Mobility relaxation by around 40 % within the first 10 µs after photogeneration of carriers has previously been reported by Mozer et al.[56] for MDMO-PPV/PCBM blend solar cells using the same method. They attributed this to an energetic relaxation of charge carriers.

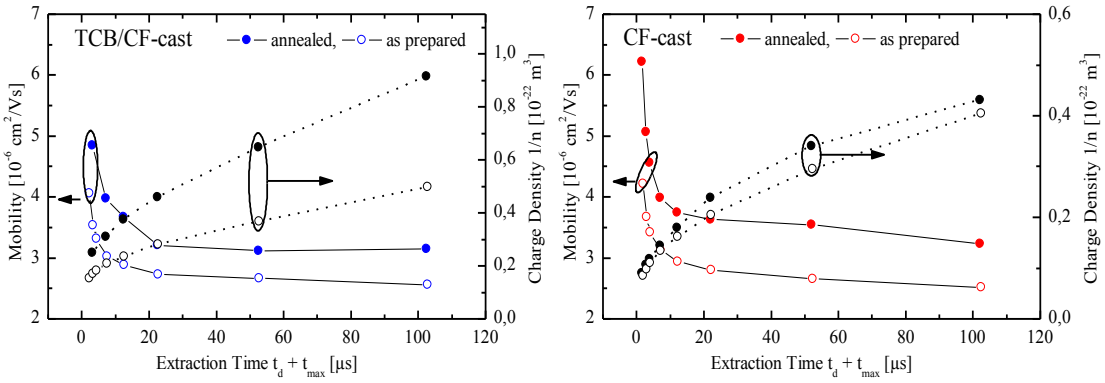


**Figure 49 Charge mobility values from CELIV experiments as a function of the delay time $t_d$ between excitation and charge extraction. The increase of the charge density as a function of $t_d$ is also given.**

Mobilities and bimolecular recombination coefficients determined from the regimes immediately following or at longer times after photoexcitation are summarized in Table 11.. It should be pointed out that CELIV measurements do not differentiate between the types of charge carriers. Hence, the results cannot be ascribed directly to either the motion of holes or electrons. Note that the mobilities deduced from our experiments are approx. one order of magnitude higher than the zero-field mobility measured for a related electron-accepting polymer by Mandoc and coworkers.[136] This suggests that the extraction signal seen in our CELIV experiment is due to holes and that these are the faster carriers.

**Table 11 Charge mobilities and bimolecular recombination coefficients of M3EH-PPV:CN-Ether-PPV blend layers with different preparation conditions.**

| Sample | Annealing | Thickness | μ (short)[1] | μ (long)[1] | γ (short )[2] | γ (long)[2] | $\mu_{eff}$ (short)[3] | $\mu_{eff}$ (long)[3] |
|---|---|---|---|---|---|---|---|---|
| | | | derived from transient peak | | | | derived from charge recombination | |
| | | nm | cm²/Vs | cm²/Vs | m³/s | m³/s | cm²/Vs | cm²/Vs |
| M3EH-PPV:CN-ether-PPV blends | | | | | | | | |
| CF | N | 55 | 4.2e-6 | 2.5e-6 | 9.2e-19 | 2.7e-19 | 1.5e-6 | 4.4e-7 |
| CF | Y | 55 | 6.2e-6 | 3.2e-6 | 9.9e-19 | 2.4e-19 | 1.7e-6 | 3.9e-7 |
| TCB:CF | N | 65 | 4.1e-6 | 2.6e-6 | 1.0e-18 | 2.9e-19 | 1.7e-6 | 4.7e-7 |
| TCB:CF | Y | 65 | 4.8e-6 | 3.1e-6 | 1.2e-18 | 5.9e-19 | 2.1e-6 | 9.7e-7 |

[1] **Mobility of charge carriers obtained from the transient peak during applied electric field at short time scale (1-10μs) and at long time scale (10-100μs).**

[2] **γ is zero-field bimolecular recombination coefficient, which is obtained from the slope of inversed charge density vs extraction time. Since the curve is not a straight line, the γ we used here is derived from the short time and long time scale respectively.**

[3] **$\mu_{eff}$: effective mobility defined as $\mu_{eff}=\varepsilon_0\varepsilon_r\gamma/e$.**

The conclusion can be drawn that films prepared from different solvents show similar mobilities and no significant improvement is observed upon annealing. Moreover, the bimolecular recombination coefficient (and the value of the effective mobility $\mu_{eff}$ as derived from this) is the same for all blends within the range of batch-to-batch variations (not shown). The effective mobility as deduced from the bimolecular recombination assuming Langevin-type recombination is a factor of 2-4 lower than the (hole) mobility determined from the maximum in the extraction transients. Note that the bimolecular recombination is measured at zero internal fields while the maximum of the extraction current appears at a field of ca. $4\times10^7$ V/m. Taking into account that the charge mobility generally increases with field one can conclude that bimolecular recombination is nearly Langevin-type. Non-Langevin recombination has been rarely observed, e.g. in highly-phase separated blends of poly(3-hexylthiophene) and soluble fullerene.[45] Our measurements show that the process underlying charge carrier recombination and separation in our samples is diffusion controlled in all cases, despite different degrees of phase separation and significant differences in the photovoltaic properties.

## 6.6 Conclusion

We reported a detailed study on how the charge carrier generation and the radiative recombination of intra- versus inter-chain excitations can be tuned in M3EH-PPV:CN-Ether-PPV (1:1 by weight) blends. By using pure solvents as well as the respective solvent mixtures for film deposition, a great variety of blend morphologies was achieved. Information on the blend morphology came from steady-state and time-resolved fluorescence studies. As-prepared layers coated from chloroform exhibited only emission from the exciplexes formed at the donor-acceptor heterojunction, with no evidence for the radiative decay of either the M3EH-PPV or the CN-ether-PPV exciton. Evidently these intrachain excited species dissociate rapidly by intermolecular charge transfer, pointing to a highly intermixed blend morphology. By using a poor solvent TCB for M3EH-PPV, which is concomitantly a good one for CN-Ether-PPV, phase-separation at an early stage of film deposition was induced. The appearance of emission from the M3EH-PPV exciton suggests that this morphology contains nano-sized domains composed almost entirely of the donor polymer. However, we found no emission from either the CN-ether-PPV exciton or the excimer in any of our blend layers. Hence we lack information on whether or not phase separation leads to pure acceptor phases. Nevertheless the rather high polaron pair radius as deduced from the Onsager fit suggests that both kinds of carriers are well delocalized on their respective phases in the phase-separated blends. Our view of the correlation between the morphology and excited state properties is summarized in Figure 50.
The nano-morphology is shown to have a large influence on the external quantum efficiency and particularly on the shape of the photocurrent characteristics. While as-prepared layers coated from CF exhibited fill factors of less than 25%, a fill factor of 44% was measured for annealed blends coated from the TCB:CF blend. The strict linear relation of photocurrent and incident light intensity rules out space charge effects and bimolecular recombination as the main factors determining the device properties. Photo-CELIV measurements confirmed that the variation in the performance of devices prepared under different condition can neither be related to differences in the bulk mobilities nor to significant changes of the (zero-field) bimolecular recombination coefficient.

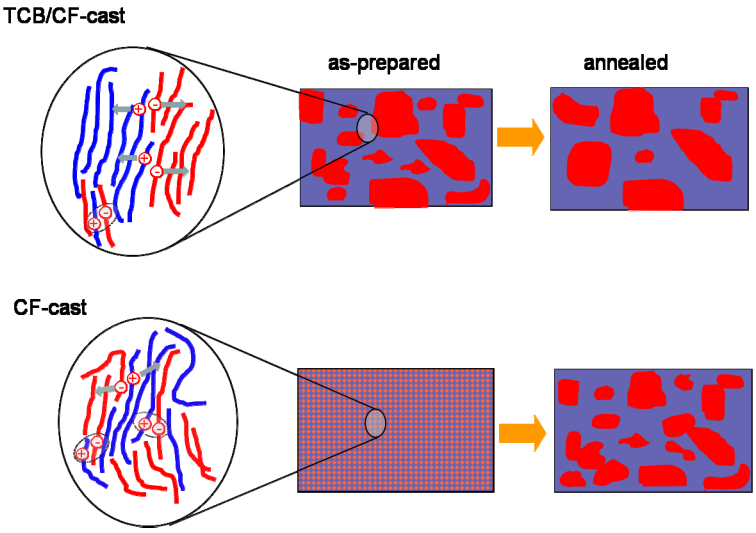


**Figure 50 Proposed nano-morphology for TCB:CF-cast and CF-cast films, before and after annealing. The close view is a simplified picture of charge carrier generation and exciplex formation in relation to the degree of phase separation.**

The findings strongly support our earlier conclusion that the photovoltaic properties are determined by processes on the very local scale, namely the competition between the field-induced dissociation and recombination of the initially formed polaron pair. We propose that the nanomorphology mainly affects the kinetic energy of the electron injected into the acceptor phase following exciton break-up at the heterojunction is used to decrease its mutual Coulombic binding energy with the hole remaining on the donor phase (and vice versa). The kinetics of this process is expected to depend on the direct environment of the electron-accepting chains. It might be well reduced if the density of electron-transporting sites is lowered by the presence of donor chains in intermixed acceptor-rich phases, leading to tightly bound polaron pairs. Those pairs will be more vulnerable to recombination via the formation of interfacial exciplexes or possibly via intrachain triplet excitons.[79, 128, 129] In contrast to this, rather pure donor and acceptor phases will favour the formation of spatially-extended interfacial electron-hole pairs, which exhibit a high probability to escape from their mutual Coulombic potential. These conclusions are in full agreement to recent Monte Carlo simulations on nanostructured blends by Marsh and co-workers.[130] These simulations predicted the geminate recombination efficiency to decrease from ca. 85 % for a blend with a feature size of 2.5 nm to 70 % for a domain size of 5.8 nm. At the same time the carrier collection efficiency was shown to increase remarkably.

A second important conclusion of these simulations was that the bulk charge transport is barely affected by the typical domain size. This prediction agrees well with the results of our CELIV measurements and the conclusions drawn by others from the experiments on single-carrier devices.[26, 68]

Note that changing the morphology by the use of different solvents (or annealing the sample) does not affect the principle mechanism of charge carrier photogeneration, which involves the diffusive motion of carriers under the action of the mutual Coulombic potential and the internal electric field. This is clearly evident from the close-to Langevin-type carrier recombination and the Onsager-type field-dependency of the photocurrent. It has been pointed out that a weaker field dependence of the photogeneration efficiency necessitates a reduction of the coefficient for bimolecular recombination well below the Langevin-limit.[140] As stated above strongly reduced recombination coefficients have been rarely observed in all-organic devices, as discussed above. These blends were shown to exhibit large single crystalline domains of PCBM embedded into a polymer-rich matrix.

Further efforts to improve the efficiency of polymer-polymer solar cells must, therefore, focus on the formation of interpenetrating bicontinuous networks from highly-ordered polymer domains, allowing the photogenerated holes and electrons to move independently in two different phases.

For our blends, Langevin-type recombination appears to prevail for all samples. Nevertheless by choosing a special solvent mixture of TCB:CF, a fill factor of 44% was finally achieved for the annealed blends deposited from TCB:CF. This value is among the highest reported for polymer-polymer solar cells.

# Chapter 7 Hybrid solar cells with a Vinazene electron acceptor

## 7.1 Introduction and motivation

As discussed in the introduction part, fill factor (FF) is considered as one key parameter determining the overall solar cell efficiency. State of art polymer-polymer solar cells exhibit high open circuit voltage of 1.5 V for the suitable electron-donating and accepting polymers combination.[120] However the fill factors of these devices are still below 40 % in most cases and the energy conversion efficiencies are only around 2%.[7-9,] To date, for polymer based solar cells, FFs exceeding 50 % have only been realized with selected material combinations. In the majority of these cases, fullerenes (most cases PCBM) [87, 125, 141, 142] or nanocrystalline inorganic semiconductors such as $TiO_2$ [143, 144] or CdSe [145]were used as the electron acceptor. Unfortunately, the open circuit voltage ($V_{oc}$) of these devices seldom exceeds 0.7 V. It is well accepted, the maximum open circuit voltage is defined by the energy difference between the LUMO of electron acceptor and the HOMO of the electron donor.[146] The low open circuit voltage of this kind devices is in part due to the high electron affinity of the electron-accepting phase. As is shown in Figure 51, the electron affinities of PCBM and $TiO_2$ are higher when compared to the polymer acceptors CN-Ether-PPV or F8BT, which guarantees efficient charge separation due to a large energy offset. However, when combined with generally used electron donor polymers such as P3HT or M3EH-PPV, the resulted open circuit voltages are limited to less than 1V. On the other hand, open circuit voltage ($V_{oc}$) exceeding 1V would be desirable for the direct driving of low-power electronic devices. Recently, the combination of fullerenes with small molecule or polymeric electron donors having high ionization energies resulted in open circuit voltages close to 1 V, but the FF of these devices dropped below 50 %.[15, 147, 148]

In Figure 51b, the absorption spectra of thin films from PCBM and commonly used electron accepting polymers are compared to the spectral photon flux of the solar spectrum at AM1.5. One obvious disadvantage of using PCBM is its weak adsorption in the range of the solar spectrum which leaves only the electron-donating polymer component to absorb the incident light.

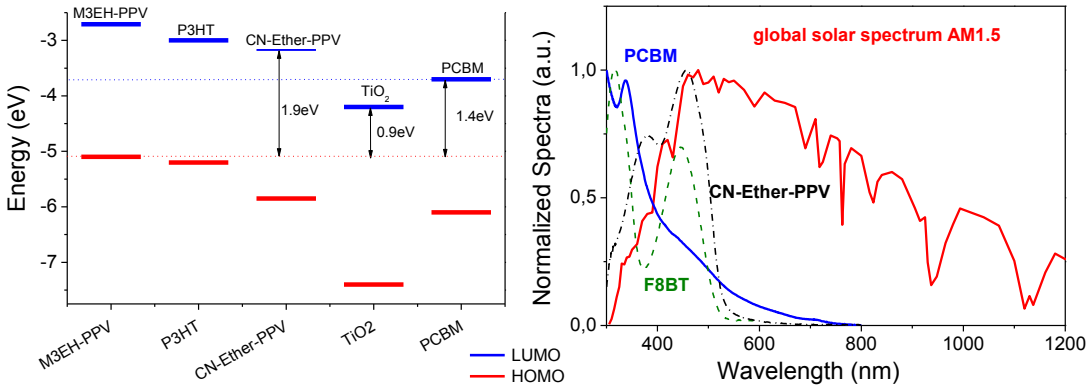


**Figure 51 a) The energy levels of electron donor polymer M3EH-PPV, P3HT and electron acceptor PCBM, CN-Ether-PPV, $TiO_2$. b) Normalized absorption spectra of PCBM, F8BT and CN-Ether-PPV compared with global solar spectrum (AM1.5).**

In this chapter, we presented a study of the photovoltaic properties of M3EH-PPV donor polymer combined with a novel molecule as electron acceptor. These studies are motivated by of the search for new electron acceptor organic materials to take the place of PCBM. Investigations were focused on the variation of the device heterojunction topology by means of varying the preparation scheme and its effect on the corresponding photovoltaic performance. Our work on PPV-based polymer blend devices, as described earlier in this thesis, suggested that the solar cell performance is determined by the field-dependent photo-generation of charge carriers. [27, 28, 81, 132, 149] The field-dependence of this process sets an upper limit to the FF. Work described earlier in this thesis has also proven that the balance between these two pathways and correspondingly the photovoltaic response is sensitive to the nanomorphology, in particular on the degree of intermixing between the two components in the phase-separated structure. [26, 27, 68] A certain degree of phase separation seems to be inevitable for enhanced device performance.

Here we proceed a step further along by tuning the heterojunction topology of the donor-acceptor (D/A) interface in polymer-Vinazene devices. The underlying processes are investigated systematically by applying different types of device architectures: (1) a distributed bulk-heterojunction in a highly intermixed D/A blend, (2) a solution processed bilayer structure with an inter-diffused D/A interface, and (3) a well defined planar D/A structure, with the acceptor layer

being thermally deposited on top of the donor, thereby strongly minimizing intermixing of the components.

## 7.2 New n-type organic seminconductor: Vinazene derivative

2-vinyl-4,5-dicyanoimidazole (Vinazene™) has been used as a precursor to design a novel family of electron-accepting materials.[150] By changing the central aromatic unit, energy of the lowest unoccupied molecular orbital (LUMO) of the resulted materials can be easily tuned to sufficiently low values guaranteeing efficient charge transfer of the photogenerated electron from the donor component. In this chapter the new vinazene derivative 4,7-bis(2-(1-hexyl-4,5-dicyano-imidazol-2-yl)vinyl)benzo[c][1,2,5-thiadiazole] (HV-BT) with a melting temperature of 208$^{o}$C and a high decomposition temperature of 402 $^{o}$C is utilized. The chemical structures of the Vinazene™ precursor and HV-BT were shown in Figure 52. The very high stability and solubility of HV-BT enables it both solution and thermal evaporation processable.

Vinazene

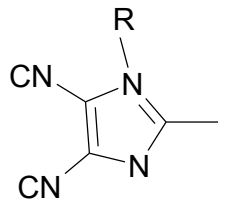


HV-BT

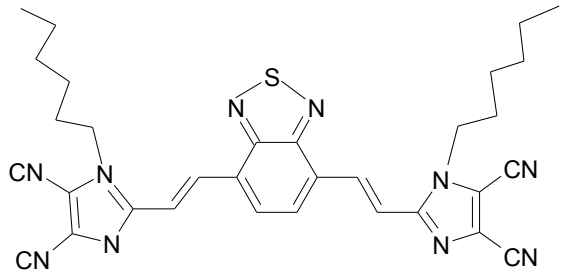


**Figure 52 Chemical structure of Vinazene™ and its derivative molecule HV-BT.**

HV-BT and M3EH-PPV have HOMO and LUMO values of -5.9 and -5.2 eV (HOMO), and -3.5 and -2.7 eV (LUMO) respectively. This leads to energy offsets at the D/A heterojunction of 0.7-0.8 eV for both electrons and holes, implying efficient dissociation of all excitons at the donor/acceptor interface. As shown by the thin film absorbance spectrum in Figure 53, M3EH-PPV and HV-BT absorb in complementary spectral regions, making this combination a promising candidate for efficient light harvesting. Furthermore, the rather low electron affinity of HV-BT near 3.5 eV enabled a technologically important open circuit voltage of 1.0 volt.

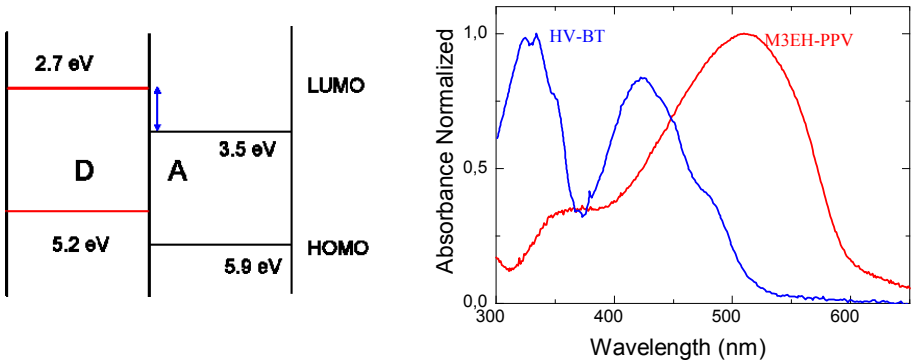


**Figure 53 Energy level scheme and normalized solid state absorption of M3EH-PPV and HV-BT.**

## 7.3 Polymer solar cells with Vinazene derivatives as electron acceptors

### 7.3.1 Recent developments

Recently, Shin et al. have fabricated blend devices of HV-BT with regio-regular electron-donating polymer P3HT. Later on, the same authors optimized the blend devices of HV-BT and poly(2,5-dioctyloxy-1,4-phenyleneethynylene-9,10-anthracenylene-ethynylene-2,5-dioctyloxy-1,4-phenylene-vinylene-2,5-di(2'-ethyl)-hexyl-oxy-1,4-phenylenevinylene (A-PPE-PPV). Open circuit voltage values between 0.87 and 0.98 V have been achieved for these two combinations.[150, 151] Surprisingly, the overall photovoltaic performance of these blend devices was rather low: optimum performance was observed for an annealed 1:1 blend of P3HT with HV-BT, with an FF of 37.3 %, an IPCE of 14 % and an ECE of 0.45 %. More recently, blends of the well-soluble Vinazene derivative 4,7-bis(2-(1-(2-ethylhexyl)-4,5-dicyano-imidazol-2-yl)vinyl)benzo-[c]thiadiazole (EV-BT) and a high band gap polymer poly[N-(2'-decyl-tetradecyl)carbazole]2,7-diyl (PCz) have been studied in detail with varying blend ratio and annealing temperatures.[152] Here, the highest FF (49 %) was observed for a 30:70 PCz:EV-BT blend annealed at 80 °C while the largest peak IPCE (20 %) was obtained for a 50:50 blend annealed at 60 °C. The strong dependence of the photovoltaic properties of polymer:Vinazene blends on the preparation conditions was attributed to different blend morphology.[151, 152] In general, as-prepared blends suffered from low fill factors and small quantum efficiencies. Structural studies with atomic force microscopy (AFM) revealed that these layers exhibit a strong intermixing of the donor and the acceptor components. Kietzke et al. proposed

that charge extraction is inefficient in these highly intermixed morphologies and that most of the photogenerated carriers recombine before being extracted to the electrodes. Layers annealed at 60°C or above resulted in a significant improvement of the device performance. For a 1:1 blend of HV-BT with P3HT, optimum performance was observed after annealing at 80°C, yielding an FF of 37.3 %, an IPCE of 14 % and an ECE of 0.45 %. This improvement was attributed to the formation of rather pure regions of the donor and acceptor molecules, which then form percolation pathways for carrier extraction to the electrodes. For the blend of EV-BT and PCz, the device characteristics depended on the annealing conditions and the blend composition in a rather complex matter: The highest *ECE* and *FF* was measured for a 70:30 EV-BT:PCz blend annealed at 80°C while *IPCE* and short circuit current were maximum for a 50:50 blend annealed at 60°C. The interpretation of these results is difficult due to the complex morphology of such solution processed blends. The resulting layers commonly display a multiphase morphology, with phase-separation in both the lateral and vertical dimension. Also, the composition of the individual phases is often ill-defined[13, 153] For example, C.R. McNeill and coworkers showed very recently that annealing of a blend of an electron-donating polythiophene and an electron-accepting polyfluorene-copolymer changes the composition of the surface, hereby altering the open circuit voltage of the solar cell.[154] To circumvent these problems, we recently fabricated interlayer devices, which feature an ultrathin layer (5–10 nm) of an electron donor, insolubilized on a polymeric anode, and an electron-accepting polymer layer deposited on top from solution.[155, 156] Our earlier studies have shown that this process yields a rather defined donor/acceptor (D/A) heterojunction with only weak interdiffusion between the two components.[156]

### 7.3.2 Blend devices

Blends of HV-BT and M3EH-PPV (1:1) were spin-coated from an 8 mg/ml solution in chloroform. A spinning speed of 2000 rpm resulted in a typical layer thickness of 60 nm, as measured with a surface profilometer (Dektak 3ST). Figure 54 shows the photoluminescence spectrum of an as-prepared blend layer on glass excited at 450 nm. As reported earlier for the 1:1 blend of HV-BT with A-PPE-PPV, the spectrum exhibits a featureless band in the NIR, which cannot be attributed to emission from either M3EH-PPV or HV-BT. This emission was

assigned to the radiative decay of an exciplex.[151] Following our recent work on polymer-polymer blends as described above, we attribute the strong exciplex component to a high degree of intermixing of the two components in the as-prepared blend. [27, 94] In addition the spectrum shows weak contributions from both M3EH-PPV and HV-BT. Note that the overall emission intensity of the blend is a factor of ca. 70 lower than that of the pure components in the solid state (not shown), suggesting that most excitons dissociate at the distributed D/A-interface in these highly intermixed layers.

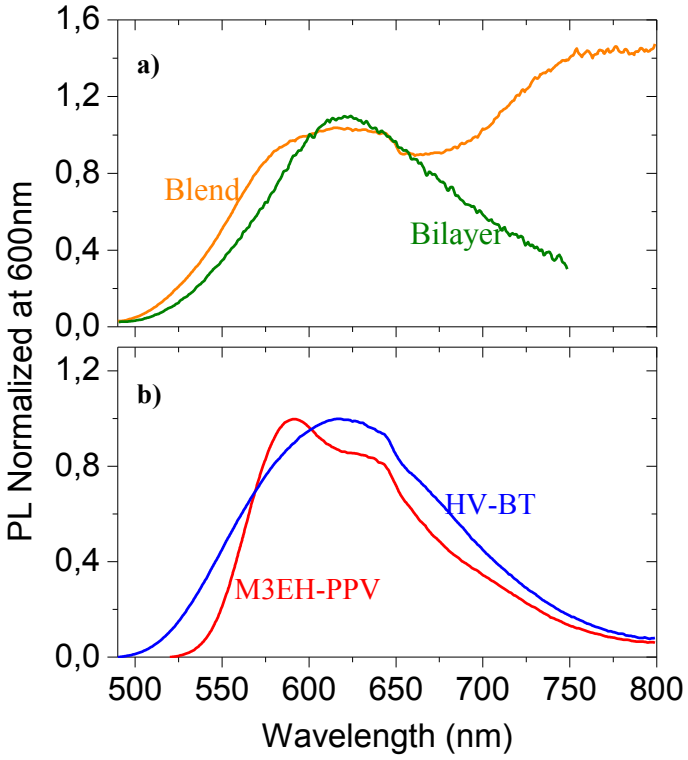


**Figure 54 Normalized photoluminescence spectra of M3EH-PPV:HV-BT 1:1 blend film (orange) and bilayer consisting of a thin M3EH-PPV interlayer and a spin-coated 35nm HV-BT layer. As comparison, the photoluminescence of pure chloroform-cast M3EH-PPV and HV-BT layers are shown respectively in graph b. The layers were excited at 450 nm.**

Figure 55a shows the IPCE spectrum of an as-prepared blend device. The IPCE is quite low and rather constant throughout the whole spectrum of the blend. The current $J_{light}$ measured under AM 1.5 illumination exhibits a $V_{oc}$ of 1 V, a short circuit current of 0.35 mA/cm$^2$ and a FF of 26 % (Figure 55b). The normalized photocurrent characteristics as shown in  exhibit a slight increase of the FF with decreasing light intensity, showing that bimolecular recombination processes or

space charge effects cannot be neglected under intense illumination. However, the FF remains low (below 35 %) even at the lowest intensity of 0.5 mW/cm$^2$.

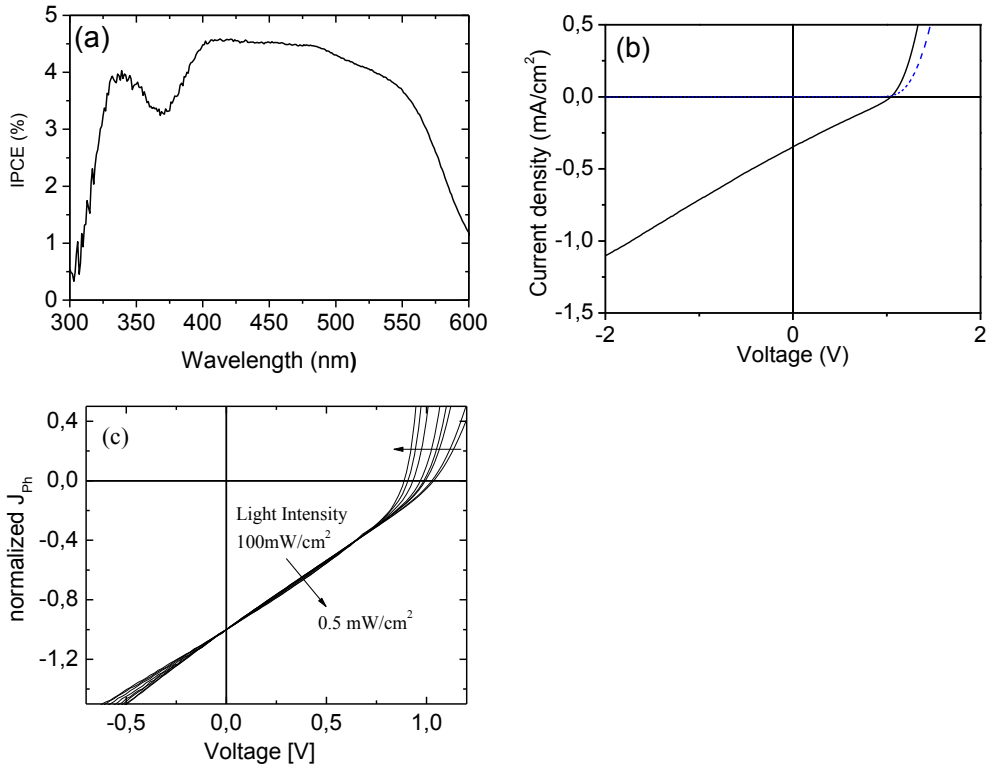


**Figure 55 ICPE (a) and I-V characteristics (b) of an as-prepared 1:1 M3EH-PPV:HV-BT blend solar cell with the active layer thickness of 60-65 nm. The dark current is shown as a dotted blue line in the right graph. Also shown are normalized photocurrent characteristics measured under white light illumination with intensity *I* of 0.5, 1, 2.5, 5, 10, 50 and 100 mW/cm$^2$ (c).**

As also discussed in the previous two chapters, low fill factors have been commonly observed in as-prepared blends of polymers. It was attributed to the strong confinement of the initially formed polaron pairs in a rather homogenous mixture of the D/A components, leading to a strong dependence of the photogeneration efficiency on the internal field.[26, 132, 157] The strong exciplex contribution in the PL spectrum discussed above, and the rather smooth and homogeneous surface in the Atomic Force Microscopy (AFM) topography image shown in Figure 56, point indeed to a high degree of intermixing in our as-prepared M3EH-PPV:HV-BT blend layers. Similar conclusions have been drawn from earlier studies on as-prepared polymer:HV-BT blend layers.[150, 151]

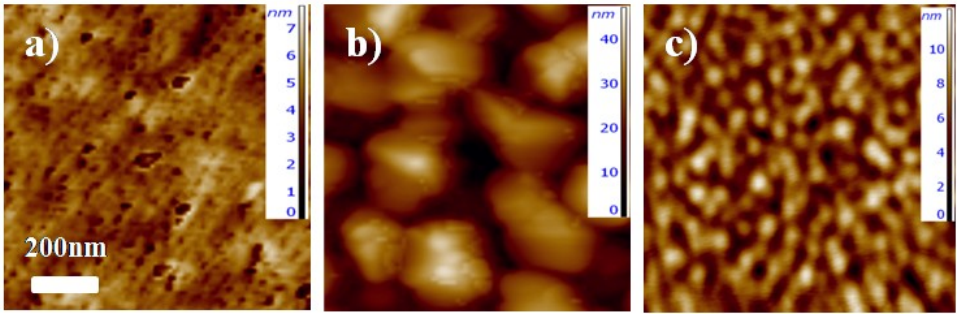


**Figure 56 Atomic force microscopy (AFM) topography images of a) an as-prepared 1:1 M3EH-PPV:HV-BT blend (spin-coated from CF) on PEDOT:PSS; b) a pure spin-coated HV-BT film and c) a pure high vacuum deposited HV-BT film on a M3EH-PPV interlayer.**

The photovoltaic properties of our as-prepared blends are quite comparable to those reported for non-annealed blends of HV-BT with either A-PPE-PPV or P3HT. [150, 151] As pointed out above, annealing of A-PPE-PPV:HV-BT blends led to an increase of the IPCE to 14 %, which was attributed to thermally-induced phase separation of the two components.[151] However, the blend morphology as well as the composition of the phase-separated domains is not well-defined in most polymer blends. [13, 153]

### 7.3.3 Bilayer devices

7.3.3.1 Solution processed acceptor layer

In chapter 4 we have shown that a bilayer system consisting of an interlayer of donor polymer covered by a spin-coated layer of an acceptor polymer yields a defined heterojunction with only weak interdiffusion between the two components.[28] To introduce a well-defined phase separation between the two components we fabricated interlayer devices, which feature an ultrathin M3EH-PPV layer (~10 nm) insolubilized on top of the PEDOT:PSS layer. Followed, a 35 nm layer of HV-BT was spin-coated on top from a chloroform solution. As a result of the separate paths for the extraction of electrons and holes, bimolecular recombination should be negligible in such a bilayer structure.

Shown in Figure 57 is the IPCE spectrum and the current-voltage characteristics of such an interlayer device. The key photovoltaic parameters are largely improved compared to the blend device. With a maximum ICPE of 27 %, a $V_{oc}$ of 1.04 V, a $J_{sc}$ of 1.8 mA/cm$^2$ and a FF of 43 %, the interlayer device exhibits an ECE of 0.80 %. This is almost double the ECE achieved for the optimum

polymer-HV-BT combination in earlier studies.[150, 151] However, the photocurrent clearly depends on the internal electric field throughout the measured voltage range, leading to an only moderate FF value. It indicates that the polaron pair remains strongly bound also in the interlayer device.

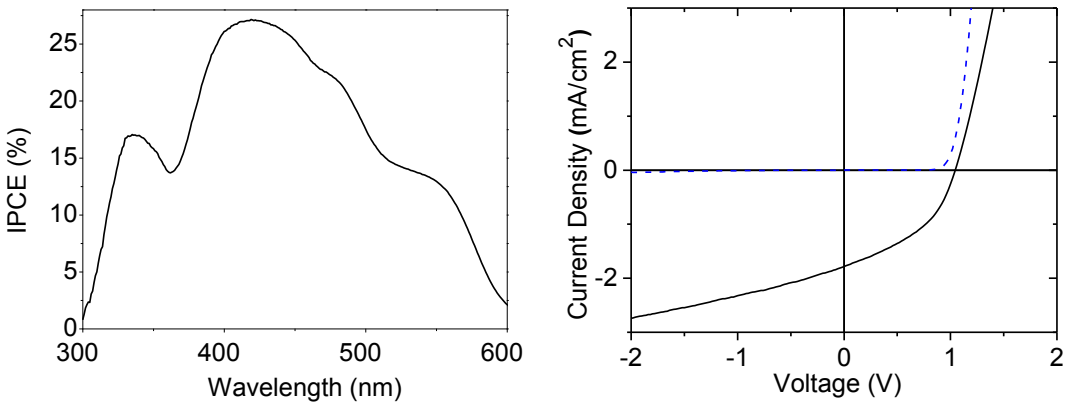


**Figure 57 IPCE and the I-V characteristics (measured under 100 mW/cm$^2$, AM 1.5 illumination) of an all-solution processed bilayer device comprising a ca. 10 nm M3EH-PPV interlayer and 35 nm HV-BT layer. The dark current is shown as a dotted blue line in the right graph.**

### 7.3.3.2 Vacuum processed acceptor layer

Finally, bilayer devices with a discrete heterojunction were fabricated with the acceptor layer thermally evaporated. The bilayer devices were prepared with a 30 nm thick HV-BT layer evaporated in a high-vacuum chamber ($2x10^{-7}$ mbar base pressure, 0.5 Å/s deposition rate) on top of a 20 nm spin-coated M3EH-PPV film. To allow a direct comparison with the all-solution processed bilayer structure as discussed above, an additional reference device consisting of a HV-BT layer evaporated onto a M3EH-PPV interlayer (10 nm) was also fabricated. The IPCE spectra and current-voltage characteristics of these devices are shown in Figure 58. Both types of devices (with a regular spin-coated donor layer or an interlayer) behave almost identically, indicating that the method used to prepare the donor layer has a minor effect on device performance.

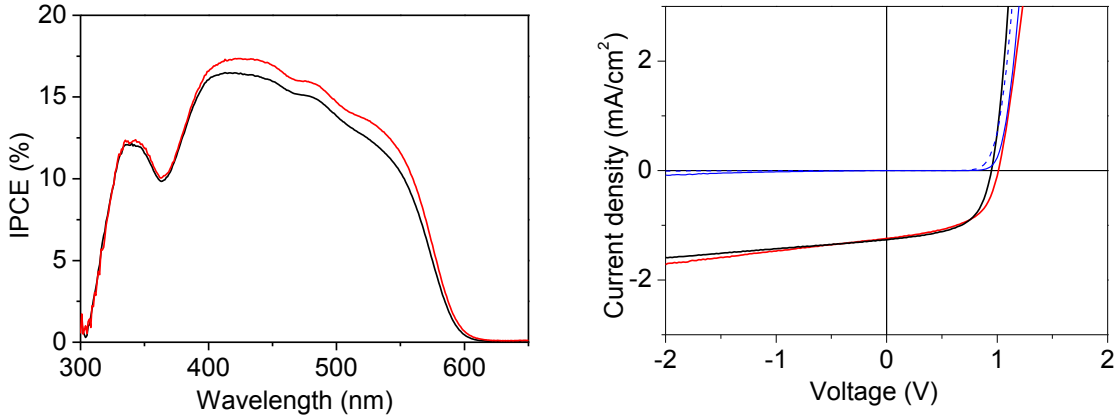


**Figure 58 IPCE and the I-U characteristics (measured under 100 mW/cm$^2$, AM 1.5 illumination) of discreet bilayer devices with a 30 nm HV-BT vacuum-deposited layer. The black lines represent the device with a 20 nm thick spin-coated M3EH-PPV layer, with the corresponding dark-current shown as a blue dashed line. The red curves were recorded for a device with a 10 nm thick M3EH-PPV interlayer, with its dark current presented by a blue solid line.**

Going from the interlayer device with a solution-processed HV-BT layer to a evaporated bilayer structure leads to remarkable increase in the FF up to 57 %. At the same time the Voc remained near 1 V.

## 7.4 Results and discussions

The photovoltaic parameters of all devices investigated are summarized in Table 12. It can be seen that the method of acceptor layer deposition has a large influence on the photovoltaic properties.

**Table 12 Photovoltaic properties of the four solar cell types. Except for the IPCE, all values were measured under AM1.5 conditions with light intensity of 100 mW/cm$^2$.**

| | | $V_{oc}$ [V] | $J_{sc}$ [mA/cm$^2$] | FF [%] | IPCE [%] | ECE [%] |
|---|---|---|---|---|---|---|
| **Blend (CF-spin coated)** | | 1.04 | 0.35 | 26 | 4.5 | 0.1 |
| **M3EH/PPV Interlayer** | HV-BT spincoated | 1.04 | 1.8 | 43 | 27 | 0.8 |
| | HV-BT evaporated | 1.02 | 1.3 | 54 | 17 | 0.7 |
| **M3EH-PPV spin coated** | HV-BT evaporated | 0.95 | 1.3 | 57 | 16 | 0.7 |

To exclude that these effects are caused by differences in the charge transport properties of the acceptor layer, pure HV-BT layers prepared either from solution

or deposited from vacuum were studied by means of the photo-CELIV method. The setup and measurement technique used in this study are described in the Appendix. The thickness of the evaporated and spin coated HV-BT layer was 35 nm and 55 nm, respectively. From the maximum of the extracted current, a mobility of $3x10^{-6}$ $cm^2/Vs$ was found for evaporated HV-BT, which is very similar to $2x10^{-6}$ $cm^2/Vs$ measured for solution processed HV-BT. The close correspondence between these two values is rather intriguing, keeping in mind the different methods employed for the preparation of the HV-BT layers and the differences in layer morphology (see the corresponding AFM images in Figure 56).

These findings suggest that the photovoltaic properties of devices comprising either a solution-deposited or an evaporated acceptor layer are not determined by the bulk of the individual semiconducting layers, but by processes at the D/A heterojunction. Most likely, deposition of HV-BT onto an M3EH-PPV interlayer from chloroform solution results in weak interdiffusion of the acceptor molecules into the polymer film. For example, the M3EH-PPV interlayer is expected to swell in the presence of chloroform, allowing the HV-BT molecules to penetrate into the insolubilized polymer layer. In fact, the emission of the solution-processed bilayer device as shown in Figure 54 does not exhibit any contribution from M3EH-PPV, suggesting that excitons generated on the polymer are rapidly quenched by the acceptor.

This interpretation is supported by the higher IPCE of the all solution processed bilayer device in comparison to the discreet bilayer. In the latter structure only excitons which are generated within the exciton diffusion length from the D/A interface can contribute to the photocurrent (the so-called exciton diffusion bottleneck).[158] Currently we have no information regarding the exciton diffusion length in either M3EH-PPV or HV-BT. For other soluble PPV-based derivatives, exciton diffusion lengths between 5 and 8 nm have been reported,[159, 160] which is well below the penetration depth of light in our semiconducting layers. An intermixed layer formed at the heterojunction in the all-solution processed bilayer devices will effectively add a photoactive region to the device structure. Hybrid planar-mixed heterojunctions, comprising a mixture of the donor and acceptor components between layers of pure donor and acceptor molecules have been shown to outperform planar heterojunction devices with regard to IPCE and ECE

values.[142] In our present study, the IPCE of the all-solution processed bilayer devices is a factor of 1.5 larger than that of the discreet bilayer devices, suggesting that the intermixed region must extend several nanometers across the heterojunction.

Based on the strong dependence of the FF and IPCE on the device architectural features, we conclude that the D/A interfacial "topography" as schematically depicted in Figure 59, dramatically influences the efficiency for free carrier generation.

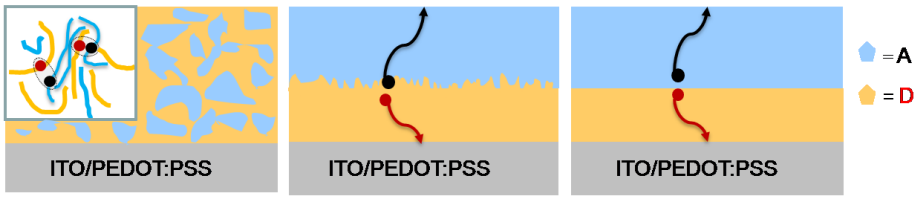


**Figure 59 Schematic drawings depicting the interfacial topology at D/A heterojunction (topology), for a blend device (left), the all-solution processed interlayer device (center) and the discreet bilayer with a vacuum processed acceptor layer deposited on top of the solution-cast polymer film (right). A closed view of geminate pair recombination is shown at upper corner of the left picture.**

The AFM images in Figure 56 suggest that both the solution-cast and evaporated HV-BT layers consist of crystallites. In conjunction with a well-defined heterojunction topology, the nanocrystalline morphology allows for the photo-generated electrons to quickly migrate into the acceptor phase away from the hetero-interface, thereby reducing the mutual Columbic binding energy to the hole remaining in the donor phase. With increasing interdiffusion of the D/A components across the heterojunction, this process is slowed down as donor molecules replace electron-transporting molecules within the acceptor phase (and vice versa). Consequently, the initially generated electron-hole pair becomes more localized, resulting in a stronger field dependence of the free carrier efficiency generation and concurrently a lower FF. In other words, the formation of pure and possibly crystalline phases seems to be a necessary condition for achieving high FF. This interpretation is in accordance with the conclusions from studies on blends of MDMO-PPV with the soluble fullerene derivative PCBM.[161] In this case, high FF and large open circuit currents were only observed under conditions which enable the formation of single crystalline domains of PCBM embedded into a polymer-rich matrix. Note that the open circuit voltage is nearly the same for all

of our devices. It shows that the heterojunction topology does not affect the energy of the active layers or at the electrodes. This result suggests that the strong correlation between the degree of donor-acceptor intermixing and fill factor is directly related to the heterojunction topography.

## 7.5 Conclusion

In this chapter we demonstrated the observation of a very pronounced correlation between the heterojunction topology and the photovoltaic properties, particularly the IPCE and the FF. The experiments data reveals that with a decreasing degree of intermixing (going from the blend to the discreet bilayer structure) the FF increases from 30% to 57%. Recently, solar cells based on entirely evaporated small molecule layers have been shown to exhibit FF values in excess of 50 % with a $V_{oc}$ near 1 V.[162, 163] To best of our knowledge, the device results presented here are the first polymer-based solar cells featuring very high FF and $V_{oc}$ values under AM1.5 illumination. Concurrently, the rather low electron affinity of the HV-BT acceptor used in this study enabled devices with a technologically important $V_{oc}$ = 1V. This suggests the combination of M3EH-PPV with HV-BT to represent a rather unique D/A combination with well-balanced electronic properties. According to best of our knowledge, the device we present here is the first polymer-based solar cell with both very high fill factor and open circuit voltage. Hence, HV-BT and related derivatives shall, therefore, be considered as potential candidates for the replacement of fullerene based acceptors.

# Chapter 8 Summary and Outlook

## Summary

The aim of this thesis was to acquire a deep understanding of the working mechanism of polymer-based solar cells and to improve the device performance.: Two types of the solar cells were studied here: all-polymer solar cells comprising macromolecular donors and acceptors based on poly(p-phenylene vinylene) and hybrid devices hybrid cells combining a PPV copolymer and a novel small molecule electron acceptor

The main conclusion of the thesis is the proposal that the main factor limiting the performance of polymer-polymer solar cell efficiency is the inefficient free charge carrier generation, while charge transport and extraction play only a minor role. We based this proposal on the following findings:

1. The observation of a strict anti-correlation between the photocurrent and the intensity of long wavelength exciplex emission in the photoluminescence spectra of the blend layers. This lead us to the conclusion that the photocurrent efficiency is governed by processes on the local scale and not on "macroscopic" device properties such as charge transport or extraction.
2. By comparing the photocurrent characteristics of bilayer and blend devices we could unambiguously show that bimolecular recombination and charge extraction do not compromise device performance, leaving the field-dependence of charge carrier generation as the main reason for the low fill factor.[27, 28]
3. The efficiency of the initial generation of carriers largely depends on the blend morphology, which can be widely controlled by annealing or by using solvent mixtures. We found conclusive evidence that annealing leads to a higher degree of phase separation which in turn increases the probability for the dissociation of electron-hole pairs bound at the heterojunction into free carriers.

Based on these findings we developed a novel approach to tune the nano-morphology blend layers consisting of the electron-donating polymer M3EH-PPV and the electron-accepting polymer CN-Ether-PPV. Hereby, a mixture of two

solvents was used: CF is a good solvent for both polymers, while TCB is a selective solvent for CN-ether-PPV Therefore, M3EH-PPV will first solidify upon drying of the layer, resulting in a well-defined phase-separated blend morphology. Using this approach, devices with a high fill factor of 44% were achieved, which is among the highest values reported for polymer-polymer solar cells.
Nevertheless, even for optimized preparation conditions, the fill factors of these polymer-polymer solar cells remained well below those found for polymer-small molecule based devices.
We, therefore, studied in detail the spectroscopic and photovoltaic properties of the combination of the hole-transporting polymer M3EH-PPV with a novel Vinazene-type small molecule electron acceptor. This molecule can be either deposited from solution or by thermal evaporation, allowing for a large variety of layer architectures to be realized: polymer-vinazene blend devices made from solution (type I), polymer-vinazene bilayer devices coated entirely from solution using the interlayer approach (type II) and strict bilayer devices with vinazene deposited on M3EH by thermal evaporation (type III). In particular we could show that the as-prepared blend is a homogeneous mix of the two components and that the solution processes bilayer (type II) contains a diffuse interface. Apparently, the use of different preparation conditions allowed us to fine-tune the spatial distribution and thus the interaction between the electron-donating and the electron-accepting component in the active layer.
We have then demonstrated that the layer architecture has a large influence on the photovoltaic properties. While blend devices exhibited overall low quantum efficiencies and fill factors (not exceeding 30 %), the strict bilayer (type III) devices showed very high fill factors of up to 57 % and an open circuit voltage of 1V without thermal treatment of the devices. In the past, fill factors exceeding 50 % have only been observed when using fullerene-derivatives as the electron-acceptor. The finding that proper processing of polymer-vinazene devices leads to similar high values is a major step towards the design of efficient polymer-based solar cells.

## Outlook

With the aim of improving polymer solar cell efficiency, future effort will be concentrated on the following aspects:

1. *Control the morphology and improve charge carrier generation efficiency*.
   As is demonstrated in this thesis, photocurrent generation is strongly related to the nano-morphology of the active polymer-blend layer. Geminate pair recombination plays a key role in limiting the device performance. We further found that the formation of rather homogenous mixture of the donor and acceptor moieties favors geminate recombination and leads to a strong field-dependence of the external photocurrent. Further efforts to improve the efficiency of polymer-polymer solar cells must, therefore, focus on the formation of interpenetrating bicontinuous networks from highly-ordered polymer domains, allowing the photogenerated holes and electrons to move independently in two different phases.

   An alternative approach will be synthesis of blockcopolymer with D-A components. The blockcopolymer might be either used as the active material directly or just as a template to form more ordered structure due to the chemical interactions between the active material and the template.

2. *Improve charge transport and the open circuit voltage*
   A promising approach for achieving higher open circuit voltage will be developing novel electron acceptors with high charge carrier mobility, suitable energy levels and better absorption on the visible light range. Our experiments on the combination of M3EH-PPV and a Vinazene-type electron acceptor have shown that high fill factors and high open circuit-voltages can be reached in polymer-based devices even without using fullerenes. However, the efficiencies of these devices were still rather low and most likely limited by the fractions of excitons reaching the heterojunction. Further improvements in efficiency require more sophisticated device architectures with a well-distributed nanostructured heterojunction between domains of pure donor and acceptor, hereby

improving exciton dissociation, free charge carrier generation and finally, charge extraction to the electrodes. In addition, chemical modifications are needed to broaden the absorption range, thus reducing the currently existing spectral mismatch with the sun light spectrum.

# Chapter 9 Appendix

## 9.1 Experimental methods

### 9.1.1 Steady state spectroscopy

Optical absorption spectra of solutions and thin films were measured with a Perkin-Elmer Lambda 9 UV-Vis spectrometer. The spectra were corrected for the transmission of the substrate (ITO/PEDOT:PSS or Glass). Most absorption spectra were taken from the completed devices by directing the light beam through the space between the pixels. Photoluminescence spectra were measured with a Perkin-Elmer LS 50/55 luminescence spectrometer. The samples were illuminated from the front side with an incident angle of 60° and the spectra were recorded in reflection at 30° with respect to the surface.

### 9.1.2 Time-resolved photoluminescence

The time-resolved fluorescence spectra measurements were performed by using a single photon counting setup. For the excitation of the samples a frequency-doubled titanium:sapphire laser (Tsunami, Spectra Physics) was used. The excitation pulse width was determined to be 100 fs by using an autocorrelator (Pulse Check, APE, Berlin). Fluorescence spectra were measured with a FL920 fluorometer (Edinburgh Instruments, Livingston, U.K.). The complete detection system had an instrumental response time of 100 ps. For data analysis and deconvolution of the instrument response function, the commercial software package provided with the FL920 fluorescence spectrometer was used.

### 9.1.3 Photo-CELIV measurements

The samples for the Photo-CELIV measurements were prepared by spin-coating polymer solution on the PEDOT:PSS coated pre-structured ITO substrates. Aluminium top electrode instead of the combination of Ca and Al was used here in order to reduce the charge injection. The measurement setup is sketched in Figure 60. A frequency-tripled Nd:YAG laser at 355 nm with ca. 20 ns laser pulse is applied to generate charge carriers. A certain voltage with regulated delay time to the light pulse was generated by using a digital voltage pulse generator (Agilent

33220A). The transient current was amplified with a current amplifier (FEMTO). All the signals were then transferred to the computer via a digital Oscilloscope (Yakagawa DL9040).

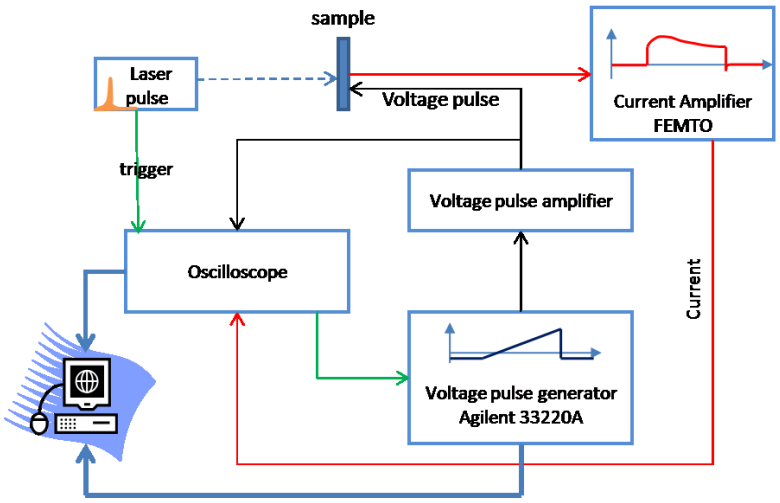


**Figure 60 A typical experimental setup for the photo-CELIV measurement.**

During and after excitation, an external forward bias voltage $U_{bias} = -U_{bi}$ was applied to compensate the built-in potential $U_{bi}$ of the sample, resulting in a near-zero electrical field inside the polymer layer. The built-in potential was determined to be the point where the photocurrent was equal to zero. After a delay time $t_d$, the photo-generated charges were extracted by linearly increasing the applied reverse voltage with the slope $A=U/t_{pulse}$ up to ~10 V within several micro seconds.

### 9.1.4 Atomic Force Microscopy

In this thesis, atomic force microscopy (AFM) with tapping model was applied.

In Figure 61, the basic working principle of the AFM is shown. The sample surface is scanned by a tip located at the end of the cantilever. The interactive forces between the tip and the surface cause bending of the cantilever on the Angstrom scale. Light from a laser diode bounces off the cack of the cantilever onto a photodiode which serves as a position-sensitive detector. The bending of the cantilever is amplified by the shifts of the position of the laser beam on the detector as shown in the right graph of Figure 61. A piezoelectric crystal, which is controlled by a feedback circuit, then will contract or expand until the laser spot hits the same position on the diode as before. The change in the length of the

piezo crystal corresponds to a variation in the sample height. Thus, surface topologies can be measured with high lateral and vertical resolution.

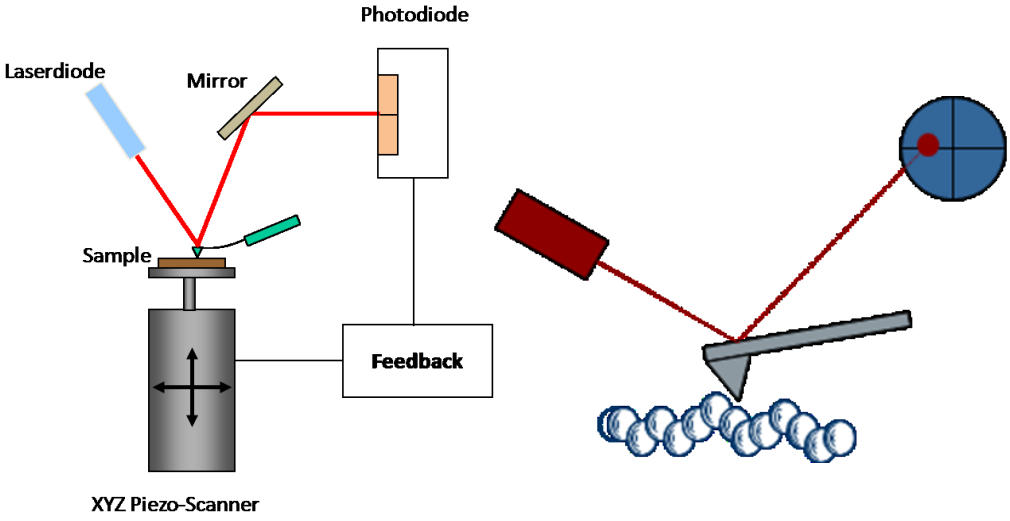


**Figure 61 Left: Schematic drawing of the working principle of atomic force microscopy. Right: a close view of the scheme for detecting the cantilever bending.**

According to different purposes, an AFM has three common modes: contact mode, non-contact mode and tapping mode. In the contact mode, as the tip scans in directly contact with the sample surface the sample, the contact force causes the cantilever bending in order to follow the sample topography profile. However when soft polymer layers are investigated, the polymer film might be destroyed if the contact mode is applied. In this kind of situation the non-contact mode is often used. In this mode, the tip (and the cantilever) vibrates about 50-150 Å above the sample surface. While the tip scans over the sample, the system detects the amplitude of the swing of the cantilever and keeps it constant with the aid of feedback system that moves the scanner up and down. The Van der Waals forces between the tip and the sample are detected and topographic images are constructed by scanning the tip above the surface. Unfortunately, the lateral resolution in the non contact mode is less than the contact mode. In this thesis, the tapping mode was used. Tapping mode overcomes problems associated with friction, electrostatic force and other difficulties often exist in the AFM method with contact mode. Compare to the non contact mode, it provides higher resolution by alternately placing the tip in contact with the surface and then lifting the tip off the surface to avoid the tip dragging across the sample surface. In the tapping mode, the cantilever oscillates with a certain frequency (10-400 kHz,

depending on the cantilever design) at an average distance of 10-100 nm away from the sample surface, so that it only taps the surface for a very small fraction of its oscillation period. When the distance between tip and sample is reduced, the vibrational amplitude of the cantilever is lowered due to damping. A feedback loop detects the drop in the amplitude and increases the tip sample distance by contracting the piezo until the original amplitude is reached again. The phase images are obtained by measuring the phase difference between the oscillations of the cantilever driving piezo and the detected oscillations.

### 9.1.5 Kelvin probe

The Kelvin probe technique was first postulated by the Scottish scientist William Thomson (later to be known as Lord Kelvin) in 1898.[164] In the beginning of 19$^{th}$ century, he demonstrated charge transfer between two large flat metal plates by using a gold leaf electroscope. Today, the Kelvin probe is considered a very powerful analytical tool which measures the difference in contact potential between a reference material (probe) and a sample.[77, 165, 166] A major advantage of this method is that the surfaces do not need to touch each other. It also requires only very weak electrical fields, hence large influences on the electrical or chemical structure of materials are very unlikely.[20] It is well suited for the study of fragile and soft matters such as organic materials.

The basic working principle of this method is illustrated in Figure 62. When the two plates with different surface potentials are electrically connected, an internal electric field is generated and a compensation current flows from the material with higher work function to the one with lower work function. This potential difference between the two plates can be detected by applying an external potential, (compensation potential) $V_{dc}$ to nullify the internal electric field induced by the contact potential difference φ. If the work function of the reference probe is known as $\varphi_1$, the work function of the sample can be determined as $\varphi_2 = \varphi_1 - \varphi$.

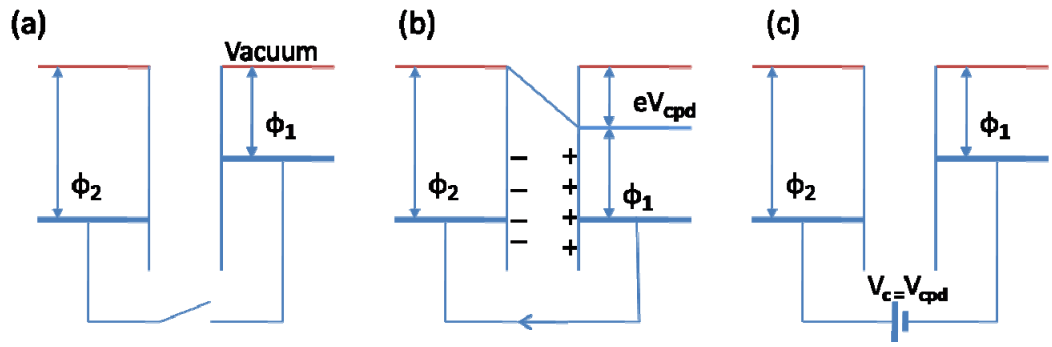


**Figure 62 Basic working principles of the Kelvin probe method. a) Sample and probe with different work functions, without contact. b) Compensation current flows when the two plates are electrically connected. The contact potential difference is represented as φ. c) The electric field is compensated by applying the external voltage $V_{dc}$, with $V_{dc} = \varphi$.**

The Kelvin probe used in this thesis is a home-built setup (see Figure 63). It consists of a flat circular gold electrode (probe) suspended above and parallel to the sample. An oscillator is connected to a piezoelectric stage and spring to control the movement of the probe. The oscillator applies a sinusoidal waveform to the probe causing a constant oscillation of frequency (ω), at a variable amplitude and height.

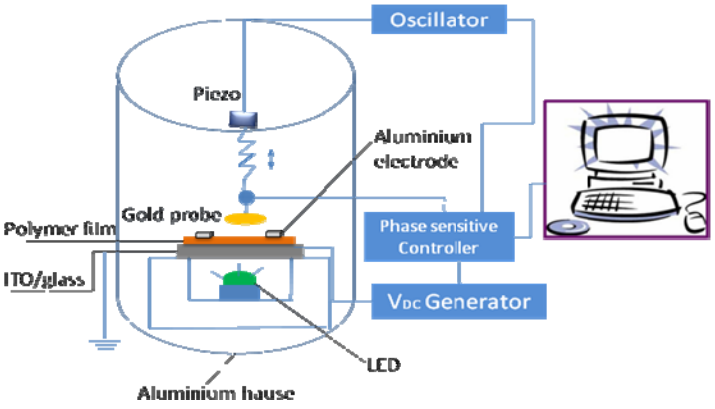


**Figure 63 Schematic drawing of the Kelvin probe setup used in this thesis.**

In order to obtain an exact measurement of the work function of the sample, both an alternating current (AC) and a direct current (DC) voltage were applied. The DC voltage $V_{dc}$ was used to minimize the electrostatic interaction between the tip and the surface. The AC voltage $V_{ac}$ is applied to detect the electrostatic forces, which were used for the distance control. In our setup the probe is ca. 2 mm above the sample with vibrating amplitude of 0.1 to 0.5 mm. With the vibration of the probe, an alternating current flow is produced which can be easily and

precisely detected. This concept has been used for many materials and has obtained very high resolution of the potential differences down to 1mV. The sample and probe are connected via a voltage source which applies a DC bias voltage $V_{dc.}$

With the vibration of the probe a varying capacitance is created. This is given by

$$C = \frac{Q}{V} = \frac{A\varepsilon_r\varepsilon_0}{d}$$

Where $C$ is the capacitance, $Q$ is the charge, $V$ is the potential, $A$ is the surface area of the probe and $d$ is the separation distance between the probe and the sample. The movement of the probe can be expressed by:

$$d(t) = d_0 + d_1\cos(\omega t)$$

Where $d_0$ is the average distance between the sample and the probe, $d_1$ is the amplitude of oscillation of the probe, and $\omega$ is the angular frequency of vibration. When the separation distance $d$ increases the capacitance $C$ decreases. As the charge remains constant, the output voltage must increase. The change of the voltage over time is recorded as shown in Figure 64. The peak to peak output voltage is given by:

$$V_{output} = (\varphi - V_{dc})RC_0\omega\frac{d_1}{d_0}\sin(\omega t + \phi)$$

Where $\varphi$ represents the contact potential of the surface, $V_{dc}$ is the applied voltage used to balance the circuit, $R$ is the resistance, $C_0$ is the mean Kelvin Probe capacitance.

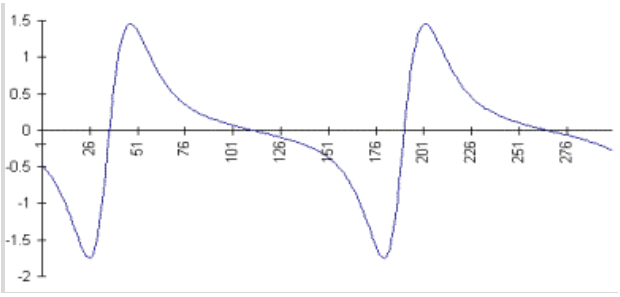


**Figure 64 Kelvin probe signal changes over time (reproduced from reference [167])**

At the point $V_{output}$=0, the contact potential of the surface $\varphi$ (difference in work function between the probe and the sample) is equal and opposite to the applied voltage $V_{dc}$.

In order to investigate the surface potential change of the polymer films in dark and under illumination, the sample is illuminated by a super-bright LED with an

emission maximum at 475 nm. The whole sample and measurement probe is covered with an aluminium cylinder cover to minimize the influence of the environment field and the room light. The measurement is done first to measure the Kelvin potential of the sample in dark, and then under illumination. The so measured potential difference in dark and under illumination is taken for direct comparison between different solar cell device architectures.

A disadvantage of this method is that the measured potential represents an average of the local work functions over the whole sample surface. Thus no detail on local potential variations on the sample surface could be obtained. Nevertheless, in our case only the relative difference of the surface potentials was studied, the measurement results were still reliable even though the measurements were performed in air.

## 9.2 Curriculum Vitae

**Name**: Chunhong Yin

**Born:** July.4th.1976, Hebei, China

**Education background:**

| | |
|---|---|
| 09/1994-07/1998 | Studied in Beijing University of Chemical Technology<br>Degree: Bachelor of Engineering |
| 10/2003-08/2005 | Studied in 'Polymer Science', an international joint master program of TU,FU,HU Berlin and Uni Potsdam, Germany<br>Degree: Master of Science |
| 10/2004-09/2005 | Master thesis in physics faculty at University of Potsdam with the topic of 'PPV polymer based heterojunction photovoltaic cells' |
| 10/2005-10/2008 | PhD studies in physics at University of Potsdam |

**Career summary:**

| | |
|---|---|
| 08/1998-01/2000 | Assistant engineer in Research and Development department of Beijing Latex Factory |
| 01/2000-07/2000 | Editor of the internet website of the National Information Center China Society Development Department, Beijing. |
| 08/2000-09/2003 | Manager of Market Layout Department in Beijing Xinnet Corp. |

**Awards:**

| | |
|---|---|
| 06/1998 | Bachelor thesis was chosen as 'Excellent Graduate Thesis' |
| 06/2008 | Student Award from European Materials Research Society (EMRS) 2008 spring meeting conference |

## 9.3 List of publications


1. Chunhong Yin, Thomas Kietzke, Michael Kumke, Dieter Neher and Hans-Heinrich Hörhold, *Relation between Exciplex Formation and Photovoltaic Properties of PPV Polymer-based Blends*, Solar Energy Materials & Solar Cells **91**, 411 (2007)

2. Chunhong Yin, Thomas Kietzke, Dieter Neher and Hans-Heinrich Hörhold, *Photovoltaic Properties and Exciplex Emission of Polyphenylenevinylene-based Blend Solar Cells,* Applied Physics Letters **90**, 092117 (2007).

3. Chunhong Yin, Björn Pieper, Burkhard Stiller, Thomas Kietzke and Dieter Neher, *Charge Carrier Generation and Electron Blocking at Interlayers in Polymer Solar Cells,* Applied Physics Letters **90**, 1335502 (2007).

4. Chunhong Yin, Marcel Schubert, Sebastian Bange, Burkhard Stiller, Michael Kumke, Hans-Heinrich Hörhold and Dieter Neher, *Tuning of the Excited State Properties and Photovoltaic Performance in PPV-based Polymer Blends,* The Journal of Physical Chemistry C **112**, 14607 (2008).

5. Marcel Schubert, Chunhong Yin, Mauro Castellani, Sebastian Bange, Teck Lip Tam , Allan Sellinger, Hans-Heinrich Hörhold, Thomas Kietzke and Dieter Neher, *Heterojunction Ttopography versus Fill Factor Correlations in Novel Hybrid Small-molecular/polymeric Solar Cells*, **submitted to** Journal of Chemical Physics.

## 9.4 Conferences Attendance

**Oral Presentations:**

June 2006: European Conference Of Hybrid Solar Cells (ECOH'S) in Paris, France
Title: Relation between exciplex formation and photovoltaic properties of PPV polymer based blends

May 2008: European Materials Research Society (EMRS) spring meeting conference in Strassbourg, France
Title: Hybrid small-molecular/polymeric solar cells with high fill factor up to 57%

Oct 2008: 11th European Conference on Organized Films (ECOF), in Potsdam, Germany
Title: Towards the design of efficient polymer-based solar cells

**Poster Presentations:**

Mar. 2006: DPG Spring Meeting, Dresden, Germany
POSTER : Exciplex dynamics in a M3EH-PPV:CN-Ether-PPV blend film and a D-A block copolymer film

Aug 2006.: ECOF (the European Conference on Organized Films), Riga, Latvia
POSTER: Charge Transfer Studies in Well-defined Polyemr Solar Cells Heterostructures Studied by the Kelvin Probe Method.

Mar 2007.: VolksWagen foundation project meeting, Kerkrade, the Netherlands
POSTER: Anticorrelation between exciplex emission and photovoltaic efficiency in PPV polymer based solar cells

Mar. 2007: DPG Spring Meeting, Regensburg, Germany
POSTER: Anticorrelation between exciplex emission and photovoltaic efficiency in PPV polymer based solar cells

May 2007: EMRS spring meeting, Strassbourg, France
POSTER: Determination of photocurrent in polymer solar cells

Feb.2008: International Symposium: 'Towards Organic Photovoltaics', Linz, Austria
POSTER: Towards hybrid small-molecular/polymeric and organic/ inorganic solar cells

Jul. 2008: Polydays 2008: Active and Adaptive Polymeric Materials, Berlin, Germany
POSTER: Towards high efficiency polymer solar cells—the relationship between nanostructure and photovoltaic performance

# References


[1] G. A. Chamberlain, Solar Cells **8**, 47 (1983).
[2] C. W. Tang, Applied Physics Letters **48**, 183 (1986).
[3] J. Xue, B. P. Rand, S. Uchida, et al., Advanced Materials **17**, 66 (2005).
[4] S.-S. Kim, S.-I. Na, J. Jo, et al., Advanced Materials **19**, 4410 (2007).
[5] J. J. M. Halls, C. A. Walsh, N. C. Greenham, et al., Nature **376**, 498 (1995).
[6] G. Yu, J. Gao, J. C. Hummelen, et al., Science **270**, 1789 (1995).
[7] T. Kietzke, H.-H. Hörhold, and D. Neher, Chemistry of Materials **17**, 6532 (2005).
[8] M. Koetse, J. Sweelssen, K. Hoekerd, et al., Applied Physics Letters **88**, 083504 (2006).
[9] C. R. McNeill, A. Abrusci, J. Zaumseil, et al., Applied Physics Letters **90**, 193506 (2007).
[10] J. Y. Kim, K. Lee, N. E. Coates, et al., Science **317**, 222 (2007).
[11] B. O'Regan and M. Grätzel, Nature **353**, 737 (1991).
[12] U. Bach, D. Lupo, P. Comte, et al., Nature **395**, 583 (1998).
[13] H. J. Snaith, A. J. Moule, C. Klein, et al., Nano Letters **7**, 3372 (2007).
[14] M. Grätzel, Progress in photovoltaics: research and applications **8**, 171 (2000).
[15] K. Schulze, C. Uhrich, R. Schüppel, et al., Advanced Materials **18**, 2872 (2006).
[16] J. Simon and J.-J. Andre, *Molecular Semiconductors: Photoelectrical Properties and Solar Cells* (Springer, 1985).
[17] P. Peumans, A. Yakimov, and S. R. Forrest, Journal of Applied Physics **93**, 3693 (2003).
[18] P. Y. Bruice, *Organic Chemistry* (Prentice-Hall, Inc., 2003).
[19] S. E. Gledhill, B. Scott, and B. A. Gregg, Journals or Materials Research **20**, 3167 (2005).
[20] I. H. Campbell, T. W. Hagler, and D. L. Smith, Physical Review Letters **76**, 1900 (1996).
[21] T. Aernouts, P. Vanlaeke, W. Geens, et al., Thin Solid Films **451**, 22 (2004).
[22] G. P. Kushto, W. H. Kim, and Z. H. Kafafi, Applied Physics Letters **86**, 093502 (2005).
[23] B. P. Rand, J. Genoe, P. Heremans, et al., Progress in Photovoltaics: Research and Applications **15**, 659 (2007).
[24] D. Mühlbacher, M. Scharber, M. Morana, et al., Advanced Materials **18**, 2884 (2006).
[25] E. Perzon, X. Wang, F. Zhang, et al., Synthetic Metals **154**, 53 (2005).
[26] M. M. Mandoc, W. Veurman, J. Sweelssen, et al., Applied Physics Letters **91**, 073518 (2007).
[27] C. Yin, T. Kietzke, D. Neher, et al., Applied Physics Letters **90**, 092117 (2007).
[28] C. Yin, B. Pieper, B. Stiller, et al., Applied Physics Letters **90**, 1335502 (2007).
[29] R. A. Marsh, C. R. McNeil, A. Abrusci, et al., Nano Letters **8**, 1393 (2008).

[30] R. R. Chance and C. L. Braun, The Journal of Chemical Physics **64**, 3573 (1976).
[31] J. Noolandi and K. M. Hong, The Journal of Chemical Physics **70**, 3230 (1979).
[32] L. Onsager, Physical Review **54**, 554 (1938).
[33] J. Pan, U. Scherf, A. Schreiber, et al., The Journal of Chemical Physics **112**, 4305 (2000).
[34] A. M. Goodman and A. Rose, Journal of Applied Physics **42**, 2823 (1971).
[35] P. J. Melz, The Journal of Chemical Physics **57**, 1694 (1972).
[36] S. Barth and H. Bässler, Physical Review Letters **79**, 4445 (1997).
[37] T. K. Däubler, V. Cimrová, S. Pfeiffer, et al., Advanced Materials **11**, 1274 (1999).
[38] J. Lioyd-Hughes, T. Richards, H. Sirringhaus, et al., Physical Review B **77**, 1253203 (2008).
[39] L. Onsager, The Journal of Chemical Physics **2**, 599 (1934).
[40] C. L. Braun, Journal of Chemistry Physics **80**, 4157 (1984).
[41] A. C. Morteani, P. Sreearunothai, L. M. Herz, et al., Physical Review Letters **92**, 247402 (2004).
[42] T. A. Skotheim and J. Reynolds, in *Conjugated Polymer-Based Photovoltaic Devices*, edited by A. J. Mozer and N. S. Sariciftci (CRC Press, 2006), Vol. 10.
[43] T. Offermans, **PhD Thesis** (2005).
[44] I. Riedel and V. Dyakonov, physica status solidi (a) **201**, 1332 (2004).
[45] A. Pivrikas, G. Juška, R. Österbacka, et al., Physical Review B **71**, 125205 (2005).
[46] D. Gebeyehu, M. Pfeiffer, B. Maennig, et al., Thin Solid Films **451-452**, 29 (2004).
[47] P. Schillinsky, C. Waldauf, and C. J. Brabec, Applied Physics Letters **81**, 3885 (2002).
[48] A. Pivrikas, G. Juska, A. J. Mozer, et al., Physical Review Letters **94**, 176806 (2005).
[49] A. J. Heeger, S. Kievlson, J. R. Schrieffer, et al., Reviews of Modern Physics **60**, 781 (1988).
[50] H. Sirringhaus, P. J. Brown, R. H. Friend, et al., Nature **401**, 685 (1999).
[51] A. Pivrikas, N. S. Sariciftci, G. Juska, et al., Progress in Photovoltaics: Research and Applications **15**, 677 (2007).
[52] C. Vijila, B. Balakrisnan, C. Huang, et al., Chemical Physics Letters **414**, 393 (2005).
[53] W. Geens, T. Martens, J. Poortmans, et al., Thin Solid Films **451-452**, 498 (2004).
[54] R. Österbacka, A. Pivrikas, G. Juska, et al., Current Applied Physics **4**, 534 (2004).
[55] G. Juska, N. Nekrasas, K. Genevicius, et al., Thin Solid Films **451-452**, 290 (2004).
[56] A. J. Mozer, N. S. Sariciftci, L. Lutsen, et al., Applied Physics Letters **86**, 112104 (2005).
[57] G. Juska, K. Arlauskas, M. Viliunas, et al., Physical Review B **62**, R16235 (2000).
[58] G. Juska, K. Arlauskas, M. Viliunas, et al., Physical Review Letters **84**, 4946 (2000).

[59] The equation is derived according to reference 58. Here we corrected the minor error in the corresponding equation given in reference 57).
[60] S. A. Carter, M. Angelopoulos, S. Karg, et al., Applied Physics Letters **70**, 2067 (1997).
[61] T. M. Brown, J. S. Kim, R. H. Friend, et al., Applied Physics Letters **75**, 1679 (1999).
[62] Y. Park, V. Choong, E. Ettedgui, et al., Applied Physics Letters **69**, 1080 (1996).
[63] J. S. Kim, M. Granstrm, R. H. Friend, et al., Journal of applied physics **84**, 6859 (1998).
[64] R. Farchioni and G. Grosso, *Organic Electronic Materials: Conjugated Polymers and Low Molecular Weight Organic Solids* (Springer, 2001).
[65] S. R. Forrest, Chemical Reviews **97**, 1793 (1997).
[66] C. M. Ramsdale, J. A. Barker, A. C. Arias, et al., Journal of Applied Physics **92**, 4266 (2002).
[67] K. Kim, J. Liu, M. A. G. Namboothiry, et al., Applied Physics Letters **90** (2007).
[68] C. R. McNeill, S. Westenhoff, C. Groves, et al., Journal of Physical Chemistry C **111**, 19153 (2007).
[69] H. Hoppe and N. S. Sariciftci, Journal of Materials Research. **19**, 1924 (2004).
[70] C. Giebeler, H. Antoniadis, D. D. C. Bradley, et al., Applied Physics Letters **72**, 2448 (1998).
[71] M. Redecker, D. C. Bradley, M. Inbasekaran, et al., Advanced Materials **11**, 241 (1999).
[72] A. C. Arias, J. D. MacKenzie, R. Stevenson, et al., Macromolecules **34**, 6005 (2001).
[73] M. Granström, K. Petritsch, A. C. Arias, et al., Nature **395**, 257 (1998).
[74] J.-S. Kim and R. H. Friend, Applied Physics Letters **87**, 023506 (2005).
[75] X. H. Yang, F. Jaiser, B. Stiller, et al., Advanced Functional Materials **16**, 2156 (2006).
[76] X. H. Yang, D. C. Müller, D. Neher, et al., Advanced Materials **18**, 948 (2006).
[77] H. Hoppe, T. Glatzel, M. Niggemann, et al., Nano Letters **5**, 269 (2005).
[78] B. Pieper, **Diplom thesis** (2006).
[79] N. Koch, A. Elschner, and R. L. Johnson, Journal of Applied Physics **100**, 024512 (2006).
[80] J. A. Barker, C. M. Ramsdale, and N. C. Greenham, Physical Review B **67**, 075205 (2003).
[81] V. D. Mihailetchi, L. J. A. Koster, J. C. Hummelen, et al., Physical Review Letters **93**, 216601 (2004).
[82] H. J. Snaith, N. C. Greenham, and R. H. Friend, Advanced Materials **16**, 1640 (2004).
[83] R. H. Bube, *Photconductivity of Solids* (John Wiley & Sons, New York, 1960).
[84] T. K. Däubler, D. Neher, H. Rost, et al., Physical Review B **59**, 1964 (1999).
[85] P. Schilinsky, C. Waldauf, J. Huach, et al., Journal of Applied Physics **95**, 2816 (2004).
[86] W. Ma, C. Yang, X. Gong, et al., Advanced Functional Materials **15**, 1617 (2005).

[87] G. Li, V. Shrotriya, J. Huang, et al., Nature Materials **4**, 864 (2005).
[88] M. Reyes-Reyes, K. Kim, and D. L. Carroll, Applied Physics Letters **87**, 083506 (2006).
[89] T. Offermans, P. A. van Hal, S. C. J. Meskers, et al., Physical Review B **72**, 045213 (2005).
[90] H. Tillmann and H.-H. Hörhold, Synthetic Metals **101**, 138 (1999).
[91] A. J. Breeze, Z. Schlesinger, S. A. Carter, et al., Organic Photovoltaics (proceedings of SPIE) **4108**, 57 (2001).
[92] A. J. Breeze, Z. Schlesinger, S. A. Carter, et al., Solar Energy Materials and Solar Cells **83**, 263 (2004).
[93] T. Kietzke, Advances in OptoElectronics **2007**, 40285 (2007).
[94] C. Yin, T. Kietzke, D. Neher, et al., Solar Energy Materials & Solar Cells **91**, 411 (2007).
[95] S. Pfeiffer, H. Rost, and H.-H. Hörhold, Macromolecular Chemstry Physics **200**, 2471 (1999).
[96] T. Kietzke and A. Zen, private communication (2005).
[97] S. V. Chasteen, **Phd Thesis** (2005).
[98] G. H. Gelinck, S. E.G.J., D.-H. Hwang, et al., Synthetic Metals **84**, 1013 (1997).
[99] R. H. Friend, G. J. Denton, J. J. M. Halls, et al., Solid State Communications **102**, 249 (1997).
[100] J. Cornil, A. J. Heeger, and J. L. Bredas, Chemical Physics Letters **272**, 463 (1997).
[101] N. C. Greenham, I. D. W. Samuel, G. R. Hayes, et al., Chemical Physics Letters **241**, 89 (1995).
[102] M. Yan, L. J. Rothberg, F. Papadimitrakopoulos, et al., Physical Review Letters **72**, 1104 (1994).
[103] S. A. Jenekhe, Advanced Materials **7**, 309 (1995).
[104] R. Farchioni and G. Grosso, *Organic Electronic Materials* (Springer, 2001).
[105] J. W. Blatchford, T. L. Gustafson, A. J. Epstein, et al., Physical Review B **54**, 3683 (1996).
[106] J. W. Blatchford, S. W. Jessen, L.-B. Lin, et al., Physical Review B **54**, 9180 (1996).
[107] I. D. W. Samuel, Physical Review B **52**, 573 (1995).
[108] I. D. W. Samuel, G. Rumbles, C. J. Collison, et al., Chemical Physics **227**, 75 (1998).
[109] F. De Lucia, C., T. L. Gustafson, D. Wang, et al., Physical Review B **65** (2002).
[110] C. Yin, **Master Thesis** (2005).
[111] S. V. Chasteen, S. A. Carter, and G. Rumbles, Journal of Chemical Physics **124**, 214704 (2006).
[112] S. V. Chasteen, J. O. Härter, J. C. Scott, et al., Journal of Applied Physics **99**, 033709 (2006).
[113] A. C. Morteani, A. S. Dhoot, J.-S. Kim, et al., Advanced Materials **15**, 1708 (2003).
[114] S. C. Veenstra, W. J. H. Verhees, J. M. Kroon, et al., Chemistry of Materials **16**, 2503 (2004).
[115] M. Yan, L. J. Rothberg, E. W. Kwock, et al., Physical Review Letters **75**, 1992 (1995).

[116] L. Smilowitz, A. Hays, A. J. Heeger, et al., Journal of Chemical Physics **98**, 6504 (1993).
[117] A. C. Morteani, A. S. Dhoot, J.-S. Kim, et al., Advanced Materials **15**, 1708 (2003).
[118] A. C. Morteani, P. Sreearunothai, L. M. Herz, et al., Physical Review Letters **92**, 247402 (2004).
[119] T. Offermans, P. A. van Hal, S. C. J. Meskers, et al., Physical Review B **72**, 045213 (2005).
[120] T. Kietzke, D. A. M. Egbe, H.-H. Hörhold, et al., Macromolecules **39**, 4018 (2006).
[121] S. C. Veenstra, W. J. H. Verhees, J. M. Kroon, et al., Chemistry Material **16**, 2503 (2004).
[122] V. D. Mihailetchi, J. Wildeman, and P. W. M. Blom, Physical Review Letters **94**, 126602 (2005).
[123] J. J. M. Halls, A. C. Arias, J. D. MacKenzie, et al., Advanced Materials **12**, 498 (2000).
[124] S. E. Shaheen, C. J. Brabec, N. S. Sariciftci, et al., Applied Physics Letters **78**, 841 (2001).
[125] J. Peet, J. Y. Kim, N. E. Coates, et al., Nature Materials **6**, 497 (2007).
[126] A. J. Moule and K. Meerholz, Advanced Materials **20**, 240 (2008).
[127] in *U.S. Department of Health and Human Services. Hazardous Substances Data Bank*, 1993).
[128] J.-F. Chang, B. Sun, D. W. Breiby, et al., Chemistry of Materials **16**, 4772 (2004).
[129] H. J. Snaith, A. C. Arias, A. C. Morteani, et al., Nano Letters **2**, 1353 (2002).
[130] C. R. McNeill, H. Frohne, J. L. Holdsworth, et al., Nano Letters **4**, 2503 (2004).
[131] T. Kietzke, D. Neher, M. Kumke, et al., Small **3**, 1041 (2007).
[132] M. M. Mandoc, W. Veurman, L. J. A. Koster, et al., Advanced Functional Materials **17**, 2167 (2007).
[133] M. Castellani and D. Berner, Journal of Applied Physics **102**, 024509 (2007).
[134] V. D. Mihailetchi, W. J, and P. W. M. Blom, Physical Review Letters **94**, 126602 (2005).
[135] T. Offermans, S. C. J. Meskers, and R. A. J. Janssen, Chemical Physics **308**, 125 (2005).
[136] M. M. Mandoc, W. Veurman, L. J. A. Koster, et al., Journal of Applied Physics **101**, 104512 (2007).
[137] T. A. Ford, I. Avilov, D. Beljonne, et al., Physical Review B **71**, 125212 (2005).
[138] D. Veldman, T. Offermans, J. Sweelssen, et al., Thin Solid Films **511-512**, 333 (2006).
[139] R. A. Marsh, C. Groves, and N. C. Greenham, Journal of Applied Physics **101**, 083509 (2007).
[140] G. Juška, K. Arlauskas, J. Stuchlik, et al., Journal of Non-Crystalline Solids **352**, 1167 (2006).
[141] B. P. Rand, J. Li, J. Xue, et al., Advanced Materials **17**, 2714 (2005).
[142] J. Xue, B. P. Rand, S. Uchida, et al., Journal of Applied Physics **98**, 124903 (2005).

[143] A. J. Breeze, Z. Schlesinger, and S. A. Carter, Physical Review B **64**, 12505 (2001).
[144] C. Goh, S. R. Scully, and M. D. McGehee, Journal of Applied Physics **101**, 114503 (2007).
[145] W. U. Huynh, J. J. Dittmer, and A. P. Alivisatos, Science **295**, 2425 (2002).
[146] L. J. A. Koster, V. D. Mihailetchi, and P. W. M. Blom, Applied Physics Letters **88**, 093511 (2006).
[147] M. Svensson, F. Zhang, S. C. Veenstra, et al., Advanced Materials **15**, 988 (2003).
[148] S. Roquet, A. Cravino, P. Leriche, et al., Journal of the American Chemical Society **128**, 3459 (2006).
[149] Z. Ooi, T. L. Tam, A. Sellinger, et al., Energy & Environmental Science **1**, 300 (2008).
[150] R. Y. C. Shin, T. Kietzke, S. Sudhakar, et al., Chemistry of Materials **19**, 1892 (2007).
[151] T. Kietzke, R. Y. C. Shin, D. A. M. Egbe, et al., Macromolecules **40**, 4424 (2007).
[152] Z. E. Ooi, T. L. Tam, R. Y. C. Shin, et al., Journal of Materials Chemistry **18**, 4619 (2008).
[153] C. R. McNeill, B. Watts, L. Thomsen, et al., Nano Letters **6**, 1202 (2006).
[154] C. R. McNeill, J. J. M. Halls, R. Wilson, et al., Advanced Functional Materials **18**, 2309 (2008).
[155] J. S. Kim, R. H. Friend, I. Grizzi, et al., Applied Physics Letters **87** (2005).
[156] C. Yin, B. Pieper, B. Stiller, et al., Applied Physics Letters **90**, 133502 (2007).
[157] C. Yin, M. Schubert, S. Bange, et al., The journal of physical chemistry C **112**, 14607 (2008).
[158] S. R. Forrest, MRS Bull **30**, 28 (2005).
[159] A. J. Lewisa, A. Ruseckasa, O. P. M. Gaudina, et al., Organic Electronics **7**, 452 (2006).
[160] D. E. Markov, E. Amsterdam, P. W. M. Blom, et al., The Journal of Physical Chemistry A **109**, 5266 (2005).
[161] J. K. J. van Duren, X. Yang, J. Loos, et al., Advanced Functional Materials **14**, 425 (2004).
[162] C. Uhrich, R. Schueppel, A. Petrich, et al., Advanced Functional Materials **17**, 2991 (2007).
[163] R. Schueppel, K. Schmidt, C. Uhrich, et al., Physical Review B **77**, 085311 (2008).
[164] L. Kelvin, Philosophical Magazine and Journal of Science **46**, 82 (1898).
[165] K. L. Sorokina and A. L. Tolstikhina, Crystallography Reports **49**, 476 (2004).
[166] V. Palermo, M. Palma, and P. Samori, Advanced Materials **18**, 145 (2006).
[167] G. Droval, **Project report** (2001).

# Acknowledgements

I would like to thank Prof. Dr. Dieter Neher for continuous guiding, supporting and great patience and for providing the opportunities to attend conferences.

I am particularly thanking Dr. Thomas Kietzke. As my supervisor for my master thesis, he offered continuous helping and supporting even after he left university. His useful and quantitive suggestions greatly inspired me during my PhD time.

Prof. Dr. Hans-Heinrich Hörhold and Dr. Allan Sellinger are greatly thanked for generously supplying a large amount of semiconducting materials. Particully thank Allan's fruitful discussions.

Many thanks to Dr. Michael Kumke and Prof. Dr. Hans-Gerd Löhmannsröben for the access to the time-resolved measurements.

I would like to thank Professor Dr. Reimund Gerhard and his group for the access to the thickness measurement.

I am very grateful of Dr. Denis Mc Carthy for his generous help of correcting the English of this thesis.

Special thank Sebastian Bange and Dr. Frank Jaiser for the very important suggestions for all my presentations and for their great generous help in the lab and on computer work. Many thanks to Burkhard Stiller for the help with AFM measurements. Particularly I need to thank Marcel Schubert. This work will not be beautiful without his assistance. I am grateful to my lovely colleagues: Sylvia Paul and Beate Reinhold. Without them, I would not have so much fun during my PhD time. And thanks to all of my colleagues in the PWM group. The nice coffee breaks I had with them are the best refreshment for the work. I appreciate so many wonderful evenings I spent with them by the cooking evening (Koch Abend) or by drinking. The nice atmosphere in the group is the greatest wealth I had.

There are too much words I would like to say to my friends: Lekha Kietzke, Meena Ganesan, Rosaura Flores Suárez, Pantea Nazaran and Qiong Tong. There are so many unforgettable days I spent with them and so much help and encouragement I got from them. Their generous friendship is worth for me to enjoy with my whole life.

Finally, I would like to thank my husband Daniel Petri, my parents and my lovely sister for their understanding, support and great love.